Aerodynamic analysis of the closure flap mechanism inside the NACA ram-air intake

K.C. Leung

Technische Universiteit Delft

TU Delft Delft University of Technology

Challenge the future

AERODYNAMIC ANALYSIS OF THE CLOSURE FLAP MECHANISM INSIDE THE NACA RAM-AIR INTAKE

by

K.C. Leung

in partial fulfillment of the requirements for the degree of

Master of Science
in Aerospace Engineering

at the Delft University of Technology,
to be defended publicly on Monday August 24, 2020 at 09:00 AM.

Supervisor:	Dr. ir. R. Vos	TU Delft
Thesis committee:	Prof. dr. ir. L. L. M. Veldhuis	TU Delft
	Dr. ir. A. H. van Zuijlen	TU Delft

An electronic version of this thesis is available at http://repository.tudelft.nl/.

TU Delft Delft University of Technology

PREFACE

This document marks the end of my thesis project and my academic career at the faculty of Aerospace Engineering at TU Delft. I would like to thank my supervisor dr.ir. Roelof Vos for this effort and time in supervising and tutoring me throughout the thesis project. Roelof's feedback has enabled me to achieve a desirable outcome of this thesis project.

I would also like to thank the people I met and the friends that I have made during my study period at Aerospace Engineering. My study period would not have been the same without them. The people from the FPP room have made the period of my thesis project really enjoyable with countless jokes, lots of coffee breaks, deep discussions, and the word that should not be said out loud here. Special thanks to Antonio who helped me a lot during my biggest battle with Ansys. That was a bloody fight.

Also, I would like to thank my family and friends, in particular my sisters, Tatsen and LR boys for the fun times, and their inspirational words and motivational speeches when I was lost. Especially, Pravin has encouraged me to get through the hard times.

Last but not least, actually the most important person, I would like to thank my *mama* for her unconditional and endless support, and her sometimes special style of encouragement.

K.C. Leung
Delft, August 2020

SUMMARY

In recent years, the environmental impact of transportation, especially from the growing aviation industry has raised concerns by the public. Environmental experts predicted that air transportation is growing for the coming two decades [1]. In order to maintain a sustained global economy, the aviation industry has been triggered to find more innovative solutions to become more environmentally friendly in this industry. The faculty of Aerospace Engineering of Delft University of Technology (TU Delft) collaborates with Airbus in the Movables for Next Generation Aircraft (MANTA) project to find new innovative solutions with the goal to improve the conventional NACA ram-air inlet [2]. The closure flap inside the NACA ram-air inlet regulates the amount of ram-air that is ingested by the NACA ram-air inlet. This flap consists of two rigid plates. It was demonstrated that a very pronounced kink is present for a certain configuration. This pronounced kink causes undesirable aerodynamic effects [3]. Due to the presence of this kink, the freestream airflow is subjected to a sharp deflection, which triggers flow separation and hence results in pressure losses in the diffused part inside the NACA ram-air inlet and vibrations at the inlet [3]. During the flight, this can also cause noise. A single morphing flap has been proposed as the replacement design of the closure flap mechanism inside the inlet of the Airbus A320. Since this is a new development in the design of the NACA ram-air inlet, no similar research on this particular design has been conducted yet.

Steady-state Reynolds-Averaged Navier-Stokes (RANS) based Computational Fluid Dynamics (CFD) simulations were conducted in order to analyse the aerodynamic performance of the conventional hinged flap and the new design with morphing flap for a range of operating settings. Each set of flap design has three different configurations, from which the minimal distance inside in the inlet was varied. A range of mass flow rates was varied in the CFD simulations. The geometry was based on the dimensions of the real NACA ram-air inlet of the Airbus A320. Since three different configurations were used for the CFD simulations, the grid had to be assessed on the discretisation error of the CFD simulations. The Least Squares version of the Grid Convergence Index (GCI) was used [4]. A trade-off between the required run time of the CFD simulation and the level of accuracy was made.

From the CFD results, it was observed that the largest differences in pressure recovery improvement and drag reduction are found for Configuration 1 with an opening of 15 $[mm]$. Configuration 1 with an opening of 15 $[mm]$ inside the NACA ram-air inlet showed a significant improvement in pressure recovery. The largest improvement in terms of pressure recovery between the Configuration with morphing flap and with hinged flap, which was found to be 13.5% at a low mass flow rate of 0.100 $[kg/s]$. By investigating the drag envelope, the maximum improvement of the drag of the morphing flap with respect to the hinged flap is 33.8%. By assessing the Cp-plots of the ramp and the closure flap between Configuration 1 with a hinged flap and a morphing flap, it was shown that a strong suction peak was present at the location of the sharp kink in the hinged flap. This kink has been eliminated by the smooth characteristics of the morphing flap, minimising the local supervelocity. This means that the strong adverse gradient is reduced, such that the boundary layer is less prone to flow separation, minimising pressure losses. Configuration 3 with a morphing flap has a lower pressure recovery than Configuration 3 with a hinged flap for most mass flow rates. High obliquity and high flow spillage cause large pressure losses [5]. It was shown that vortex ingestion is high at high mass flow rates. This results in higher pressure losses due to vortex cores.

CONTENTS

List of Symbols

Greek Symbols	Description	Unit
α	Angle of attack	$[deg]$
γ	Ratio of specific heats	$[-]$
Δ	Maximum absolute difference between all solutions	$[-]$
δ_{RE}	Error estimation by Richardson's extrapolation	$[-]$
ϵ	Dissipation rate of turbulent kinetic energy	$[m^2/s^2]$
η	Pressure recovery	$[-]$
μ	Dynamic viscosity	$[kg/(ms)]$
ν	Kinematic viscosity	$[m^2/s]$
ν_T	Eddy viscosity	$[Pa \cdot s]$
ρ	Air density	$[kg/m^3]$
τ	Shear stress	$[Pa]$
ϕ	Flow variable	$[-]$
ω	Specific turbulence dissipation rate	$[1/s]$

Latin Symbols	Description	Unit
A	Area	$[m^2]$
C_f	Skin friction coefficient	$[-]$
C_D	Drag coefficient	$[-]$
C_p	Pressure coefficient	$[-]$
D	Drag	$[N]$
e	Specific energy	$[J/kg]$
E	Energy	$[J]$
F_s	Safety factor	$[-]$
h	Representative grid cell size	$[-]$
h	Heat transfer coefficient	$[W/(m^2 \cdot K)]$
k	Turbulence kinetic energy	$[J/kg]$
k	Thermal conductivity of the fluid	$[W/(m \cdot K)]$
l	Characteristic length	$[m]$
$\dot{m}$	Mass flow rate	$[kg/s]$
M	Mach number	$[-]$
Nu	Nusselt number	$[-]$
p^*	Observed order of convergence	$[-]$
P	Pressure	$[Pa]$
Pr	Prandtl number	$[-]$
R	Gas constant	$[J/(kg \cdot K)]$
q	Dynamic pressure	$[Pa]$
Re	Reynolds number	$[-]$
S_{ref}	Reference area	$[m^2]$
T	Temperature	$[K]$
U_s	Standard deviation	$[-]$
U_ϕ	Overall uncertainty	[%]
y^+	Dimensionless wall distance	$[-]$
Q	Heat transfer	$[W]$

Subscripts	Description
∞	freestream
t	total
s	static
0	ambient
1	throat

List of Abbreviations

CAD	Computer-Aided Design
CFD	Computational Fluid Dynamics
DNS	Direct Numerical Simulation
ECS	Environmental Control System
LES	Large Eddy Simulation
MANTA	Project Movables for Next Generation Aircraft
NACA	National Advisory Committee for Aeronautics
PACK	Pressurisation and Air Conditioning Kit
RANS	Reynolds-Averaged Navier-Stokes
RPR	Ram Pressure Ratio
SST	Shear Stress Transport
TU Delft	Delft University of Technology
URANS	Unsteady Reynolds-Averaged Navier-Stokes

List of Figures

List of Tables

1

INTRODUCTION

The design of an inlet is one of the most challenging tasks of the development of aircraft with air-breathing systems. The NACA ram-air inlet was developed in the 1950s by a research group at the National Advisory Committee for Aeronautics (NACA) and no radical changes in its design have been done. In recent years, the environmental impact of transportation, especially from the growing aviation industry has raised concerns by the public. Environmental experts predicted that air transportation is growing for the coming two decades [1]. In order to maintain a sustained global economy, more innovative solutions in the aviation industry are needed to strive to become more environmentally friendly.

For this reason, the faculty of Aerospace Engineering of Delft University of Technology (TU Delft) collaborates with Airbus in the Project Movables for Next-Generation Aircraft (MANTA) upon finding a new innovative solution with the goal to improve the NACA ram-air inlet [6]. A single morphing flap has been proposed as replacement design of the closure flap mechanism inside the NACA ram-air inlet of the Airbus A320. Since this is a new development in the design of the NACA ram-air inlet, no similar research on this particular design has been conducted yet.

The scope of the thesis project is bounded to the forward part of the air-conditioning system of the Airbus A320, which encompasses the NACA ram-air inlet that is submerged on the surface of the fuselage. The influence on proceeding parts of the air-conditioning system such as the precoolers, heat exchangers and the outlet upon the inlet performance will not be treated in the thesis project.

1.1. HISTORY OF AIR-BREATHING INLETS

The inlet needs to deal with the mismatch between the airflow condition in the freestream and the required inflow conditions for the engine at the inlet entrance. The inlets have to able to ingest the required amount of air for various flight conditions. The role of the inlet is to achieve the required transformation at high efficiency. A high efficiency equals to the maximisation of the pressure recovery, while simultaneously the drag, complexity of the design, weight and cost are minimised. A significant source of energy loss is friction on the external surface, which is caused by wetting the surface with airflow. The low-energetic airflow will then be ingested by the air inlet resulting in high pressure losses.

In the early years of jet aircraft development, many aircraft manufacturers opted for minimising pressure losses by placing the inlets far off the fuselage or integrating with the nose of the aircraft. The engine inlet of the North American F-86F aircraft, shown in Figure 1.1, was integrated with the nose of the aircraft, such that the ingested incoming airflow is undisturbed and clean.

Figure 1.1: North American F-86F aircraft [1]

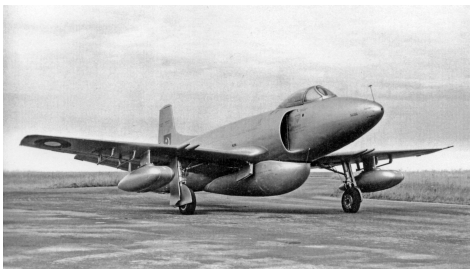

Figure 1.2: Supermarine Attacker aircraft [2]

Another philosophy is to integrate a Y-shaped duct on the sides of the fuselage, as shown by the Supermarine Attacker aircraft in Figure 1.2. One drawback of such design is that the long bifurcated duct requires sharp bends around the cockpit, which causes significant losses due to wall friction. Another disadvantage is that it can cause high flow distortion through mixing for asymmetric operation in which mass flow is ingested unequally. On the other hand, this specific type of submerged inlet has the advantage that little drag is added, whilst providing a good pressure recovery and its low weight characteristics. The submerged inlet lies below the outer skin of the aircraft fuselage, such that it does not add to the radar cross-sectional area of the aircraft, making the submerged inlet suitable for stealth technology [7]. This particular type of air inlet is named as the submerged inlet or known as the flush (mounted) inlet [8].

The same findings have been noticed earlier by a researcher at the National Advisory Committee, F.M.Rogallo conducted intensive experimental research to determine efficient arrangements of different inlet shapes, from extruding inlets to parallel-walled inlets, for internal-flow systems in the year 1941 [9]. He had concluded that the inlet opening of an internal-duct system should be located at the forward stagnation points of the part of the aircraft to be most efficient. The tests also indicated that small openings for airflow resulted in relatively high losses [9]. He concluded that the submerged inlet has difficulties in achieving low internal-flow losses, mainly because the airflow is diverted from its flow path along the aircraft fuselage into the duct entrance [9]. Therefore, the submerged inlets should not be used for internal-flow systems because of its poor drag characteristics which lead to high losses [9].

The Ames Aeronautical Laboratory, a facility of NACA, conducted further research on submerged inlets. The parallel-walled inlet has shown to diverge the streamlines of the flow as the duct entrance was approached. The research group suggested to modify and diverge the ramp walls to match the walls with the streamlines of the flow in order to achieve an increased inlet performance [10]. This modification allowed the pressure recovery to increase up to 10% [10]. Matching the ramp walls with the local streamlines resulted in good pressure recovery and drag characteristics [10] [11]. The divergent ramp walls should have sharp (lateral) edges to allow improved inlet performance. The submerged-type inlet called NACA ram-air inlet was then invented, knowing for its S-shaped divergent ramp walls [10].

1.2. NACA RAM-AIR INLET MECHANISM

The inlet flap of the NACA inlet mechanism modulates the amount of ambient airflow, which is ingested into the duct tunnel in which the heat exchangers of the Environmental Control System (ECS) use the air to cool down the bleed-air from the engines [12]. The amount of air is controlled and monitored by the temperature unit of the Pressurisation and Air Conditioning Kit (PACK). The ram-air inlet flap is located inside the NACA ram-air inlet and NACA ram-air inlet is located in the belly fairing of the Airbus A320 aircraft, shown in Figure 1.3.

[1] Source:https://classicfighters.org/north-american-f-86-sabre/
[2] Source:https://www.baesystems.com/en/heritage/vickers-supermarine-type-371-spiteful

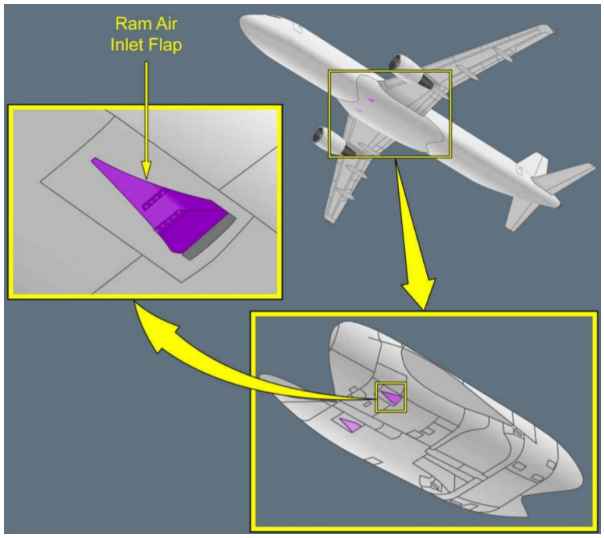

Figure 1.3: The location of the ram-air inlet flap on the belly component of the Airbus A320 [13]

From the observation of Figure 1.4, it can be seen that the ram-air inlet flap consists of two rigid plates connected by a hinge and an actuator attached to the flap mechanism to push in the vertical direction up and downwards. The actuator is responsible for the opening and closing of the NACA ram-air inlet. The entire flap itself is attached to the NACA ram-air inlet by five bolts at the hinge line. The bottom of the downstream rigid plate is connected to an actuator for the deflection. Furthermore, the downstream rigid plate also has two aft-hinges that allow the aft-hinge location to slide a bit back and forth. Opening and closing the ram-air inlet is controlled by the actuator. The flap of the ram-air inlet acts like a door which is nearly closed during take-off and landing to prevent debris from being ingested into the ram-air inlet [14]. The ram-air inlet door is 25% open when the aircraft is on the ground, and it is fully closed in flight [14].

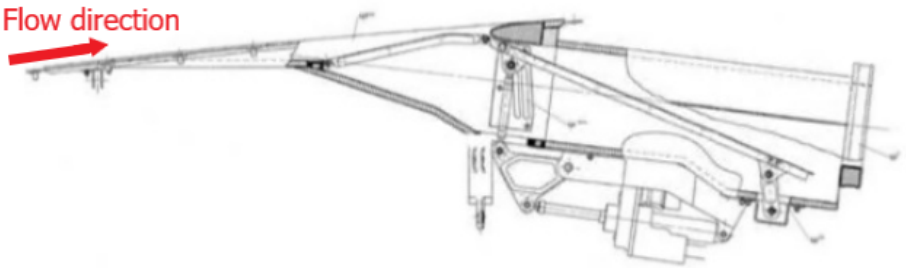

Figure 1.4: Cross-sectional side view of the ram-air inlet of the Airbus A320 aircraft - Courtesy of Airbus

1.3. PROBLEM STATEMENT

The design of the NACA ram-air inlet has attracted interest from researchers. There is a problem with the NACA ram-air inlet in existing aircraft. The source of the problem originates in the design of the ram-air inlet flap, which consists of two rigid plates, as shown in Figure 1.4. The first rigid plate is curved, while the second rigid plate is flat.

Two kinks are present in this conventional closure flap design. The first kink is located in the middle of the rigid plate due to the permanent curvature of the plate. The second kink is located at

the hinge between the two individual rigid plates. For the configuration in which the ram-air inlet flaps are (nearly) closed, as shown in Figure 1.5, the kink that is located between the two individual rigid plates is very pronounced. Computational Fluid Dynamics (CFD) simulations have shown that this pronounced kink causes undesirable aerodynamic effects, shown in Figure 1.5 [3]. Due to the presence of this kink, the freestream airflow is subjected to a sharp deflection, which triggers flow separation and hence results in pressure losses in the diffused part inside the NACA ram-air inlet and vibrations at the inlet [3]. During the flight, this can also cause the development of noise.

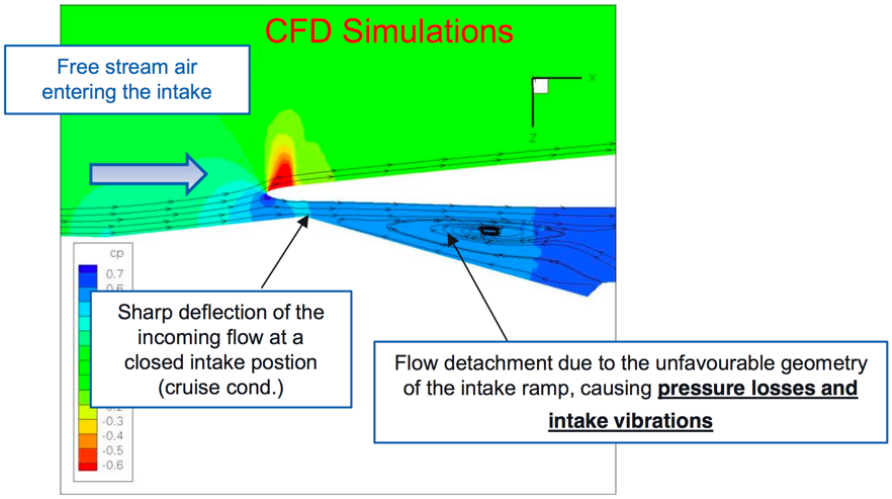

Figure 1.5: CFD results of a configuration with the deflected closure flap [Courtesy of Airbus]

It is expected that smoother geometry without sharp kinks leads to improvement in aerodynamic performance. The simplest solution to this problem is to remove the sharp kink by designing a smoother hinge between the two rigid individual flaps or using flexible geometry, which inherently eliminates the kink in the closure flap and thus unfavourable geometry is avoided. The closure flap is required to deflect up and down to modulate the amount of airflow that is being ingested into the duct. A method to tackle the problem with the ram-air flap is to design aircraft structures with the properties that possess smoother geometry and are able to change its shape without introducing sharp kinks. Smart materials and adaptive structures have made new novel designs possible and overcome its limitations. For this reason, a single morphing flap made of laminate is proposed as an innovative solution to the old design with rigid hinged plates. The aerodynamic analysis shall show the changes in aerodynamic effects by replacing the closure flap with rigid plates with a morphing flap.

1.4. RESEARCH OBJECTIVE

A literature review on the traditional NACA ram-air inlets have been conducted. However, it lacks aerodynamic analysis on the NACA ram-air inlet with its new proposed design. This causes a gap in the implementation of new projects.

The primary goal of this thesis project is to analyse the aerodynamic effects of the NACA ram-air inlet when the hinged flap is replaced by a single morphing flap. The new design with the single morphing flap as the new closure flap mechanism will be compared with the old design with the hinged flap. A secondary goal of this thesis is to understand the inlet performance of the NACA ram-air inlet with a morphing flap in comparison with a hinged flap. To analyse the aerodynamic effects of the NACA ram-air inlet, CFD simulations will be performed for multiple cases.

Based on the motivation, the research objective can be summarised and is stated as follows:

- *Investigate the aerodynamic effects of the closure flap mechanism inside the NACA ram-air inlet of the Airbus A320 with a single morphing flap through Computational Fluid Dynamics simulations*

1.5. THESIS OUTLINE

The thesis is outlined as follows. Chapter 2 deals with the literature review in which past research on the ram-air inlet were compared. The aerodynamic background behind the ram-air inlet will also be presented. This is followed by Chapter 3 in which the methodology in CFD is presented and discussed, including the geometry of the real NACA ram-air inlet, the approach to the different test cases and the mesh generation are presented. In Chapter 4, the grid convergence study of a set of grids is conducted. The results from the CFD simulations are presented and discussed in Chapter 5. Finally, the conclusions of this thesis project on the design of the closure flap mechanism inside the NACA ram-air inlets and recommendations for future work are presented in Chapter 6.

2

THEORETICAL BACKGROUND

This chapter deals with the experimental and numerical studies that have been done in the past. The experimental studies are needed to show the important aerodynamic phenomenons of the inlets. The numerical studies show how researchers have tried to improve the performance of the inlets, especially by using vortex generators. The experimental investigation on inlets will be discussed in Section 2.1, while the numerical investigation on inlets will be reviewed in Section 2.2. A brief comparison between the inlets that are mostly used for the ECS, the parallel-walled inlet and the NACA ram-air inlet, is made in Section 2.3. The aerodynamic theory on inlets and the parameters to express the inlet performance are discussed in Section 2.4.

2.1. EXPERIMENTAL INVESTIGATIONS

Ram-air inlets have been used in aircraft for auxiliary systems. A great number of research on ram-air inlets have been conducted between 1940 and 1960 by NACA [15]. The ram-air inlets can be divided into two groups: scoop inlets that are protruding the surface, submerged inlets that are located slightly below the surface. Usually, the submerged-type inlets are used on aircraft for auxiliary systems. First, the most basic configurations of the submerged-type inlet and their characteristics are presented in Subsection 2.1.1. Then the experimental work on the submerged-type inlets, NACA ram-air and parallel-walled inlets, will be discussed in Subsections 2.1.2 and 2.1.3, respectively.

2.1.1. SUBMERGED INLETS

The design of the planform, which includes the profile and planform, affects the magnitude and distribution of air that flows into the inlet. These factors have an influence on the overall inlet performance. According to research conducted by Sachs and Spreiter (1951), three types of planforms are presented as the approach ramps of a submerged inlet [16]. The three different planforms are illustrated in Figures 2.1a, 2.1b, and 2.1c.

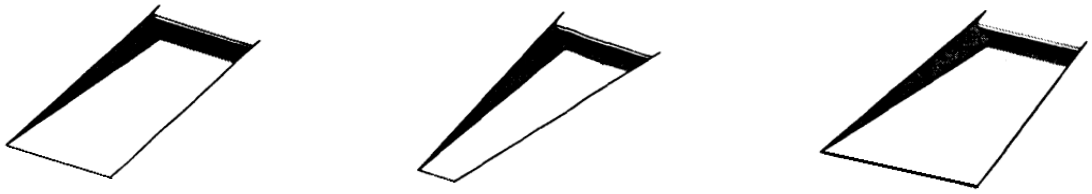

(a) Parallel walls (b) Divergent walls (c) Convergent walls

Figure 2.1: Three different classes of planform for the approach ramp of a submerged inlet [16]

For the parallel-walled inlet shown in Figure 2.1a, the author concluded that flow around the parallel-walled inlet can be modelled as a two-dimensional flow for average mass flow ratios [16].

The second class of planform, the divergent-walled inlet, is shown in Figure 2.1b. According to the authors, this planform has two main differences with respect to the parallel-walled inlet. Firstly, since the flow near the ramp floor is not aligned with the flow direction, the flow around the inlet with divergent walls cannot be approximated as a two-dimensional flow [16]. Secondly, the external flow is not aligned with the edge of the divergent walls and is forced to flow over the edges into the inlet cavity [16]. The described phenomenon is illustrated in Figure 2.2.

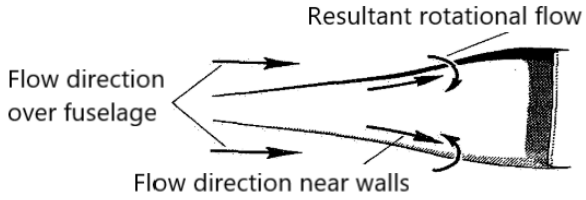

Figure 2.2: Vortex around the edge of the ramp of a divergent walled inlet [17]

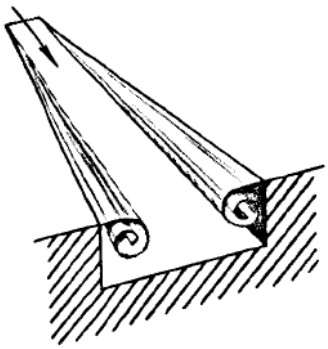

Figure 2.3: Vortex sheet in a divergent inlet [16]

The authors believed that these two reasons cause a vortex sheet to be generated along the ramp walls of the divergent-walled inlet. The design of an inlet affects both the boundary layer and the generation of vortex sheets [16]. Figure 2.3 illustrates the described phenomenon.

The third type is the convergent-walled inlet that behaves similar to the divergent-walled inlet with generating a pair of vortices. The main difference of the convergent-walled inlet is that the vortices roll outwards over the wall edges, such that the effect of the vortices on the pressure recovery is small [16].

The divergent-walled and parallel-walled inlets are mostly used for the auxiliary systems on the aircraft. The experimental work on a special type of the divergent-walled inlet, the NACA ram-air inlet, will be discussed in Subsection 2.1.2. The parallel-walled inlet will be discussed in Subsection 2.1.3.

2.1.2. NACA RAM-AIR INLET

Rogallo presented in 1941 the results of the experimental research on different inlet shapes for an internal-flow system, which has been tested in a 5-foot (1.52[m]) vertical wind tunnel (1941) [9]. Rogallo tested a wide variation of opening shapes during the experiments from flush openings with circular ducts, adjustable-flap openings, parallel-walled openings, scoops and circular pipes protruding the surface plate. The researcher concluded that the submerged inlets should not be used because of its poor pressure characteristics [9]. Researchers of Ames Aeronautical Laboratory, a facility of NACA, however, found interesting results about the parallel-walled inlet. The results showed that the streamlines of the flow diverge as the duct entrance is approached. The researchers tried to match the divergent ramp walls with the local streamlines, the divergent-walled inlet with S-shaped ramp edges was invented [10]. This type of inlet is known as the NACA ram-air inlet. A large number of research on NACA ram-air inlets have been conducted.

Gault (1947)

Gault investigated NACA ram-air inlets on a 1/5-scale model of the fighter aircraft (1947) [18]. The twin NACA ram-air inlets were positioned on the side of the fuselage, above the leading edge of the wing. Figure 2.4 shows the wind tunnel test setup of the research conducted by Gault.

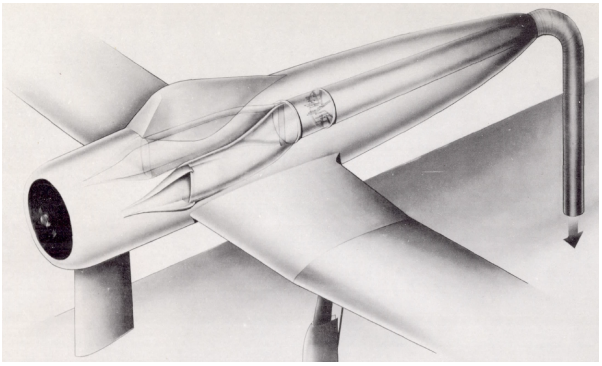

Figure 2.4: Schematic overview of the experimental test setup of the 1/5-scale model of the fighter aircraft [18]

The results of the pressure losses and the pressure distribution of the lip and ramp as a function of angle of attack and velocity ratio were acquired by the experiments [18]. The flaps were deflected at 55° while the velocity ratio and angle of attack were kept constant. The investigation aimed to investigate the variations of pressure distributions. This wind tunnel experiment revealed that there was a region of low energy flow along the edge of the inlet, in the vicinity of the wing [18]. It was determined that low energy regions that occurred near the side of the inlet, adjacent to the wing, caused significant pressure losses [18]. Moreover, the streamline pattern of the flow was disturbed by the upwash of the wing, causing the separation of the flow, which resulted in pressure losses in the inlet [18]. Gault concluded that the NACA ram-air inlets should not be placed on the fuselage in the vicinity of the leading edge of the wing.

Mossman and Randall (1948)

Mossman and Randall conducted research on the following submerged inlets: parallel-walled inlets, divergent-walled inlets, and the NACA ram-air inlets with curved-divergent-walls in a 7[ft]-10[ft] (2.13-[m]-3.05-[m]) wind tunnel (1948) [5]. Many design variables have been investigated, such as the effect of the shape of the ramp planform, the ramp angle, the width-to-depth ratio, the small ridges at the edges of the ramp wall, and lip shapes were investigated. The ramp angle is the angle inlet ramp relative to the external surface. The test model of the NACA ram-air inlet is shown in Figure 2.5.

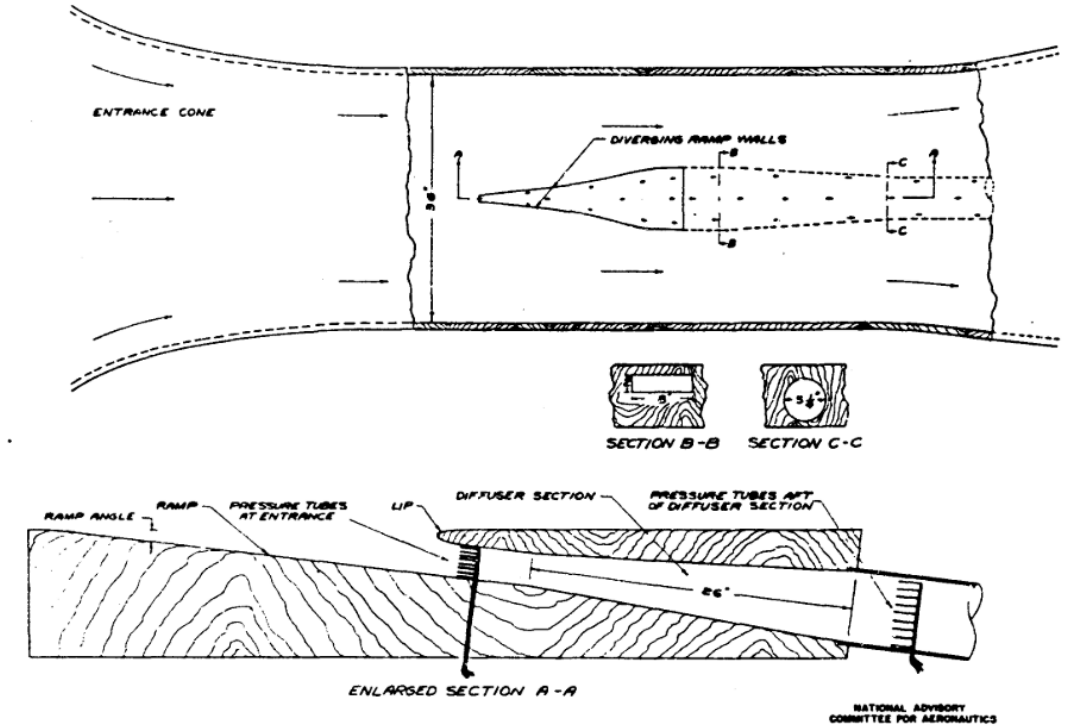

Figure 2.5: The NACA ram-air inlet model that is being tested by Mossman and Randall [5]

The experiments showed that the boundary layer near the duct entrance influences the pressure recovery. It was found that the pressure recovery of a submerged-type inlet can be increased by using divergent ramp planform that thins out the boundary layer [5]. Furthermore, increasing the ramp angle decreases the pressure recovery.

For a given divergent ramp, the angle between diverging ramp walls and the ramp planform increases when the ramp angle increases. According to Mossman and Randall, it generates two adverse effects. First, a large ramp angle provokes flow separation [5]. Second, increasing the ramp angle (shown in Figure 2.5) increases the obliquity between the freestream flow and the ramp walls, making it more difficult for the air to follow the contour of the ramp walls [5] [9].

As a result, there is air spillage at the edge of the ramp walls, causing a crossflow to occur between the freestream flow and the airflow flowing downstream the ramp. This was shown previously in Figure 2.2. These two adverse conditions, high obliquity and high spillage, cause large pressure losses.

The parallel-walled inlet has the lowest pressure recovery with a value of 0.80, whereas the configuration with NACA ram-air inlet has the highest value of the pressure recovery of 0.87. From this result, it was concluded that the walls of the inlet should be curved and divergent (similar to the typical NACA ram-air inlet, which has curved-divergent ramp walls) [5].

Frank and Taylor (1951)

The effects of the angle of attack and Mach number on the pressure recovery and mass flow ratio have been investigated by Frank and Taylor (1951) [19]. Experimental research has been conducted on two different types of ram-air inlets: scoop inlets, and NACA ram-air inlets. The scoop inlet is a protruding inlet that sticks out of the surface, whereas a NACA ram-air inlet is submerged into the surface.

At low mass flow ratios between 0 and 0.5, the pressure recovery measured at the entrance of the NACA ram-air inlet was always higher than the scoop inlet for any Mach number and angle of attack tested in this experiment [19]. The authors found that the boundary layer thickness growth upstream of the scoop inlet was stronger, resulting in a lower pressure recovery [19]. Furthermore, the authors found that the performance of the NACA ram-air inlet is more sensitive than the scoop inlet to the variation of the angle of attack. This adverse effect on the pressure recovery was present especially at low angles of attack for increasing Mach number [19].

2.1.3. PARALLEL-WALLED INLET

The parallel-walled inlet is one of the two commonly used submerged inlets. It has the simplest shape amongst the three basic configurations of submerged inlets, explained in Subsection 2.1.1. It consists of a ramp with two straight inlet walls on the sides, as shown in Figure 2.1a.

Delany (1948)

Delany presented the results of the inlet performance due to the location of the inlet along the fuselage, which has been tested on a 1/4-scale model of a fighter aircraft (1948) [17]. Two different types of ram-air inlets have been investigated, inlet PW: the parallel-walled inlet, and inlet DW: a divergent-walled inlet as found on a NACA ram-air inlet.

Table 2.1: Pressure recovery for forward and aft location of the parallel-walled inlet PW and a divergent-walled inlet DW, respectively [17]

	Forward location	Aft location
Inlet PW	0.890	0.820
Inlet DW	0.970	0.935

The pressure recoveries of the forward and aft location for the two types of the inlet for an inlet velocity ratio of 0.7 are summarised in Table 2.1. Inlets PW and DW were tested on their performance based on the difference of the walls. The pressure recovery for inlet DW is superior to the pressure recovery for inlet PW: the inlet PW provided lower values of pressure recovery than for inlet DW.

The researchers believed that the difference in pressure recovery is due to the difference in the boundary layer thickness of the fuselage. The reason for the lower value of pressure recovery for inlet PW compared to inlet DW was explained by the rotational flow. Due to the shape of the divergent wall, a pair of rotational flow, vortices, is formed. The vortices push the low-energetic flow of the boundary away from the duct entrance. Thinning the boundary layer makes it less prone to flow separation [20]. A thick boundary layer on the fuselage is detrimental to the pressure recovery. The boundary layer thickness of the aft location of the inlet was 33% thicker than for the forward location of the inlet [17]. The interference of the pressure field of the wing might also be adverse. For higher inlet velocity ratios, the strength of the vortices and the proportion of the vortices that was ingested into the duct entrance were increased [17].

Martin and Holzhauer (1948)

This experiment was conducted to investigate the NACA ram-air and the parallel-walled inlets on a full-scale model of a fighter jet (1948) [21]. The effect of the ramp divergence and the use of deflectors were investigated. The ramp divergence is defined as the angle of the ramp with respect to the axial direction of the inlet. The researchers found that the pressure recovery is little affected by the ramp divergence [21]. However, the velocity ratio at which the maximum pressure recovery was achieved, was decreased [21]. The pressure losses of the parallel-walled inlet were higher than the

NACA ram-air inlet, leading to lower pressure recovery. The authors concluded that the application of deflectors improved the pressure recovery of the inlets, but this advantage was cancelled out by the significant drag penalty caused by the deflectors [21].

Dennard (1959)
Dennard has conducted research on the total-pressure recovery and the drag characteristics of several ram-air inlets at transonic speed (1959) [22]. This includes parallel-walled inlets, scoop inlets and NACA ram-air inlets. The scoop inlet is a protruding inlet that sticks out of the surface, whereas the parallel-walled and NACA ram-air inlets are submerged into the surface. The range of Mach number that has been tested lies between 0.55 and 1.3. The ramp angles between with 15° and 90° with increments of 15 degrees were investigated.

Dennard found the following conclusions. For parallel-walled inlets, the lowest drag and the highest value of the pressure recovery were found for the inlet with the smallest inlet ramp angle [22]. Low drag generally occurs at high mass flow ratios. For the scoop inlet, it was found that both the pressure recovery and the drag were high; the drag was even the highest amongst the three inlets tested [22]. The NACA ram-air inlet has the highest pressure recovery and the lowest drag of the three tested inlets [22].

2.2. NUMERICAL INVESTIGATIONS

By the 1990s, technology and computational power became advanced enough to conduct experiments and industrial applications through Computational Fluid Dynamics (CFD). CFD has since become a common tool to analyse aerodynamic flow around an object. This section presents the numerical investigations on the submerged inlets through CFD simulations, with the focus on the improvement of inlet performance by application of the vortices.

Da Silveira et al. (2017)
Da Silveira et al. investigated the effect of the angle of attack on the pressure recovery of the NACA ram-air inlet (2017) [7]. The inlet efficiency was analysed on a canard-type aircraft using CFD simulations. The $SST\ k-\omega$ turbulence model has been applied.

Table 2.2 shows the test cases with their corresponding overall inlet efficiencies.

Table 2.2: Pressure recovery η for different cases [7]

Case	Pressure recovery η
(a) NACA inlet mounted on a flat plate (uniform)	0.520
(b) NACA inlet mounted on a flat plate (flow profile)	0.827
(c) NACA inlet mounted on the fuselage at an angle of attack of 2°	0.930
(d) NACA inlet mounted on the fuselage at an angle of attack of 15°	0.633

In the first case (a) without the real flight conditions, the inlet efficiency is 52%. It showed that a pair of vortices is sucked into the inlet, reducing the inlet efficiency [7]. In the second case (b), in which flight conditions were imposed upon, the efficiency increased to 83%. This showed the impact of the inlet conditions on the pressure recovery. The third (c) and fourth (d) case showed the effect of the angle of attack on the inlet efficiency.

It can be noticed that at an angle of attack of 0° (cruise condition) the pressure recovery is highest at 93%. The efficiency decreases significantly to 63% when the angle of attack in case (c) has been changed from 2° to 15°. Case (d) showed that a vortex is formed and then sucked into the inlet causing the pressure recovery to drop [7]. Furthermore, a high angle of attack caused the NACA ram-air inlet to experience high flow disturbance which resulted in a decrease of pressure recovery. [7].

Devine et al. (2004)

Devine et al. tried to combine both advantages in a novel design; the insensitivity of the velocity ratio to the pressure recovery of parallel-walled inlets and the high peak performance of the NACA ram-air inlet (2004) [23]. It means that the research goal was to improve the simple, easy to manufacture parallel-walled inlet, such that the same low-drag characteristic of NACA ram-air inlet is being met [23].

In this experiment, the use of vortex generators was applied in order to improve inlet performance. This study was done through CFD simulations. The $k-\omega$ turbulence model was used in which two transport equations represents the turbulence quantities of the flow.

Figures 2.6a and 2.6b show the influence of the height and spacing of the vortex generators, respectively. In this paper, the pressure recovery was defined as the ram pressure ratio (RPR). Velocity ratio (VR) was defined as the ratio of the velocity at the inlet to the freestream velocity. The results showed that the total pressure of each combination with a vortex generator was significantly higher compared to the inlet configuration without a vortex generator. The authors believed that the vortices that were generated by the vortex generators located in front of the NACA ram-air inlet, cause the outer part of the boundary layer to roll up [23]. A higher proportion of high momentum airflow was forced into the ram-air inlet [23]. The application of vortex generators significantly decreases the boundary layer thickness, thereby increasing the pressure recovery. The typical improvement in the pressure recovery from the application of vortex generators was found to lie between 35% and 40%.

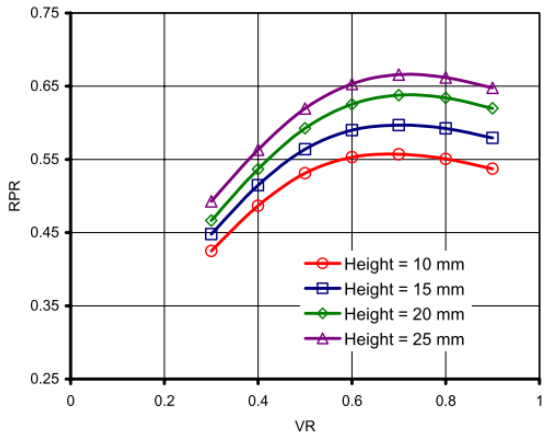

(a) Influence of the vortex generator height. The pressure recovery (RPR) is plotted versus the velocity ratio (VR)

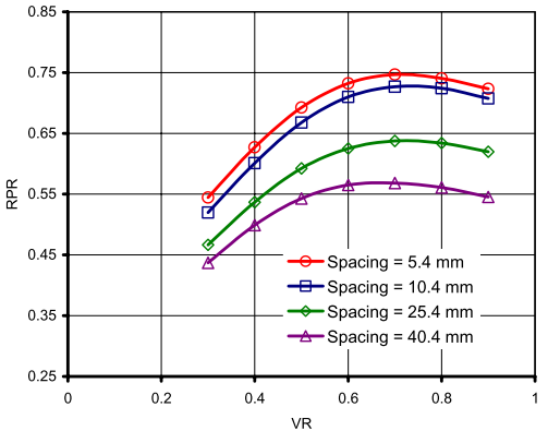

(b) Influence of the vortex generator spacing. The pressure recovery (RPR) is plotted versus the velocity ratio (VR)

Figure 2.6: Influence of design parameters: height and spacing of vortex generators [23]

The lateral spacing of the vortex generators caused an increase in the inlet pressure recovery. This can be explained by the fact that there is a stronger interaction between the inlet and the vortex generators when the lateral spacing is reduced [23]. The pressure recovery reaches its maximum and decreases when a vortex is being ingested into the inlet. Another point to be mentioned is, the shape of the vortex generators does not result in significant differences in performance. One can

take the advantage of choosing the simplest, cheapest shape to be manufactured as the vortex generator.

Perez et al. (2006)

The improvement of the inlet performance with the application of vortex generators has been investigated by Perez (2006) [24]. The pressure recovery of the conventional NACA ram-air inlet has been compared with the NACA ram-air inlet with the application of vortex generators. The area and the angle of attack of the vortex generators were varied.

CFD software FLUENT and the Spalart-Allmaras turbulence model have been used with the following boundary conditions: ambient pressure of 72,428 [Pa], a Mach number of 0.31 and a total temperature of 270.3 [K].

This research shares similar conclusions about the pressure recovery [7]. Perez found that the use of vortex generator on the conventional NACA ram-air inlet compared to the clean conventional NACA ram-air inlet, the maximum relative improvement of the pressure recovery was found to be 58% [24]. The researchers concluded that the vortex generator thins out the boundary layer and thus improves the pressure recovery [23]. For the configurations with varying angle of attack, it showed that a stronger interaction between the anti-rotating vertices occurred when the angle of attack of the vortex generators was increased [24]. The angle of attack of the vortex generator shall equal to 35° in order to achieve the highest gain in inlet performance in terms of pressure recovery. Increasing the area of the vortex generators increases the pressure recovery. However, the application of vortex generators near the inlets leads to higher drag coefficient.

2.3. COMPARISON NACA RAM-AIR INLET VS. PARALLEL-WALLED INLET

This section presents a comparison between NACA ram-air and parallel-walled inlets.

Mossman conducted an experiment on parallel-walled and NACA ram-air inlets in a 5.33[cm]-18.80[cm] wind tunnel at Mach numbers between 0.20 and 0.96 (1949) [20].

The author found that the pressure recovery for the parallel-walled inlet decreased significantly from a Mach number of 0.75. For the NACA ram-air inlet, the pressure recovery decreased significantly at a higher Mach number of 0.94. Mossman used the shadowgraph method to show that shockwaves were formed upstream of the inlet, which resulted in thickening of the boundary layer and thus led to a reduction in pressure recovery [20]. Furthermore, a strong shockwave is able to cause flow separation, leading to a decrease in pressure recovery [20].

Mossman concluded that the difference between parallel-walled and NACA (and the divergent-walled) inlets lies in the fact that the interaction of the shockwave with the boundary layer is less strong for the NACA ram-air inlet compared to the parallel-walled inlet [20]. Due to the three-dimensional flow of the NACA ram-air inlet, the flow of the NACA wall inlet is thinner than the flow of the parallel-walled inlet, which is approximated as a two-dimensional flow [20]. Mossman added that the thinner boundary layer of NACA ram-air inlet is less prone to separate than in the case of the thicker boundary layer of the parallel-walled inlet at a similar adverse pressure gradient.

The inlet performance of the NACA ram-air inlet, in terms of pressure recovery, is superior compared to the parallel-walled inlet. The value of the highest pressure recovery of the NACA ram-air inlet is larger than the highest pressure recovery of the parallel-walled air inlet [21]. The advantage of the parallel-walled inlet is that the pressure recovery is less sensitive to variations of the Mach number [9]. Furthermore, a parallel-walled inlet has the advantage that it is much easier and cheaper to manufacture than a NACA ram-air inlet [23].

The parallel-walled inlet has been investigated by improving the inlet performance with vortex

generators. The goal was to combine both the advantages of the parallel-walled inlet and the NACA ram-air inlet [23]. Results have shown that the vortex generators thin out the boundary layer [23]. Although the drag coefficient increased, it resulted in an improvement of the pressure recovery. It must be mentioned that a vortex core deteriorates the pressure recovery. For this thesis, it is important to inspect the formation of vortices since they affect the performance of the NACA ram-air inlets.

2.4. AERODYNAMIC BACKGROUND

The main objective of this thesis is to perform an aerodynamic analysis on the NACA ram-air inlet in which the conventional flap is replaced by a morphing plate. It is useful to indicate its inlet performance using parameters. In this section, the performance parameters that are used in this thesis are presented.

2.4.1. PRESSURE RECOVERY

The NACA ram-air inlet is designed with the purpose to provide an amount of airflow with minimal disturbance as possible. Therefore, the inlet must allow the recovery of as much of the total pressure in the freestream conditions. The inlet performance is commonly characterised by pressure recovery. This is one of the most important performance parameters. The pressure recovery is the ratio of the inlet ram pressure to the freestream ram pressure. It is defined that the ram pressure is the difference between the total pressure and the static pressure of the incoming airflow [25].

According to the organisation Engineering Sciences Data Unit ESDU report 80037, the loss in pressure recovery is composed of two components [26]:

- *"The loss associated with flow separations which can occur at the lip for some combinations of inlet mass flows and lip geometry" [26]*
- *"The loss associated with the diffuser which results mainly from the boundary-layer growth on the diffuser walls and the effect of the pressure gradient imposed on it by the flow diffusion" [26]*

The sources of pressure losses can be further extended. According to ESDU report 80037, the efficiency of the inlet is given by Equation 2.1 with the sources of the losses [26]. The assumption is that the external shape of the inlet does not affect the inlet pressure losses.

$$\eta = 1 - \Delta\eta_l - \Delta\eta_d N - \Delta\eta_{cst} - \Delta\eta_{csf} \tag{2.1}$$

Where:

Δ_{eta_l} is the efficiency that accounts for the loss in pressure recovery due to flow separation at the lip [-]

Δ_{eta_d} is the efficiency that accounts for the loss in pressure recovery without interaction between the airflow and the diffuser [-]

N is the magnification factor to be applied to $\delta\eta_d$ to account for the diffuser loss [-]

$\Delta\eta_{cst}$ is the efficiency that accounts for the loss due to the wall of the duct upstream of the diffuser [-]

$\Delta\eta_{csf}$ is the efficiency that accounts for the loss due to the wall of the duct downstream of the diffuser [-]

For the case with an inlet, the pressure recovery is defined as the ratio of ram pressure in the freestream flow to the ram pressure at the smallest cross-sectional area inside the NACA ram-air inlet duct, the throat area. The throat area, at which the pressure recovery is calculated, is shown in Figure 2.7. The throat area is located inside the NACA ram-air inlet. The location and size of the throat area vary for different configurations and flap designs.

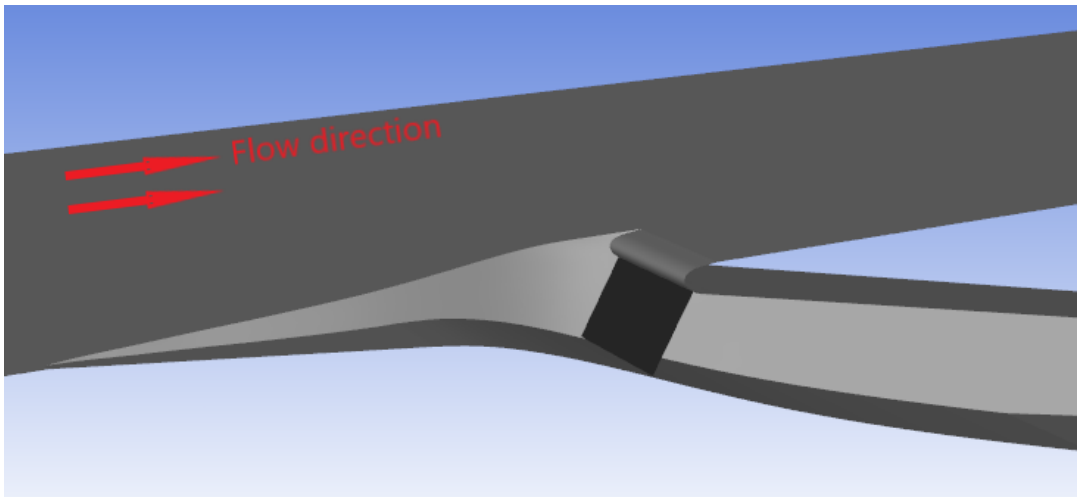

Figure 2.7: Half of the geometry of the NACA ram-air inlet is illustrated. The location of the throat area, at which the pressure recovery is calculated, is shown in black.

Then the pressure recovery η is calculated as follows, by Equation 2.2.

$$\eta = \frac{P_{t_1} - p_{s_0}}{P_{t_0} - p_{s_0}} \tag{2.2}$$

Where P_{t_0} is the total pressure measured in the freestream $[Pa]$, P_{t_1} is the total pressure measured at the throat area $[Pa]$, and P_{s_0} is the static pressure of the freestream $[Pa]$. P_{t_1} can be considered as the total pressure that is recovered inside the inlet.

2.4.2. INLET DRAG

The drag is the second important parameter to define the performance of an inlet. The inlet must be designed such that the drag is as small as possible. According to the research conducted in 1948 by Mossman and Randall, the inlet drag consists of three components [5]. It is assumed that the airflow after entering the duct is aligned with the upstream airflow such that there is no momentum of the outlet air in the direction of the drag. The drag components are listed as follows [5]:

- Loss in the momentum of the entering air at the duct entrance
- Momentum of entering air (ram drag)
- Loss in the momentum behind the duct (profile drag)

The inlet drag for submerged inlets is calculated by using Equation 2.3.

$$D = \int \dot{m_{ent}}(u_0 - u_{ent})\,dA_{ent} + \int \dot{m_{ent}} u_{ent}\,dA_{ent} + \int \dot{m_{aft}}(u_0 - u_{aft})\,dA_{aft} \tag{2.3}$$

Where $\dot{m}$ is the mass flow rate per unit area $[kg/(s \cdot m^2)]$, u is the velocity $[m/s]$, A is the area $[m^2]$, subscript 0 is the freestream, ent is the duct entrance, and aft is the duct outlet.

2.4.3. MASS FLOW RATIO

The mass flow rate that is ingested by an inlet can be utilised to measure the inlet performance [27]. This is usually expressed as the ratio of the mass flow rate that is ingested by the inlet to the mass flow rate of the incoming flow. For auxiliary inlets, the mass flow ratio is defined by mass flow rate $\dot{m}_1$ that is ingested by the inlet through the inlet throat area A_1 to the mass flow in the incoming flow through a streamtube of the equivalent cross-sectional A_1. The inlet mass flow ratio is then calculated by Equation 2.4 [27].

$$\text{mass flow ratio} = \frac{\dot{m}_1}{\dot{m}_0} = \frac{\rho_1 A_1 V_1}{\rho_0 A_0 V_0} \tag{2.4}$$

Where $\dot{m}$ is the mass flow rate $[kg/s]$, u is the flow velocity $[m/s]$, A is the area $[m^2]$. Subscripts 0, and 1 denotes the station that is located upstream of the inlet in the freestream flow and the station that is located at the inlet throat, respectively. These two indicated stations are illustrated in Figure 2.8.

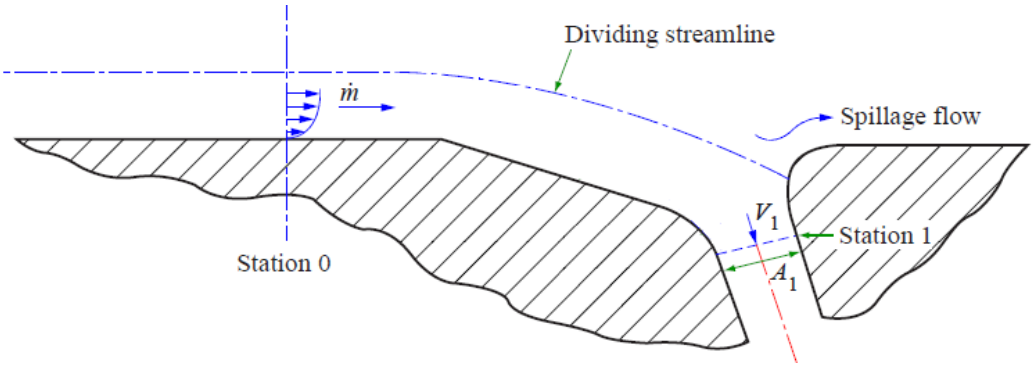

Figure 2.8: Inlet geometry with the entry streamtube [27]

The dividing streamline is also shown in Figure 2.8, retrieved from Report ESDU no.03006, which defines the upper boundary of the streamtube upstream of the inlet duct entrance plane. The height of the dividing streamline is an important parameter on the entry streamtube. Figures 2.9a and 2.9b show the velocity profiles at station 0 with entry streamtube and the dividing streamline for mass flow ratios of 0.8 and 0.2.

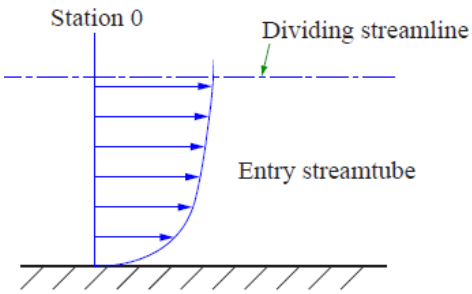

(a) Mass flow ratio $\frac{\dot{m}_1}{\dot{m}_0} = 0.8$

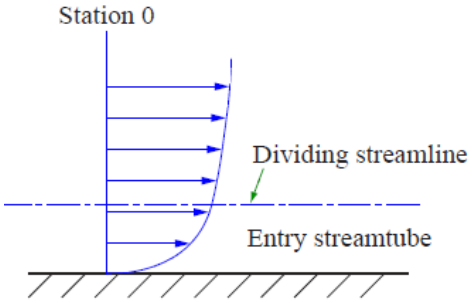

(b) Mass flow ratio $\frac{\dot{m}_1}{\dot{m}_0} = 0.2$

Figure 2.9: The effect of the mass flow ratio on the entry streamtube and dividing streamline [26]

In Figure 2.9a, for mass flow ratio of 0.8, the height of the dividing streamline above the surface of station 0 lies at a certain distance from the surface. As the mass flow ratio decreases from 0.8 to 0.2, the height of the streamtube and thus the cross-sectional area at station 0 also decrease as

shown in Figure 2.9b. When the velocity profile remains the same for both mass flow ratios, the entry streamtube for mass flow ratio of 0.2 contains a higher proportion of low energetic (slow-moving) airflow.

2.4.4. PRESSURE COEFFICIENT

The pressure coefficient C_p is a dimensionless number to express the relative pressures in a flow field. This index is useful to show the differences in pressure in the flow field around the two closure flap designs. The pressure coefficient is calculated using Equation 2.5 [28].

$$C_p = \frac{p - p_\infty}{1/2 \rho V_\infty^2} \tag{2.5}$$

Where p is the static pressure $[Pa]$, p_∞ is the freestream static pressure $[Pa]$, ρ is the density $[kg/m^3]$, and V_∞ is the freestream velocity $[m/s]$.

2.4.5. BOUNDARY LAYER THEORY

From the literature study, it was found that the inlet performance of the NACA ram-air inlet is influenced by the boundary layer. The boundary layer is a thin region of a viscous fluid in which the viscous effects are important. The boundary layer is adjacent to the surface of a solid body, which is in contact with the moving fluid [28]. Figure 2.10 illustrates the different parts of the flow.

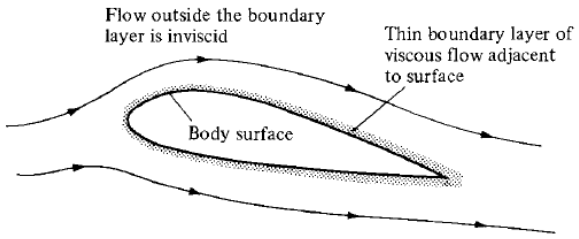

Figure 2.10: The two different regions, thin and thick boundary layer, around a solid body [28]

In this thesis, low-energetic air is pushed away from the NACA duct entrance due to the presence of a part of vortices such that high-energetic air is ingested by the NACA ram-air inlet. Although the height of the boundary layer around an aircraft is relatively small, the height of the boundary layer compared to the duct height of the inlet is significantly large.

The characteristics of the boundary layer depend on the Reynolds number. In order to calculate the Reynolds number, the dynamic viscosity needs to be determined first. The dynamic viscosity μ is a function of the total temperature and is given by Sutherland's law in Equation 2.6 [29].

$$\mu = \mu_{ref} \left(\frac{T}{T_{ref}} \right)^{3/2} \frac{T_{ref} + S}{T + S} \tag{2.6}$$

Where T is the absolute total temperature in $[K]$, μ_{ref} is the viscosity 1.716e-5 $[kg/ms]$, T_{ref} is the reference temperature of 273.15 $[K]$, and S is the Sutherland reference temperature 110.4 $[K]$.

The Reynolds number can then be calculated using Equation 2.7 [28].

$$Re = \frac{\rho u x}{\mu} \tag{2.7}$$

Where ρ is the density $[kg/m^3]$, u is the freestream velocity $[m/s]$, x is the characteristic length $[m]$, and μ is the dynamic viscosity $[kg/(ms)]$.

The boundary layer is mathematically defined as the distance as one moves away from the wall of the solid body to this outer edge layer where the velocity equals $0.99 \cdot u_{\text{inf}}$ [28]. The height of the boundary layer can be estimated by the Blasius' solution in which it assumes that the pressure in the boundary layer is constant through the height of the boundary layer. The boundary layer thickness δ of a turbulent boundary layer on a flat plate is approximated by Equation 2.8.

$$\delta = \frac{0.37x}{Re_x^{1/5}} \tag{2.8}$$

Where x is the length of the plate and Re is the Reynolds number.

2.4.6. CHOKED FLOW

Since the NACA ram-air inlet possesses a constriction inside the duct channel, downstream of the lip, the NACA ram-air inlet can be considered similar to a convergent-divergent nozzle. The mass flow rate that can be ingested by the NACA ram-air inlet can be limited by certain flow conditions. The condition at which the flow is sonic, the mass flow rate will not increase whilst the backpressure downstream of the throat increases. This is called the choked condition [28]. In this condition, the mass flow rate remains constant when the backpressure is increased. This particular mass flow rate for the choked condition will be avoided in the NACA ram-air inlet.

In order to calculate the mass flow rate at which the flow is choked, the continuity equation is rewritten as follows in Equation 2.9.

$$\dot{m} = \rho A u \tag{2.9}$$

The velocity u in Equation 2.9 can be expressed as a function of the speed of sound to take into account the compressibility effects, resulting in Equation 2.10:

$$\dot{m} = \rho A M \sqrt{\gamma R T} \tag{2.10}$$

Where ρ is the density $[kg/m^3]$, A is the area $[m^2]$, M is the Mach number, γ is the ratio of specific heats of air, R is the specific gas constant, and T is the temperature.

The driving fluid in CFD is air and it is assumed to be an ideal gas, from the equation of state the density is expressed in Equation 2.11:

$$\rho = \frac{P}{RT} \tag{2.11}$$

By substituting the density from the equation of state of Equation 2.11 into Equation 2.12.

$$\dot{m} = \frac{P}{RT} A M \sqrt{\gamma R T} \tag{2.12}$$

The isentropic relation of the static and total pressure is given by Equation 2.13 :

$$\frac{P}{P_t} = \left(\frac{T}{T_t}\right)^{\frac{\gamma}{\gamma-1}} \tag{2.13}$$

Substituting the isentropic relation of the pressure in Equation 2.13 into Equation 2.12 yields:

$$\dot{m} = P_t \left(\frac{T}{T_t}\right)^{\frac{\gamma}{\gamma-1}} \frac{1}{RT} AM\sqrt{\gamma RT} \tag{2.14}$$

By rearranging Equation 2.15 yields the following equation:

$$\dot{m} = \frac{P_t}{\sqrt{T_t}} \sqrt{\frac{\gamma}{R}} AM \left(\frac{T}{T_t}\right)^{\frac{(\gamma+1)}{2(\gamma-1)}} \tag{2.15}$$

The isentropic relation of the static and total temperature is given by Equation 2.16.

$$\frac{T}{T_t} = \left(1 + \frac{\gamma-1}{2} M^2\right)^{-1} \tag{2.16}$$

Then, substituting Equations 2.16 into Equation 2.15 gives the equation to calculate the mass flow rate:

$$\dot{m} = \frac{P_t}{\sqrt{T_t}} \sqrt{\frac{\gamma}{R}} AM \left(1 + \frac{\gamma-1}{2} M^2\right)^{\frac{-(\gamma+1)}{2(\gamma-1)}} \tag{2.17}$$

The choked mass flow rate, at which the sonic condition Mach=1 is reached, can be calculated using Equation 2.18:

$$\dot{m}_{choked} = \frac{P_t}{\sqrt{T_t}} \sqrt{\frac{\gamma}{R}} A_{throat} \left(1 + \frac{\gamma-1}{2}\right)^{\frac{-(\gamma+1)}{2(\gamma-1)}} \tag{2.18}$$

Equation 2.18 was used to determine the mass flow rate at which the flow is choked at the throat for different configurations. This value was calculated and used as the upper limit of the mass flow outlet in the CFD simulations. The range of mass flow rates that were analysed for each configuration has a maximum value of 80% of the choked mass flow rate.

2.4.7. TURBULENCE QUANTITIES

For the setup of the CFD simulation in Ansys Fluent, setting up appropriate boundary conditions is a very important step [30]. It can severely affect the performance of the CFD simulation. Several turbulence quantities were required to be specified in Ansys Fluent. If possible, those quantities are preferably obtained from experiments. The calculations that are required for determining the turbulence quantities are presented in this Subsection.

Turbulence length scale

The physical size of the large eddies that contains the turbulence kinetic energy is defined by the turbulence length scale l. The turbulence length scale for Fluent can be estimated with Equation 2.19 [31].

$$l_{turbulent} = 0.07L \tag{2.19}$$

Where L is the characteristic length $[m]$. The characteristic length L is limited due to the size of a ducted channel. For the NACA ram-air, the length of the NACA S-shaped contour parallel with the freestream direction determines the size of the vortices that are generated by the sharp edges of the NACA ram-air inlet.

Turbulence intensity

Another parameter that is required for the setup of the CFD simulation in Fluent is the turbulence intensity. The turbulence intensity is defined as the ratio of the velocity fluctuation over the root mean square of the velocity vector [32]. A turbulence intensity above 0.10 is considered to be high.

The turbulence intensity is a function of the Reynolds number and can be estimated using Equation 2.20 [33].

$$I_{internal} = 0.16Re^{-1/8} \tag{2.20}$$

Where Re is the Reynolds number.

Turbulent kinetic energy

Once the turbulence intensity has been calculated from Equation 2.20 the initial value of turbulent kinetic energy k can be determined. The turbulent kinetic energy is defined as the kinetic energy per unit mass of the turbulent velocity fluctuations of the flow.

$$k = \frac{3}{2}(UI)^2 \tag{2.21}$$

Where I is the turbulence intensity found in Equation 2.20 and U is the freestream velocity $[m/s]$.

Turbulent dissipation rate

The specific turbulent dissipation rate ω is calculated using Equation 2.22 [31].

$$\omega = \frac{\sqrt{k}}{C_\mu l} \tag{2.22}$$

Where C_μ is a constant of 0.09, k is the turbulent kinetic energy $[J/kg]$ and l is the turbulent length scale $[m]$.

3

METHODOLOGY

Since the goal of this thesis is to analyse the aerodynamic effects of the NACA ram-air inlet by replacing the conventional closure flap mechanism with a hinged flap by a morphing flap through CFD simulations, the methodology to prepare and execute CFD analysis will be explained in this chapter. First of all, the use of numerical modelling will be explained in Section 3.1. Then the software packages that were used are discussed in Section 3.2. The physical model of the aircraft component, the NACA ram-air inlet, was required to be modelled into a computational model. The measurements of the dimensions of the NACA ram-air inlet and the definitions of the NACA ram-air inlet parts are explained in Section 3.3. The test cases that were simulated in CFD and the Computer-Aided Design (CAD) geometry models of different configurations that were created will be explained in Section 3.4. This is followed by Section 3.5 in which the definitions of the main mesh attributes are stated. The computational domains and operating conditions were required to be determined, which are discussed in Section 3.6.

3.1. NUMERICAL MODELLING

Simulations in Computational Fluid Dynamics were performed in the thesis project to analyse the NACA ram-air inlet with a single morphing flap. CFD is extensively used in the research and development departments of industrial companies to analyse and design engineering applications with fluids. The fluid physics are numerically solved in CFD [34]. In order to conduct CFD simulations, the governing equations which define the fluid physics need to be understood. The governing equations of CFD are explained in Subsection 3.1.1. This is followed by Subsection 3.1.2 in which the turbulence modelling by applying the Reynolds decomposition to the governing equations is discussed.

3.1.1. GOVERNING EQUATIONS

Turbulence is described by a mathematical model, the set of governing equations of fluid dynamics along with its boundary conditions [35]. The motion of a viscous fluid is governed by three basic laws of mass, momentum and energy [35]. Each physical principle is stated below.

- Conservation of Mass
- Conservation of Momentum
- Conservation of Energy

The mathematical representations of the three laws of conservation are the continuity equation, the momentum equation, and the energy equation. These three equations are known as the complete Navier-Stokes equations. Each mathematical model corresponding to the conservation law is described briefly.

CONSERVATION OF MASS

The conservation of mass states that mass cannot be created or destroyed in a closed system. The total mass remains constant. The equation for the continuity equation is shown in Equation 3.1 [36].

$$\frac{\partial \rho}{\partial t} + \nabla \cdot (\rho \vec{V}) = 0 \tag{3.1}$$

CONSERVATION OF MOMENTUM

The conservation of momentum follows from Newton's second law, which states that in a closed system the change of momentum in a fluid is equal to the sum of the forces acting on it. Two types of forces are distinguished for a fluid, the surface forces and the body forces [35]. The momentum equations in Cartesian coordinates are shown in Equations 3.2, 3.3, and 3.4 [36].

$$\frac{\partial \rho u}{\partial t} + \nabla \cdot (\rho u \vec{V}) = -\frac{\partial p}{\partial x} + \frac{\partial \tau_{xx}}{\partial x} + \frac{\partial \tau_{yx}}{\partial y} + \frac{\partial \tau_{zx}}{\partial z} + \rho f_x \tag{3.2}$$

$$\frac{\partial \rho v}{\partial t} + \nabla \cdot (\rho v \vec{V}) = -\frac{\partial p}{\partial y} + \frac{\partial \tau_{xy}}{\partial x} + \frac{\partial \tau_{yy}}{\partial y} + \frac{\partial \tau_{zy}}{\partial z} + \rho f_y \tag{3.3}$$

$$\frac{\partial \rho w}{\partial t} + \nabla \cdot (\rho w \vec{V}) = -\frac{\partial p}{\partial z} + \frac{\partial \tau_{xz}}{\partial x} + \frac{\partial \tau_{yz}}{\partial y} + \frac{\partial \tau_{zz}}{\partial z} + \rho f_z \tag{3.4}$$

CONSERVATION OF ENERGY

The conservation of energy states that energy in a closed system cannot be created or destroyed. The rate of change of the energy of the fluid is equal to the sum of the work done by the fluid and the heat added to the fluid, this is dictated in Equation 3.5 [36].

$$\begin{aligned}
\frac{\partial}{\partial t}\left[\rho\left(e+\frac{V^2}{2}\right)\right] + \nabla \cdot \left[\rho\left(e+\frac{V^2}{2}\right)\vec{V}\right] = {} & \rho\dot{q} + \frac{\partial}{\partial x}\left(k\frac{\partial T}{\partial x}\right) + \frac{\partial}{\partial y}\left(k\frac{\partial T}{\partial y}\right) + \frac{\partial}{\partial z}\left(k\frac{\partial T}{\partial z}\right) + \\
& - \frac{\partial (up)}{\partial x} - \frac{\partial (vp)}{\partial y} - \frac{\partial (wp)}{\partial z} \\
& + \frac{\partial (u\tau_{xx})}{\partial x} + \frac{\partial (u\tau_{yx})}{\partial y} + \frac{\partial (u\tau_{zx})}{\partial z} \\
& + \frac{\partial (v\tau_{xy})}{\partial x} + \frac{\partial (v\tau_{yy})}{\partial y} + \frac{\partial (v\tau_{zy})}{\partial z} \\
& + \frac{\partial (w\tau_{xz})}{\partial x} + \frac{\partial (w\tau_{yz})}{\partial y} + \frac{\partial (w\tau_{zz})}{\partial z} \\
& + \rho \vec{f} \cdot \vec{V}
\end{aligned} \tag{3.5}$$

3.1.2. TURBULENCE MODELLING

A method to solve the Navier-Stokes equations is the Direct Numerical Simulation (DNS) [35]. All turbulence length scales are simulated in DNS. The high Reynolds number of the NACA ram-air inlet makes DNS simulations not suitable. An aircraft operates in the flow regime with a Reynolds number in the order of 10^6. The limitation of this method is that the computational cost to capture all turbulence motions around the NACA ram-air inlet is too high. The temporal and spatial requirements are the limiting factors of DNS [37]. Large Eddy Simulation (LES) overcomes the limitations of DNS [35]. When a high Reynolds number and complex geometry are the limiting factors for the application of DNS, Large Eddy Simulation (LES) can be used. LES is less costly than DNS since it does not simulate the small-scale structures. Another method to calculate viscous flows is the Reynolds-averaged Navier-Stokes (RANS) equations. RANS simulations are less expensive than LES simulations. For this thesis, the CFD simulations were performed in RANS.

In order to solve the Navier-Stokes equations, the RANS equations are used to describe turbulent flow in this thesis. The main principle of RANS is to decompose a flow variable into a time-averaged value and the fluctuating value, this is called the Reynolds decomposition [34]. The Reynolds decomposition is defined as follows [35]:

$$u(x_i, t) = \bar{u}(x_i, t) + u'(x_i, t) \tag{3.6}$$

Where u is the flow parameter, $\bar{u}$ is the time-averaged value of the flow parameter, u' is the fluctuating quantity of the flow parameter.

The Reynolds decomposition is applied to the Navier-Stokes equations, which leads to the RANS equations shown in Equation 3.7 and 3.8 [38].

$$\frac{\partial \langle \underline{u} \rangle}{\partial t} + \nabla \cdot (\langle \underline{u} \rangle \langle \underline{u} \rangle) + \frac{1}{\rho} \nabla \langle p \rangle - \frac{1}{Re} \nabla \cdot \nabla \langle \underline{u} \rangle = -\nabla \cdot \langle \underline{u}' \underline{u}' \rangle \tag{3.7}$$

$$\nabla \cdot \underline{u} = 0 \tag{3.8}$$

The Reynolds stress tensor arises on the right side of Equation 3.7 after the Reynolds decomposition has been applied to the Navier-Stokes equations. The Reynolds stress tensor is shown in Equation 3.9.

$$\tau_{ij} \equiv -\left\langle u_i' u_j' \right\rangle \tag{3.9}$$

The Reynolds stress tensor is a non-linear term and it introduces a new problem where the number of unknowns is more than the set of equations [38]. Due to the introduction of the Reynolds stress tensor shown in Equation 3.9, the RANS equations are not a closed set. Therefore, additional equations that represent the turbulent properties of the flow, are required for the Reynolds stress tensor to solve the closure problem [34]. These approximations for the Reynolds stress tensor are known as the turbulence models.

TURBULENCE MODELS

It is required to choose a turbulence model for the RANS simulations. There exists a large number of turbulence models. It is important to know the advantages and limitations of each turbulence model. The commonly used turbulence models $k-\epsilon$, $k-\omega$, and $k-\omega\,SST$ will be discussed. First, the turbulence models $k-\epsilon$ and $k-\omega$ will be explained, and it will eventually lead to the Menter's SST model that was used for the CFD simulations.

$k-\epsilon$ model The $k-\epsilon$ model is a widely used turbulence model [32] [39]. In this model, partial differential equations for the turbulence kinetic energy k and the dissipation rate ϵ are solved. It is assumed that there exists an equilibrium between turbulence production and dissipation [38]. The model is suitable for external aerodynamic problems. It should not be used on flows with strong adverse pressure gradients, strong curvature and flow separation [32].

$k-\omega$ model $k-\omega$ model is also commonly used turbulence model. It is a two-equation model in which the turbulence kinetic energy k and the postulated transport equation for the specific turbulence dissipation rate ω are solved in this model. The model gives good results for boundary layer flows and flows with pressure gradients and separation [23] [38]. The model is very sensitive to inflow and freestream boundary conditions [38]. For this reason, the $k-\epsilon$ turbulence model is better than the $k-\omega$ turbulence model for external aerodynamics.

Menter SST model The Menter Shear Stress Transport (SST) combines the advantages of the two turbulence models $k-\epsilon$ and $k-\omega$ [32] [40]. This model uses the $k-\epsilon$ in the freestream flow, far from the no-slip boundaries and switches to the $k-\omega$ model in the inner parts of the boundary layer. This avoids the problem with the $k-\omega$ model, which is sensitive to inflow and freestream boundary conditions [40]. The SST turbulence model was used in the study of Menon on NACA ram-air inlets since SST model provides good results for critical areas like the boundary layer: adverse pressure gradients near the walls of the NACA inlets were expected [41].

The Menter $k-\omega\,SST$ turbulence model was used for the steady-state CFD simulations of this thesis project. For the aerodynamic analysis of the NACA ram-air inlet, it is important to capture the boundary layer accurately since the boundary layer flow around the NACA ram-air inlet affects the inlet performance. This will be formulated by the $k-\omega$ model of the SST model, which is more superior in the boundary layer than the $k-\epsilon$ model [40]. The $k-\epsilon$ formulation will be used in the free-shear layers and outer boundary layer regions, eliminating the problem with the free shear flow boundary conditions of the $k-\omega$ model [42]. The shear stress transport correction of the $k-\omega\,SST$ model improves the prediction of flow separation due to adverse pressure gradients [42]. The flow field around the geometry of the NACA ram-air inlet, especially around the lip and inside the NACA ram-air tunnel at the throat area is very complex and will benefit from this accuracy advantage.

3.2. SOFTWARE

For this thesis, several software packages are required for the pre-processing, processing and post-processing of CFD simulations. The first step of a CFD problem is to create a CAD geometry and the computational domain of the physical model. This was done by creating different geometries in the CAD software CATIA. The geometry of the NACA ram-air inlet in CATIA was modelled such that the hinged flap and the morphing flap will change its shape due to actuator extension. ANSYS DesignModeler was used in order to apply small modifications to the geometry such that the geometries were clean solids [30].

After the geometries were created, the following step was to generate a mesh for each geometry. The generation of meshes is an important step in CFD since it splits the physical domain into a finite number of discrete volumes. ANSYS Meshing, which is a mesh analysis software tool integrated in ANSYS CFX, was used for the meshing [30]. In the pre-processing part of CFD, the generated meshes were imported into the solver ANSYS Fluent in which the CFD problem was solved [30]. The solver parameters and boundary conditions were required to be set up in order to solve the CFD problem. After the solver has completed the simulation, the succeeding step is the post-processing of the CFD results which are assessed and post-processed in Tecplot 360 [43].

3.3. GEOMETRY OF NACA RAM-AIR INLET

This section provides a full description of the geometry that is simulated using CFD software. The NACA ram-air inlet is geometry studied in this master thesis. No information of the lip shape and dimensions of the inlet has been given by the manufacturer or could be found on the internet, but a used NACA ram-air inlet of an Airbus A320 by Airbus has been provided for research purposes. Figure 3.1 shows the side view of the real NACA ram-air inlet.

Figure 3.1: Side view of the NACA ram-air inlet of the Airbus A320. The flow direction is indicated with red arrows.

Figure 3.2 shows the isometric view of the real NACA ram-air inlet with the hinged line indicated by the red box. The original hinged flap is located inside the NACA ram-air inlet and is attached to the ram-air inlet at the hinged line with countersunk bolts. Figure 3.3 shows the water injector inside the NACA ram-air inlet. The water ejector sprays water in the ram-air inlet system in order to increase the cooling efficiency of the ram-air [44].

Figure 3.2: Isometric view of the NACA ram-air inlet of the Airbus A320 with the location of the 'axis of rotation' indicated by the red box.

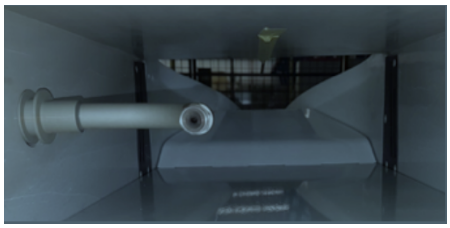

Figure 3.3: The water injector inside the NACA ram-air inlet of the Airbus A320 [3]

The dimensions of the NACA ram-air inlet were obtained by measurement using simple measurement tools such as a measuring tape and a calliper. The calliper was used to measure the dimensions of the lip of the inlet accurately. The recorded dimensions of the NACA ram-air inlet can be found in Appendix A.

Each part of the NACA ram-air inlet needs to be defined. Figures 3.4 and 3.5 show the inlet part names of the isometric, top and side view of the NACA ram-air inlet, respectively. Figure 3.5 shows the location of the 'axis of rotation' which is defined as the hinge line at which the closure flap rotates due to deflection of the actuator.

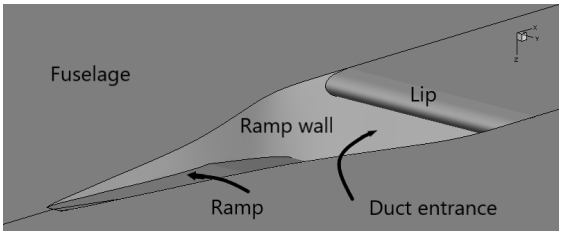

Figure 3.4: Isometric view of the NACA ram-air inlet with definitions

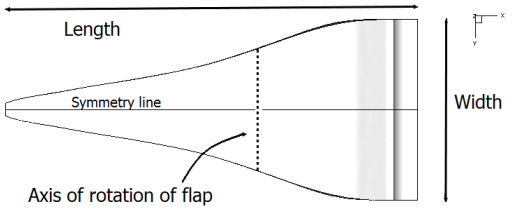

Figure 3.5: Top view of the NACA ram-air inlet with definitions

Figure 3.6 shows the side view of the NACA ram-air inlet. The original hinged flap or the morphing flap is located in the NACA ram-air inlet and it is attached to the ram-air inlet at the hinged line with countersunk bolts. For clarity, the term 'axis of rotation of the flap' and 'rotation point of the flap' will be used to indicate this hinge line. The throat area is defined as the smallest cross-sectional area inside the NACA ram-air inlet duct. The throat area varies due to the deflection of the actuator that determines the opening sizes of different configurations.

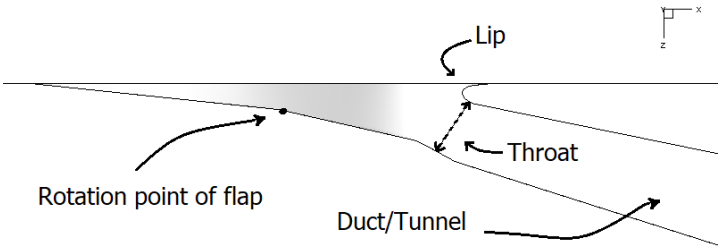

Figure 3.6: Side view of the NACA ram-air inlet with definitions

In addition to Figure 3.6, Figure 3.7 presents the side view of the NACA ram-air inlet with the hinged flap. It shows the definitions of the two kinks on the hinged flap. One kink is located in the middle of the first rigid plate, called Kink no.1. The second kink is located at the hinge between the rigid plates of the conventional closure flap, called Kink no.2. The red/black arrow illustrates the movement of the flap due to the deflection of the actuator. The opening is defined as the minimal distance between the lip and the closure flap, which is controlled by the deflection of the actuator. When the closure flap is deflected upwards from the current position coloured in black to its new position coloured in red, the opening/throat reduces its size. For the case with a morphing flap, Kink no.1 and Kink no.2 are not present since the kinks are smoothed out by the morphing plate.

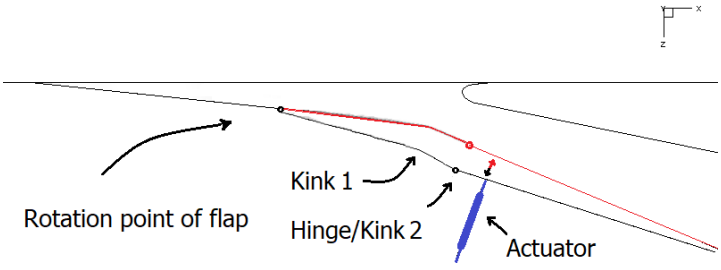

Figure 3.7: Side view of the NACA ram-air inlet with the deflected state of the conventional closure flap

After the dimensions of the NACA ram-air inlet were determined, the dimensions were used to create the CAD models of the NACA ram-air inlet. However, an extra step was required since the CAD models were not fully constrained and were also determined on different flap designs and configurations. This will be explained in the next section.

3.4. TEST CASES

The effects of the closing flap mechanism on the aerodynamic performance of the NACA ram-air inlet have not been researched yet, therefore a number of configurations were tested and analysed at different operating settings. Since no information on the flap deflection and operating settings were given by the manufacturer of the NACA ram-air inlet, assumptions were made. This section discusses the three aspects in which the test cases were varied: the flap designs, the configurations, and the mass flow rates.

3.4.1. HINGED AND MORPHING FLAPS

The goal of this thesis project is to analyse and identify the performance of the NACA ram-air inlet by replacing the conventional closure flap mechanism with hinged flap by a morphing (laminate) flap. The conventional hinged flap design is the baseline model, whereas the morphing flap is proposed as the new model, meaning that two different sets (of configurations) of flap designs were analysed. The two flap designs are illustrated in Figure 3.8.

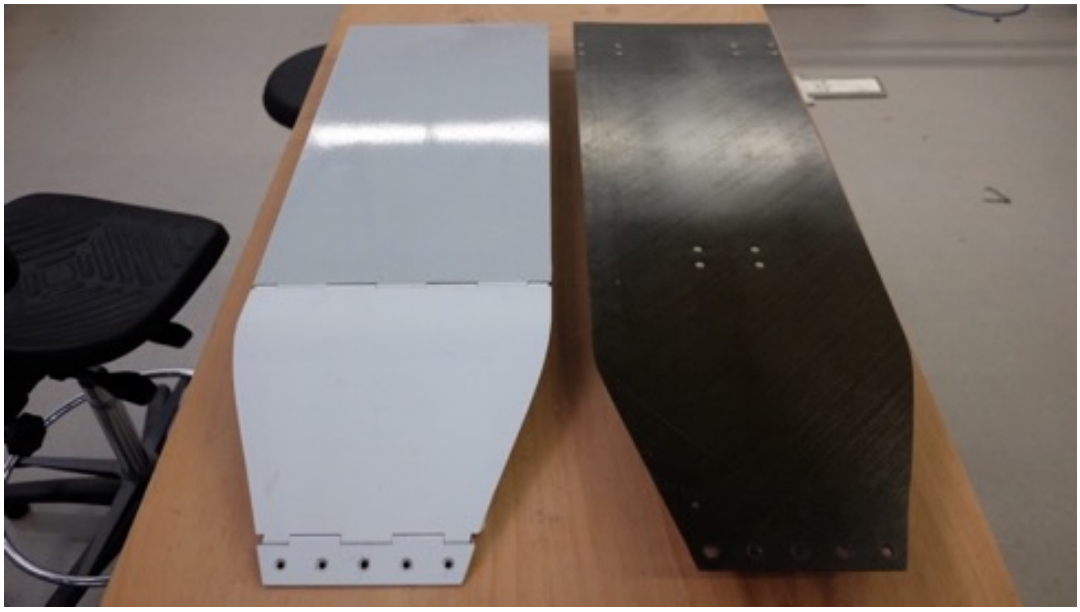

Figure 3.8: Hinged flap (conventional design), consisting of two rigid plates (attachment strip with holes not included), is illustrated on the left side. Morphing flap (novel design) is illustrated in black on the right side. The flaps are attached with countersunk bolts to the NACA ram-air inlet at the 'axis of rotation'. - Courtesy of R.Vos

The 'old' and 'new' flap designs are summarised as follows:

- **Hinged flap cases:** For the case that has the rigid hinged flap (conventional) as the closing flap mechanism inside the NACA ram-air inlet, the rigid plates were modelled in CATIA with kinematics in order to deflect the hinged flap as result of the movement of the actuator. Various configurations with different openings can be analysed. The described hinged flap is illustrated on the left in Figure 3.8.
- **Morphing flap cases:** For the case that has the morphing flap as the closing flap mechanism inside the NACA ram-air inlet, the real NACA ram-air inlet without the flap mechanism was modelled in CATIA. Since three configurations for both hinged and morphing designs were planned to be analysed the curve of the laminates with its corresponding deflection has been acquired from experimental bending tests. The morphing (laminate) flap is illustrated on the right in Figure 3.8.

3.4.2. CONFIGURATIONS

The configurations are the second aspect in which the test cases were varied. For the (near) closed condition for the cruise condition, the hinged flap was matched with the trace lines due to wear inside the NACA ram-air inlet in order to determine the opening between the rigid plate and the lip/inlet ceiling. The distance was measured to be 15 $[mm]$. The open condition was more straight forward. The actuator of the rigid plate was fully retracted from the lip/inlet ceiling and the opening was measured to equal 95 $[mm]$. The midway condition is in the middle of the closed and open condition. This equals to an opening of 55 $[mm]$. The three configurations are summarised as follows in Table 3.1:

Table 3.1: The three configurations of the NACA ram-air inlet in which the opening size at the throat was varied

Configuration	Description	Opening at throat section [mm]
1	(closed)	15
2	(midway)	55
3	(open)	95

For the hinged flap, the kinematics were created in CATIA such that the flap moves to its desired opening position. For the morphing flap, shown in Figure 3.9, the flap was mounted to the 'axis of rotation', indicated in Figure 3.2.

Figure 3.9: Morphing (laminate) flap. The morphing flap is attached with countersunk bolts to the NACA ram-air inlet at the 'axis of rotation'

The morphing flap was deflected by using an actuator such that the shape of the morphing flap will be reshaped, resulting in a change of the opening size inside the NACA ram-air inlet. The curves

of the morphing flap for the three different configurations were acquired from bending tests and are shown in Figure 3.10 [3].

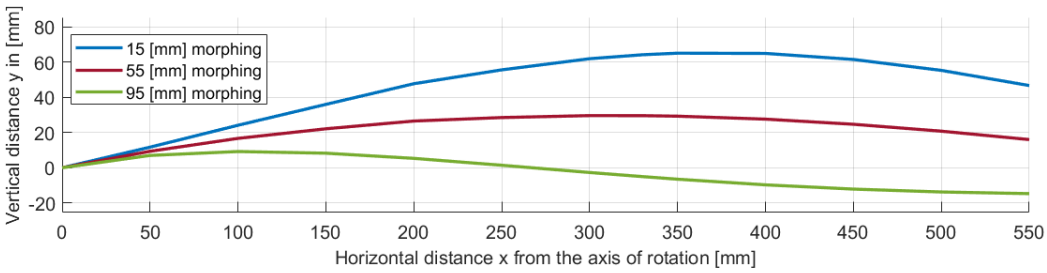

Figure 3.10: The three different shapes of the morphing flap due to deflection

The different configurations with morphing flaps were created in CATIA. The curve was extended with a spline to the end of the NACA ram-air inlet, where the heat exchangers of the ECS are located, with the goal to make the geometry continuous and suitable for CFD simulations.

CAD models

Based on the measurement of the dimensions of the NACA ram-air inlet in Section 3.3 and the information on the flap designs and the configurations explained earlier in this Section, the geometries were created. Both hinged and morphing flap designs for all three configurations were created in CATIA, meaning a total of six geometrically different CAD models were generated for this thesis. Figures 3.11, 3.12, and 3.13 presents the comparison of hinged and morphing flaps of configurations 1, 2, 3, respectively. The fuselage skin, on which the NACA ram-air inlet is attached to, was modelled as a flat plate for simplicity. Only the geometry around the NACA ram-air inlet is shown. The actual CAD model in CATIA is much larger in size. This will be explained in Subsection 3.6 on boundary conditions and computational domain. The dimensions of the geometry away from the NACA ram-air inlet are identical, therefore only the close-up of the NACA ram-air inlet is displayed. In Figure 3.11, Configuration 1 with an opening of 15 $[mm]$ with hinged flap and morphing flap are presented.

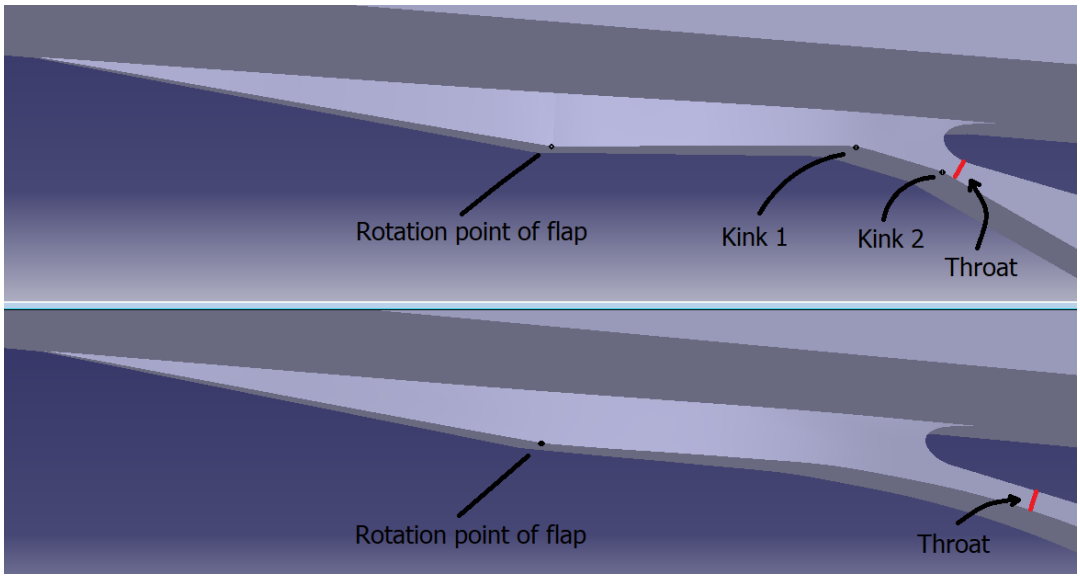

Figure 3.11: Close-up of the NACA ram-air inlet. Top: Configuration 1 with an opening of 15 $[mm]$, with hinged flap. Bottom: Configuration 1 with an opening of 15 $[mm]$, with morphing flap.

It can be seen from the top part of Figure 3.11 that the NACA ram-air inlet with hinged flap shows a very pronounced kink on the closure flap, beneath the NACA ram-air lip. This kink, Kink no.2, has been proven to be the source for an undesired aerodynamic effect that triggers the onset of flow separation and thus pressure losses [3]. Furthermore, when looking closely to the image of the NACA ram-air inlet with hinged flap, one can see that there are two more kinks in the geometry. The first one is located slightly upstream of the hinged flap, midway of the first rigid flap plate. This was indicated as Kink no.1. Another kink is located at the 'rotation point' at which the flap is mounted to the NACA ram-air inlet. Moreover, it can be seen that the throat area in the configuration with the morphing flap is moved more downstream in the duct. In this configuration, the morphing flap comes in contact with the water injector that is located inside of the NACA ram-air inlet, previously shown in Figure 3.3. The water injector restricts the movement of the morphing flap in this configuration, causing the throat area to be moved more downstream.

In Figure 3.12, Configuration 2 with an opening of 55 $[mm]$ with hinged flap and morphing flap are presented.

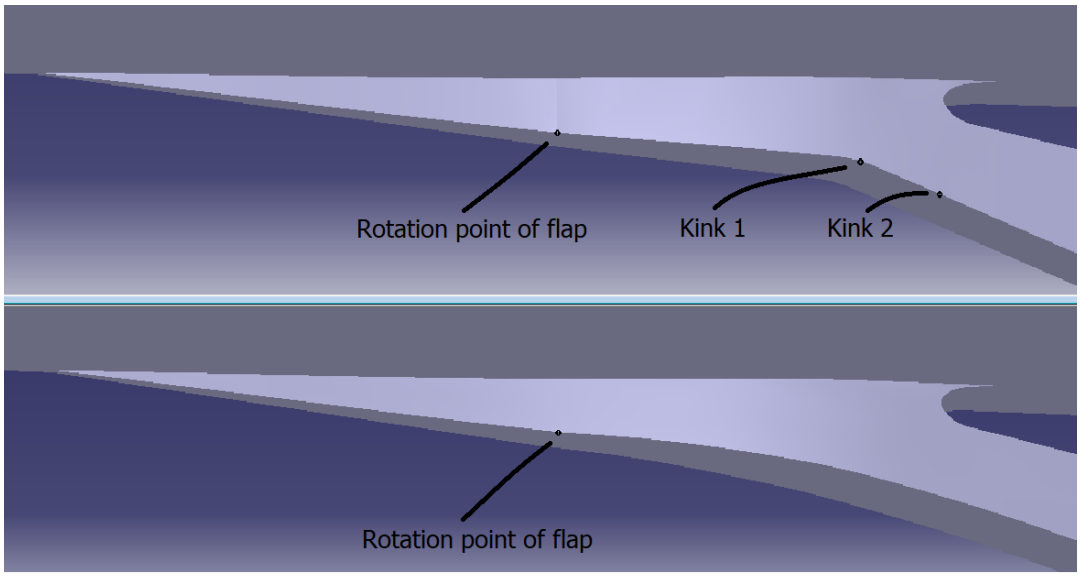

Figure 3.12: Close-up of the NACA ram-air inlet. Top: Configuration 2 with an opening of 55 $[mm]$, with hinged flap. Bottom: Configuration 2 with an opening of 55 $[mm]$, with morphing flap.

From the observation of the top part of Figure 3.12, it can be seen that Kink no.2 between the rigid plates is hardly present for this flap deflection. For this particular flap deflection, Configuration 2 with an opening of 55 $[mm]$ with hinged flap does not introduce a sharp kink at Kink no.2. By looking at the bottom part of Figure 3.12, Kink no.1 and Kink no.2 have been eliminated in the morphing flap as expected. Furthermore, the geometry of the morphing flap around the 'rotation point of the flap' is very smooth.

In Figure 3.13, Configuration 3 with an opening of 95 [mm] with hinged flap and morphing flap are presented.

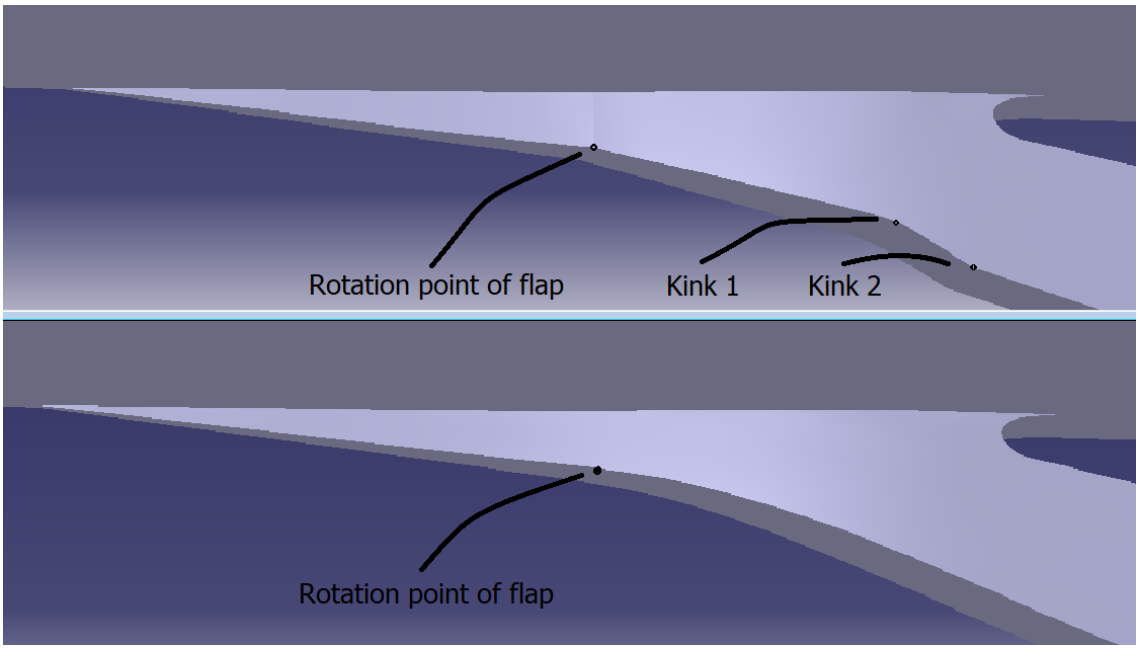

Figure 3.13: Close-up of the NACA ram-air inlet. Top: Configuration 3 with an opening of 95 [mm], with hinged flap. Bottom: Configuration 3 with an opening of 95 [mm], with morphing flap.

From Figure 3.13 it can be seen that a strong kink between the rigid hinged plates is present in the hinged flap case, indicated as Kink no.1. This is a concave kink, whereas Kink no.2 between the rigid hinged plates for Configuration 3 is a convex kink. The kink at the 'rotation point of the flap' is also rather strong. In the morphing case, Kink no.1 and Kink no.2 are eliminated and smoothed out. Furthermore, a subtle kink is located at the 'rotation point of the flap'.

3.4.3. MASS FLOW RATES

In order to analyse the aerodynamic performance of the NACA ram-air inlet with two different flap design and three different configurations, a number of mass flow rates for the mass flow outlet were selected to be analysed. Since the opening size of each configuration varies, the choked mass flow rates are different. For the practical reason, the assumption is that the mass flow rates were chosen such that the choked conditions at the throat section of the NACA ram-air inlet has not been reached. The mass flow rates of each configuration that were simulated are summarised in Table 3.2:

Table 3.2: Mass flow rates of each Configuration

Configuration	Mass flow rate [kg/s]	Mass flow rate range [kg/s]
1	0.025	0.050 - 0.400 with a step size of 0.050
2	0.100	0.250 - 1.500 with a step size of 0.250
3	0.100	0.500 - 2.500 with a step size of 0.500

3.5. MESH

Once the CAD models were created in CATIA and modified in AnsysModeler, the next step was to generate a set of meshes. The mesh generation was done by using ANSYS Meshing. In this section, the approach for the meshing will be presented.

In ANSYS Meshing, the setting for the global cell size covers much of the mesh regions where no meshing rules are imposed on. This means that any mesh rule that is linked with a cell size will be equal or less to the global cell size. The mesh that was used for the CFD simulations is a hybrid grid: both structured and unstructured portions are combined into one single mesh. In general, the mesh generation followed the unstructured meshing approach for most regions of the domain due to the complexity of the CAD model. A very complex part is the transition between the NACA ram-air lip and the ramp walls. This resulted in a very skewed part of the geometry.

Figure 3.14a shows the isometric view of the entire mesh domain. For the unstructured mesh, a cell size (smaller than the global cell size) is chosen in regions where high flow gradients are expected. Figure 3.14b zooms in onto the vicinity of the NACA ram-air inlet in which small cells can be seen. It is expected that vortices are generated around the sharp edge of the NACA ram-air inlet and the NACA ram-air lip. Therefore, a local refinement around the edge of the NACA ram-air inlet was required. This step was done by specifying a body of influence in order to control local mesh refinement. Any region that overlaps with the body of influence will obtain the specified cell size. In Figure 3.14b, a body of influence along the fuselage in the vicinity of the NACA ram-air inlet was placed. This is illustrated as a 'tube' with very small cells. Furthermore, due to the neighbouring walls inside the NACA ram-air inlet, the location of the small cross-sectional area inside the NACA ram-air inlet (throat area) required a local refinement by using a body of influence. Moreover, a local refinement was applied to the duct downstream of the NACA ram-air inlet since it is expected that the vortices will affect on the flow that is being ingested by the NACA ram-air inlet.

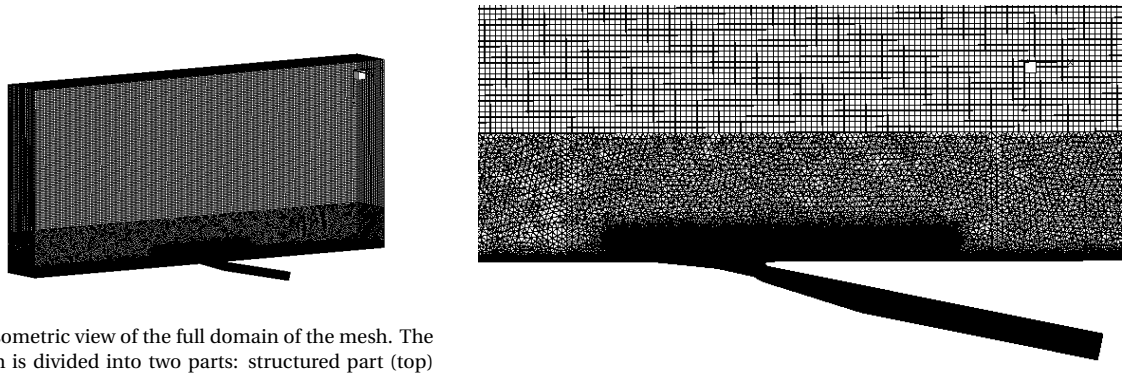

(a) Isometric view of the full domain of the mesh. The mesh is divided into two parts: structured part (top) and an unstructured part (bottom)

(b) Zoomed in on the NACA ram-air inlet

Figure 3.14: Mesh of the NACA ram-air inlet model that is used for the CFD simulations

The top part of the mesh shown in 3.14b contains a structured mesh. The choice of applying a structured mesh in this region is explained as follows. It is expected that the airflow far from the object of interest is undisturbed. Structured grids that are aligned with the flow leads to more accurate results. A structured mesh does not require a large computational memory of storing the irregular data structure since a structured mesh has easy mesh connectivity of the nodes and the elements. This leads to easy data management.

The mesh on the surface of the NACA ram-air lip is shown in Figure 3.15. A mapped mesh method was used to generate the mesh on the surface of the lip region since this is a critical region of the flow field. The number of divisions in the direction of the width of the inlet and the direction along the lip can be specified and controlled more easily for the grid independence study.

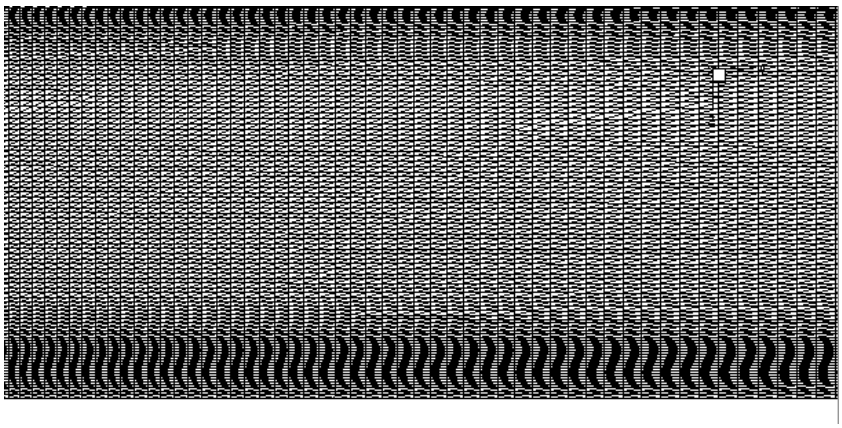

Figure 3.15: Mapped mesh around the lip area of the NACA ram-air inlet

The mesh adjacent to the walls, in the normal direction of the wall surface, required a special form of meshing. According to Versteeg and Malalasekera, the turbulent boundary layer is divided into two layers: the inner layer and the outer layer [34]. The inner layer is subdivided into three layers: the viscous sublayer that is close to the wall, the buffer layer and the low-law region. There are two methods to solve the near-wall region of a turbulent boundary layer [45]. The first method is to model the turbulence of the near-wall region to the grid wall. The modelling is done by empirical relations called wall functions. This method applies to high Reynolds number models such as the $k-\epsilon$ turbulence model. The second method is to resolve the turbulence up to the viscous sublayer near the grid wall. This applies to low Reynolds number models such as the $k-\omega$ and the $k-\omega$ SST turbulence models.

The inflation layer is a type of structured grid in which the first cell layer is located adjacent to a grid wall or a no-slip boundary. The height of each succeeding cell layer increases with a growth rate until the last cell layer of the inflation layer is generated. The entire inflation layer must be located in the viscous sublayer in order to predict the boundary layer accurately. An important aspect is that the first cell layer is located in the viscous sublayer. An important parameter to determine the first cell layer is the dimensionless wall distance y^+, also known as 'y plus' [46]. The y^+ is required to ensure that the first point of the grid is located in the viscous sublayer.

This is used in CFD in order to model the influence of the Reynold stress tensor near the domain walls, depending on the type of turbulence model. The $k-\omega$ SST turbulence model requires that the first layer height is estimated to have a $y+$ value of 1 for the first cell layer. The value $y+$ is defined in Equation 3.10 [34].

$$y^+ \equiv \frac{u_* y}{\nu} \tag{3.10}$$

Where u_{star} is the friction velocity $[m/s]$, y is the physical wall distance $[m]$, and ν is the kinematic viscosity $[m^2/s]$.

Equation 3.11 is defined as the friction velocity u_* [34].

$$u_* = \sqrt{\frac{\tau_w}{\rho}} \tag{3.11}$$

Where τ_w is the wall shear stress $[Pa]$, and ρ is the density of air at the wall $[kg/m^3]$.

Rearranging Equation 3.10 for first layer height y yields:

$$y \equiv \frac{y^+ \nu}{u_*} \tag{3.12}$$

The wall stress stress is calculated with Equation 3.13:

$$\tau_w = C_f \frac{1}{2} \rho U_\infty^2 \tag{3.13}$$

Where C_f is the local skin friction coefficient, ρ is the density of air at the wall $[kg/m^3]$, and U_∞ is the freestream velocity of the fluid medium $[m/s]$.

For a turbulent flow along a flat plate, the skin friction coefficient C_f can be estimated with Equation 3.14 [47].

$$C_f = \frac{0.027}{Re^{1/7}} \tag{3.14}$$

Where Re is the Reynolds number.

An inflation layer with the required first cell layer thickness that satisfied a $y+$ value of 1 was applied to the mesh of the fuselage wall and the physical walls of the NACA ram-air inlet. Figure 3.16 shows the mesh around the location at which the ambient air is ingested by the NACA ram-air inlet.

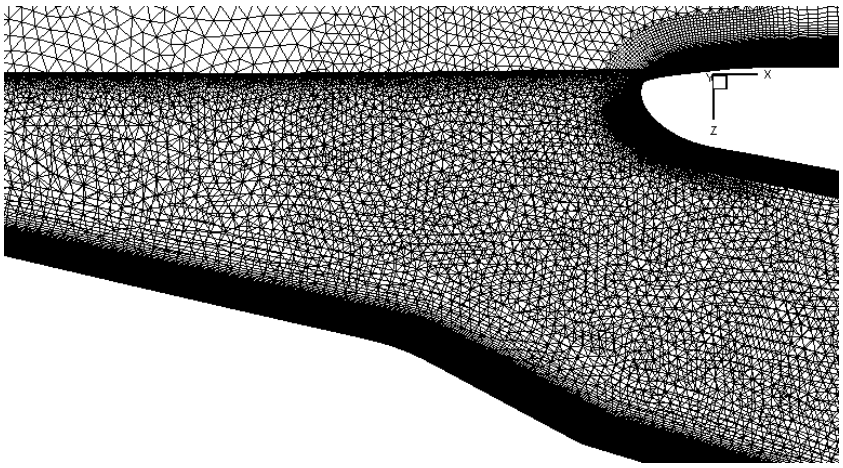

Figure 3.16: An inflation layer around the ramp, the lip and inside the tunnel is shown. The inflation layer is applied around all physical walls of the geometrical model.

The inflation layer around the lip can be seen on the right of Figure 3.16. The inflation cannot reach its full specific height at every location. A mode called Collision Avoidance is activated to detect regions of close proximity of the geometry that can lead to bad cells due to overlapping or crossing of the inflation layer. An example is the sharp edge of the NACA ram-air inlet at which the vortices are formed. Collision Avoidance is applied to this region since inflation layers cross at this location. Another example is the inflation layer located inside the NACA ram-air inlet. Although

a local refinement is applied near the throat of the inlet in Configuration 1, Collision Avoidance is brought into play to avoid geometrical limitations due to the application of the inflation layer leading to bad quality cells.

3.6. COMPUTATIONAL DOMAIN AND BOUNDARY CONDITIONS

This section explains the computational domain and the boundary condition types that were applied on the boundaries of the computational domain. The computational domain is explained in Subsection 3.6.1. The boundary conditions and the initial conditions are explained in Subsection 3.6.2.

3.6.1. COMPUTATIONAL DOMAIN

Figure 3.17 illustrates the computational domain of the NACA ram-air inlet submerged into a fuselage wall. The size of the computational domain is based on a wind tunnel experiment report NACA A8A20 and similar inlet CFD study on NACA ram-air inlet with vortex generators [17] [48]. The NACA ram-air inlet is placed at 6 times the characteristic length downstream of the inlet, whereas the outlet is placed 6 times downstream from the NACA ram-air inlet. The far-field, which is parallel with the fuselage wall, is placed at 5 times the characteristic length away from the fuselage wall. The other far-field that lies parallel with the symmetry plane is placed at 5 times the characteristic width distance away from the symmetry plane. The symmetry plane allows the computational domain to be halved reducing the computational cost. The dimensions of the computational domain are depicted with arrows and the responding domain length in Figure 3.17. The symmetry is located along the cutting plane of the NACA ram-air inlet, but it is not illustrated with colour in Figure 3.17. Note that the NACA ram-air inlet is not shown in Figure 3.17.

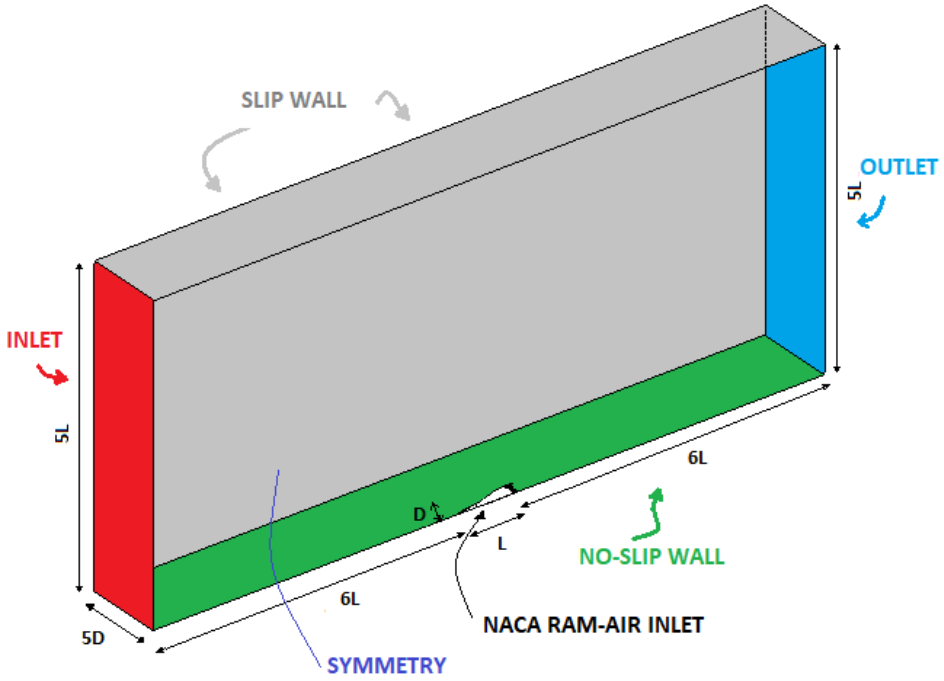

Figure 3.17: Computational domain with its boundary conditions - NACA ram-air inlet (tunnel) is hidden

Figure 3.18 shows a close-up of the computational domain of the NACA ram-air inlet that was not shown in Figure 3.17. The duct is extended by three times the characteristic length of the NACA ram-air inlet to allow the flow to be fully developed without the effect of the imposed boundary

condition located at the back of the duct tunnel. The duct exit is represented with an orange colour. The physical walls of the NACA ram-air inlet tunnel, which are wetted by the airflow, are displayed in green. A no-slip wall has been imposed on these walls. The plane that represents the symmetry plane is not shown with a colour.

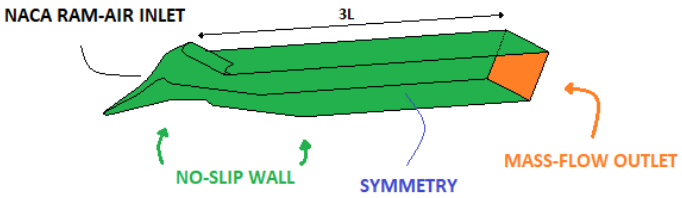

Figure 3.18: Computational domain with its boundary conditions - zoomed in on the NACA ram-air inlet

3.6.2. BOUNDARY CONDITIONS AND OPERATING CONDITIONS

Without the information of the flow field at the boundary conditions, the CFD simulation and its surroundings are not defined yet. Boundary conditions are very important to prescribe the psychical representation of the fluid flow. Therefore, appropriate boundary conditions need to be applied to the boundaries of the computational domain. Operation conditions at the boundary conditions are required to define the input values of the steady-state RANS simulations.

The locations of each boundary condition are illustrated in Figures 3.17 and 3.18. The boundary conditions that were used for the CFD problem are described as follows.

Pressure inlet - A pressure inlet was used on the boundary upstream of the NACA ram-air inlet. The inflow direction is parallel along the fuselage since the angle of attack was chosen to be zero. For this boundary condition, the gauge pressure (relative pressure to the operating pressure) and the total temperature were required as input. The flow properties were obtained with isentropic flow relations. For a Mach number of 0.20 and altitude of 0 $[m]$, the isentropic relations were used to calculated the total and static pressure. The freestream total and static pressure were calculated to be 104190 and 101325 $[Pa]$, respectively. In ANSYS Fluent, the gauge was required as an input parameter. The gauge pressure was obtained by subtracting the value of the freestream static pressure from the freestream total pressure. The freestream total and static temperature were calculated to equal to 290.46 and 288.15 $[K]$, respectively. The turbulence was specified by the turbulent intensity and the turbulent length scale. The turbulent intensity was calculated to be 2.46% using Equation 2.20. The turbulent length scale makes it easier to estimate and more intuitive to link the physical size of the large eddies to the physical size of the problem. The length of the NACA ram-air inlet, parallel with the direction of the fuselage skin, was used as the reference length. By using Equation 2.19, the turbulent length scale was calculated to be 0.0485 $[m]$.

Pressure outlet - A pressure outlet was applied to the outlet boundary of the computational domain. The pressure outlet is required to be placed far from the body of interest, such that the static pressure has reached its freestream conditions. Furthermore, it should not be placed in regions with large geometrical changes. By placing the pressure-outlet sufficiently far from the body of interest convergence problems can be minimised. The gauge static pressure was equal to 0 since the operating pressure was set equal to the static pressure.

No-slip condition - This boundary condition was imposed on any real physical wall, such as the walls of the NACA ram-air inlet, fuselage surface, NACA ram-air lip, the closure flap mechanism and the walls of the duct. This boundary condition assumes that the velocity of the fluid adjacent to the solid walls is zero, meaning that the fluid comes to a rest forming a boundary layer [34].

Slip condition - Free-slip walls were applied to the boundaries away from the NACA ram-air inlet and fuselage (indicated as far-field) by specifying the zero shear force equal to zero allowing the flow to match with the freestream velocity. The normal component of velocity has a value of zero, whilst the gradient of the tangential component is equal to zero.

Mass-flow-outlet - A mass flow outlet was applied to the boundary condition at the end of the NACA ram-air tunnel. Since the pressure at the exit of the NACA ram-air tunnel is unknown, a pressure outlet cannot be used. Therefore, a mass-flow-outlet was used for this boundary. This provides the ability to specify and vary the mass flow rate. For this thesis, the mass flow rate is an important parameter as it specifies the amount of air that is being ingested by the NACA-ram-air inlet and the required amount of air for the heat exchangers to cool bleed-air. The target mass flow rate was specified in such a way that the choked condition was avoided.

Symmetry - The NACA ram-air inlet is symmetric along its x-axis, acting as a centreline of the body. Due to the symmetry plane, the geometry of the real representation can be reduced by half meaning that the computational domain reduced by half in size. This has the benefit of decreasing the computational cost. At the symmetry plane, it is required that the normal component of velocity is zero and the normal gradients for all variables are zero [35]. Note that the mass flow rate imposed at these boundaries are only half of the actual mass flow rate. No variables are required to be submitted for a symmetry condition.

The operating conditions are summarised in Table 3.3.

Table 3.3: The operating conditions

Variable	Symbol	Value	Unit
Mach Number	M	0.20	–
Velocity	v	68.06	m/s
Altitude	h	0	m
Static Temperature	T_s	288.15	K
Static Pressure	P_s	101325	Pa
Air Density	ρ	1.225	kg/m^3

4

GRID CONVERGENCE INDEX

In this chapter, the main components of the numerical error are explained in Section 4.1. This will be followed by the special version of the Grid Convergence Index (GCI) together with the calculations explained in Section 4.2. The GCI method was applied to Configurations 1, 2, and 3.

4.1. NUMERICAL ERROR

According to Eça and Hoekstra, the numerical error of a CFD solution consists of three components: the round-off error, the iterative error and the discretisation error [49]. Each source of discretisation will be explained in Subsections 4.1.1, 4.1.2, and 4.1.3, respectively.

4.1.1. ROUND-OFF ERROR

The round-off error is originated from the finite representation of a number by a computer [32]. The exact values of the variables are truncated due to the finite number of digits that are used by a computer. This is a machine-limiting factor. For the CFD simulations, double precision has been chosen. Double precision is considered to be adequate to make sure that the round-off error is sufficiently small compared to the other two sources of the numerical error [49]. However, round-off errors are usually not the dominant source of numerical error.

4.1.2. ITERATIVE ERROR

The iterative error is due to the difference of the iterative solution of a set of algebraic equations and the fully converged solution of the same system. [32]. This requires iterative methods to solve and refine the approximate solution until it is of sufficient accuracy. To ensure that the iterative error is insignificant, the residual errors are used to monitor the numerical process and should be 2 to 3 orders of magnitude smaller than the discretisation error [4]. In this thesis, the convergence of the residuals with respect to the number of iterations has been checked. The residuals quantify the error, often named as imbalance, of mass, momentum and energy in the solution of the control volume. The residuals shall be as low as possible to be more numerically accurate. In Fluent, a solution is considered to be converged when the scaled residuals are below a tolerance value of at least 10^{-3} to stipulate at least qualitative convergence [31] [32]. For quantitative convergence, the changes in flow variables are required to be monitored. In the thesis, the drag of the tunnel and the fuselage, and the total pressure at the throat section were monitored.

4.1.3. DISCRETISATION ERROR

The discretisation error is the primary source of the numerical error in CFD simulations [49]. This type of error is due to the discretisation of the equations of fluid mechanics into a set of algebraic equations [49]. The exact solution of the continuum equations is numerically approximated. The discretisation error is affected by the number of grid cells and the distribution of grid points in regions with a high variation of flow quantities. The approximation approaches close to the exact solution of the discretised equations as the number of cells in the computational domain is increased. However, a high number of cells is computationally more costly, since it requires longer run time and more CPU to run the CFD simulations. In the next Section, the GCI which was used to assess the discretisation error will be presented. Furthermore, this is followed by a trade-off of the grids based on the run time and the overall uncertainty of the CFD simulations.

4.2. LEAST SQUARES VERSION OF GRID CONVERGENCE INDEX

In order to assess the discretisation error of the CFD simulations the Least Squares version of the Grid Convergence Index (GCI) has been used [4]. In Subsection 4.2.1, the strategy to refine the meshes for the grid convergence will be explained. In Subsection 4.2.2, the calculation of the discretisation uncertainty will be presented. Finally, the GCI method was applied to the three configurations of the NACA ram-air inlet with different opening sizes and its results are presented in Subsections 4.2.3, 4.2.4 and 4.2.5. The trade-off between the run time and the GCI is discussed in Subsection 4.2.6.

4.2.1. MESH REFINEMENT

In order to assess the discretisation error by comparing a set of solutions, a set of grids was required to be generated and simulated in CFD. First of all, a mesh that is considered to have a *fine* refinement needs to be generated, then the other meshes were generated. It is important to make sure that local refinement was done at regions of high flow gradients. A *very fine* mesh was generated and three meshes that contain larger cell sizes. Those are labelled as the *medium*, *coarse* and *very coarse* meshes. The refinement was performed according to the following guidelines.

The refinement was done on a three-dimensional mesh. For practical reason, the refinement ratio was chosen to be 1.26 such that the total number of cells will approximately be doubled ($1.26^3 \approx 2$) or halved. Therefore, the setting for the cell size was multiplied or divided by 1.26 for a coarser or finer mesh, respectively. The setting for the number of divisions on an edge was multiplied or divided by 1.26 to keep the same level of refinement. For the body of influence, the cell size was submitted. This value was also multiplied or divided by 1.26 for a coarser or finer mesh, respectively.

The inflation layer, which is intended to capture the flow gradient inside the boundary layer needs to be refined as well. For an inflation layer, the number of layers needs to be specified. This number was also multiplied or divided by 1.26 and rounded-off for a coarser or finer mesh, respectively. The first layer thickness was calculated in order to obtain the required y^+ value of 1 for the $SST\, k-\omega$ model. This value shall be kept constant to maintain y^+ around 1, therefore the growth of the inflation needs to be adjusted in order to keep the same inflation layer thickness.

Figure 4.1a illustrates the very coarse mesh, whereas Figure 4.1b illustrates the very fine mesh of the mesh refinement study. The grids are numbered from 1 to 5 according to their level of refinement: no.1 for the very fine grid, no.2 for the fine grid, no.3 for the medium grid, no.4 for the coarse grid, and no.5 for the very coarse grid.

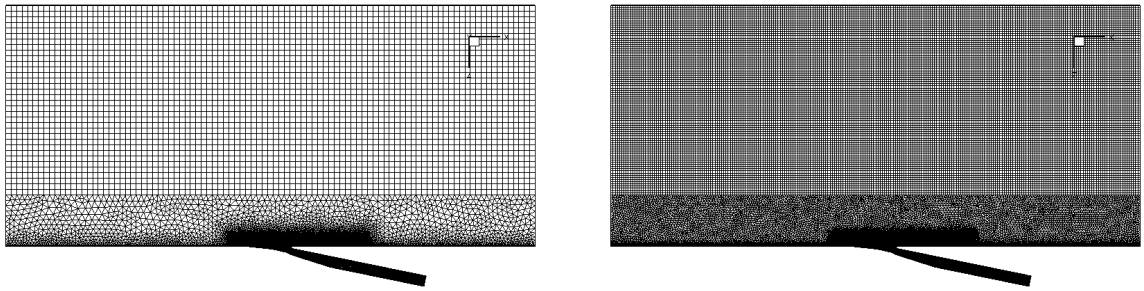

(a) Very coarse grid (Mesh no.5)

(b) Very fine grid (Mesh no.1)

Figure 4.1: The mesh of the mesh refinement study with a refinement ratio of 1.26

4.2.2. DISCRETISATION UNCERTAINTY

The estimation of the discretisation uncertainty U of a flow quantity of the standard Grid Convergence Index is calculated by Equation 4.1 [4].

$$U = F_s |\delta_{RE}| \tag{4.1}$$

Where Fs is a safety factor of 1.25 for the comparison with two grids or more, and δ_{RE} is the estimation of the error.

The error estimation can be obtained from Richardson's extrapolation, given in Equation 4.2 [4].

$$\delta_{RE} = \phi_i - \phi_0 = \alpha h_i^p \tag{4.2}$$

Where ϕ is the value of a flow variable, h_i is the representative grid cell size and p is the observed order of convergence.

Since the number of grids that were simulated for each configuration is 5, Richardson's extrapolation was obtained with a least squares approach that includes the flow values of all five grids. In order to calculate the exact value ϕ_0 that would be obtained in theory from a mesh with an infinite number of cell elements, the following minimisation function needs to be solved, shown in Equation 4.3 [4].

$$S(\phi, \alpha, p) = \sqrt{\sum_{i=1}^{n_g} \left(\phi_0 - (\phi_0 + \alpha h_i^p)\right)^2} \tag{4.3}$$

Where n_g is the number of grids, ϕ is the value of a flow variable, α is a constant, p is the observed order of convergence and h_i is the representative grid cell size. The grid refinement ratio h_i / h_1 is the ratio of the average cell height of the given mesh and the average cell height of the finest mesh, calculated using the number of cells of the grid n_{cells_i}. This relation is shown in Equation 4.4 [4].

$$\frac{h_i}{h_1} = \left(\frac{n_{cells_i}}{n_{cells_1}}\right)^{-\frac{1}{3}} \tag{4.4}$$

The minimisation function was solved by MATLAB using fmincon to find the values of the constant α and the observed order of convergence p [50].

After the values of α, ϕ, and p were determined to solve the minimisation function in Equation 4.3, the standard deviation was calculated. The standard deviation U_s of each data fit was calculated using Equation 4.5 [4].

$$U_s = \sqrt{\frac{\sum_{i=1}^{n_g} \left(\phi_i - (\phi_0 + \alpha h_i^p)\right)^2}{n_g - 3}} \tag{4.5}$$

The overall uncertainty U_ϕ that depends on its order of convergence p can be calculated using Equation 4.6 [4].

$$\begin{aligned} U_\phi &= 1.25\,\delta_{RE} + U_s \\ &\qquad \text{for } 0.95 \leq p < 2.05 \\ U_\phi &= \max(1.25\,\delta_{RE^*} + U_s, 1.25\,\Delta_M) \\ &\qquad \text{for } p \geq 2.05 \end{aligned} \tag{4.6}$$

Where Δ_M is the maximum absolute difference between all solutions.

The error estimation from Richardson's extrapolation δ_{RE} is obtained relative to the value obtained with the fine mesh from Mesh no.2, denoted with subscript 2. The standard deviation U_s, the error estimation of Mesh no.2 with respect to the estimated exact value δ_{RE2}, the order of convergence p of the best fit, and the theoretical fit with an order of convergence $p^* = 2$ are presented in the following Subsections 4.2.3, 4.2.4, and 4.2.5 for Configurations 1, 2 and 3, respectively.

The pressure coefficient around the NACA ram-air lip of each configuration was checked on its grid convergence. ϕ is defined as the normalised width of the NACA ram-air lip. The slice with a value of $\phi = 0.0$ is located at the symmetry plane of the geometry, whereas $\phi = 0.5$ is halfway along the width of the NACA ram-air lip. The pressure plots at the locations $\phi = 0, 0.25, 0.50$ have been assessed. The results were obtained for three grids: the very fine (Mesh no.1), the fine (Mesh no.2) and very coarse grid (Mesh no.5). The locations of the slices are displayed in Figure 4.2.

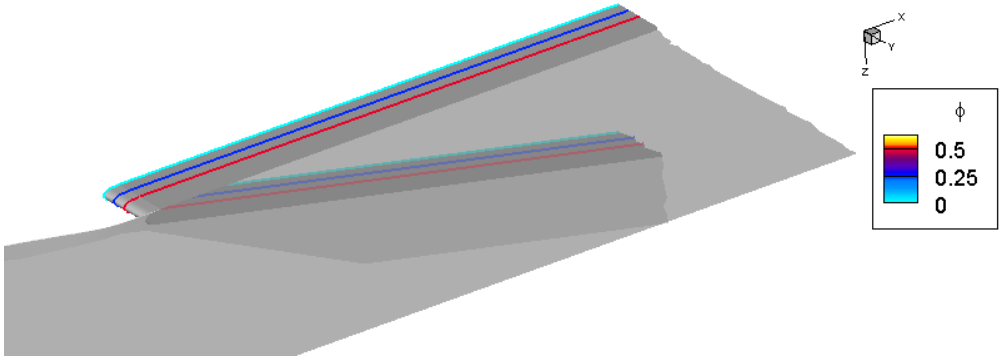

Figure 4.2: The three locations of the slices, at which the pressure coefficient C_p has been plotted, are indicated with ϕ.

4.2.3. GCI OF CONFIGURATION 1 - 15 [mm] OPENING

Table 4.1 presents the drag coefficient C_D and the pressure recovery η for each of the 5 grids and the exact approximation of both two parameters denoted by Mesh no.0. The estimated value of Mesh no.0 is calculated for two different fits. The observed order of convergence p, its exact value ϕ_0 and its best fit are calculated using the quantities from the five different meshes whereas the exact value ϕ_0 of the fit with the theoretical order of convergence p^* is kept constant at 2 since the second-order discretisation scheme was used.

Table 4.1: Grid Convergence Study of Configuration 1 - 15 [mm] opening - the drag coefficient and the pressure recovery of each mesh. The values of both parameters are extrapolated with the best fit and the fit where the order of convergence was set to 2.

Mesh	Refinement	Number of elements [$x10^6$]	h_i/h_1	C_D [-]	η [-]
5	very coarse	2.530	2.21	0.0009382	0.6023
4	coarse	4.223	1.87	0.0009445	0.6034
3	medium	7.911	1.51	0.0009758	0.6062
2	fine	14.699	1.23	0.0009795	0.6163
1	very fine	27.423	1.00	0.0009843	0.6167
0 (best fit)	-	infinite	0	0.0009929	0.6172
0 (fit with $p^* = 2$)	-	infinite	0	0.0099251	0.6173

Table 4.2 shows the results of the uncertainty analysis for Configuration 1. The observed order of convergence p, the standard deviation U_s of the fit, the error relative to Mesh no.2 δ_{RE2} are presented in the top part of the table. The standard deviation U_s^* and the error relative to Mesh no.2 δ^*_{RE2} of the fit with an order of convergence of $p^* = 2$ and the overall discretisation uncertainty U^*_ϕ are presented in the bottom part of the Table.

Table 4.2: Grid Convergence Study of Configuration 1 - 15 [mm] opening - uncertainty analysis

Quantity	Drag coefficient C_D	Pressure recovery η
p	2.598	2.202
U_s [%]	0.721	0.370
δ_{RE2} [%]	-1.086	-0.095
p^*	2	2
U_s^* [%]	0.808	0.396
δ^*_{RE2} [%]	-1.320	-0.103
Overall uncertainty U^*_ϕ [%]	2.4613	0.5311

Figures 4.3a and 4.3b show the Grid Convergence Index of the parameters: the drag coefficient C_D as a function of the relative cell size and the pressure recovery η at the throat section of the NACA ram-air inlet as a function of the relative cell size. These two parameters C_D and η of each mesh were compared with respect to the value obtained from Mesh no.2. Furthermore, the best fit of the mesh data point and the best fit for the theoretical order of convergence $p^* = 2$ are illustrated in the plot as well.

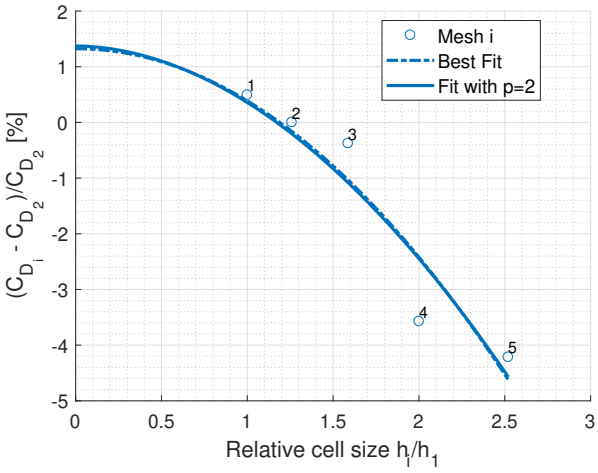

(a) GCI of the drag coefficient C_D with respect to the relative cell size. The relative error to the value obtained from Mesh no.2 is presented.

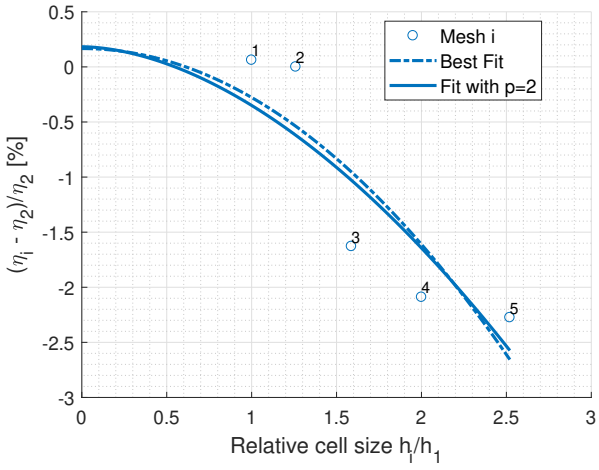

(b) GCI of the pressure recovery η with respect to the relative cell size. The relative error to the value obtained from Mesh no.2 is presented.

Figure 4.3: Grid convergence study of case 15 [mm]. The mesh data points are illustrated with a circle icon, the dotted line represents the best fit of the observed order of convergence and the solid line corresponds to the fit with $p^* = 2$.

Both the drag coefficient C_D and the pressure recovery η are assessed on its grid independence. It can be seen in Figures 4.3a and 4.3b that the relative differences of the drag coefficient and the pressure recovery are scattered. The highest relative difference with respect to the value of Mesh no.2 can be found in the drag coefficient C_D. Therefore, from Table 4.2 the overall uncertainty of the drag coefficient C_D with 2.46% was also the highest of the two values of overall uncertainty. Although this number seems to be high, looking at the differences in Figure 4.3a the relative differences of the drag coefficient C_D of Meshes no.1,2 and 3 show variations of less than 1%, whereas the relative differences of the drag coefficient of Meshes no.4 and no.5 with respect to Mesh no.2 are around 4%. These outliers contribute to a higher overall uncertainty. The pressure recovery η shows good agreement between the finest grids, Meshes no.1 and no.2. This is represented by the low overall uncertainty of 0.53%. The pressure recovery η of Mesh no.1 has a relative difference of less than 0.5%, whereas the relative differences of Mesh no.3-5 deviate around 1.5-2.5% with respect to Mesh no.2.

The grid convergence of the chordwise distribution of the pressure coefficient C_p of Configuration 1 is shown in Figures 4.4, 4.5, and 4.6. The C_p distributions are shown for locations $\phi = 0, 0.25, 0.5$ along the width of the NACA ram-air lip, as shown in 4.2.

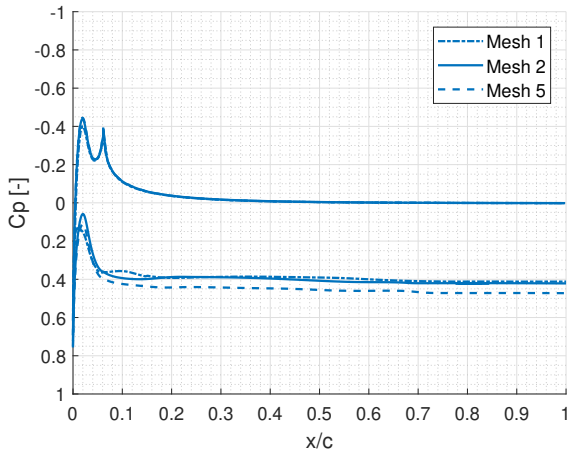

Figure 4.4: Grid convergence study of the chordwise pressure coefficient distribution of the upper-and lower surfaces at $\phi = 0$. The results of three grid sizes of Configuration 1 are illustrated.

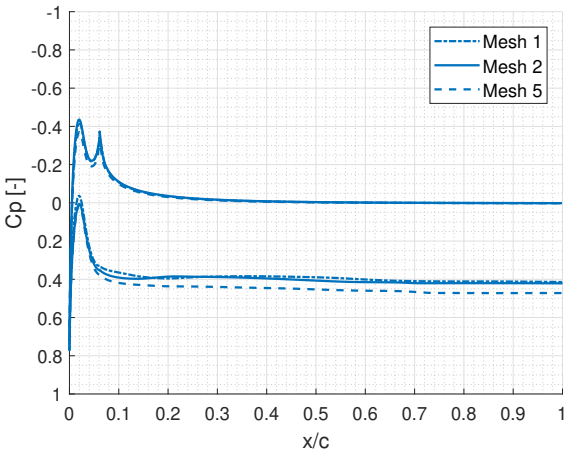

Figure 4.5: Grid convergence study of the chordwise pressure coefficient distribution of the upper-and lower surfaces at $\phi = 0.25$. The results of three grid sizes of Configuration 1 are illustrated.

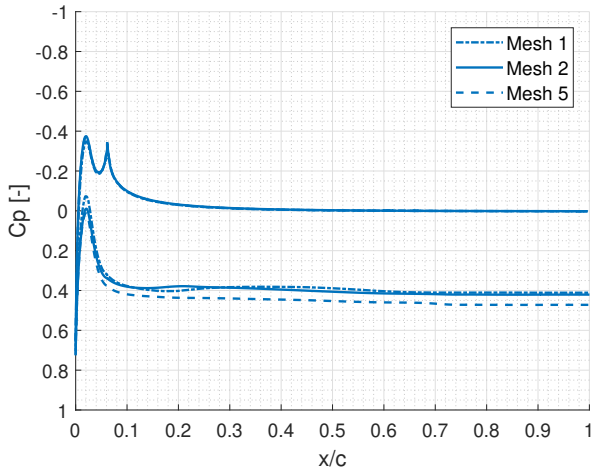

Figure 4.6: Grid convergence study of the chordwise pressure coefficient distribution of the upper-and lower surfaces at $\phi = 0.50$. The results of three grid sizes of Configuration 1 are illustrated.

In Figure 4.4 it can be seen that the C_p-plots of Mesh no.1 and no.2 are very similar at the top surface. The C_p-plot of the upper surface in Figure 4.4 shows very small differences. An exception for the lower surface is noticeable with a small 'bump' around $x/c = 0.1$. The difference is found at the region where the lip changes to the flat surface of the fuselage. This can cause a higher discretisation error at this location. The same difference can be noticed from Figures 4.5 and 4.6 as well. In those three figures, it can be seen that Mesh no.5 possesses a significant difference at the lower surface. The grid size of Mesh no.5 is much larger than Mesh no.1 and no.2, causing a larger discretisation error.

4.2.4. GCI OF CONFIGURATION 2 - 55 [mm] OPENING

Table 4.3 shows the exact values of the drag coefficient C_D and the pressure recovery η for multiple meshes of Configuration 2 where the throat in the NACA ram-air tunnel is equal to 55 [mm]. The estimated value of Mesh no.0 is calculated for both the observed order of convergence p and the constant value of $p^* = 2$.

Table 4.3: Grid Convergence Study of Configuration 2 - 55 [mm] opening - the drag coefficient and the pressure recovery of each mesh. The values of both parameters are extrapolated with the best fit and the fit where the order of convergence was set to 2.

Mesh	Refinement	Number of elements [$x10^6$]	h_i/h_1	C_D [-]	η [-]
5	very coarse	2.081	2.37	0.0009396	0.5424
4	coarse	3.846	1.93	0.0009682	0.5325
3	medium	7.283	1.56	0.0009416	0.5333
2	fine	13.465	1.27	0.0009680	0.5342
1	very fine	27.533	1.00	0.0009715	0.5328
0 (best fit)	-	infinite	0	0.0009724	0.5325
0 (fit with $p^* = 2$)	-	infinite	0	0.0009775	0.5303

Table 4.4 shows the uncertainty analysis of Configuration 2. The observed order of convergence p, the standard deviation U_s of the fit, the error relative to Mesh no.2 δ_{RE2} are presented in the top part of the table. The standard deviation U_s^* and the error relative to Mesh no.2 δ^*_{RE2} of the fit with an order of convergence of $p^* = 2$ and the overall discretisation uncertainty U^*_ϕ are presented in the bottom part of the Table.

Table 4.4: Grid Convergence Study of Configuration 2 - 55 [mm] opening - uncertainty analysis

Quantity	Drag coefficient C_D	Pressure recovery η
p	6.7246	7.8913
U_s [%]	0.5042	8.0600
δ_{RE2} [%]	-0.4584	0.1526
p^*	2	2
U_s^* [%]	0.7459	0.2900
δ_{RE2} [%]	-0.9769	0.3972
Overall uncertainty U^*_ϕ [%]	1.7253	0.6378

Figures 4.7a and 4.7b show the Grid Convergence Study of Configuration 2. Both the drag coefficient C_D and the pressure recovery η are analysed on its grid independence.

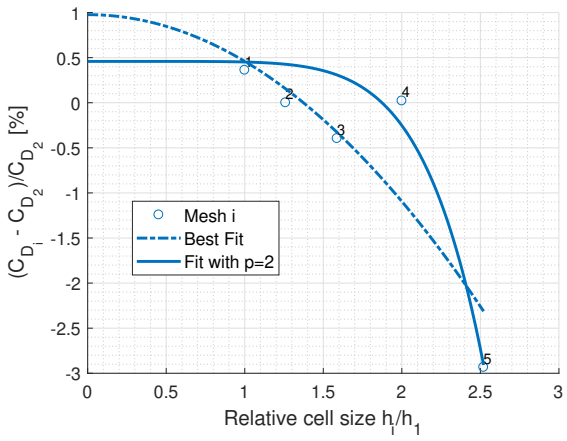

(a) GCI of the drag coefficient C_D with respect to the relative cell size. The relative error to the value obtained from Mesh no.2 is presented.

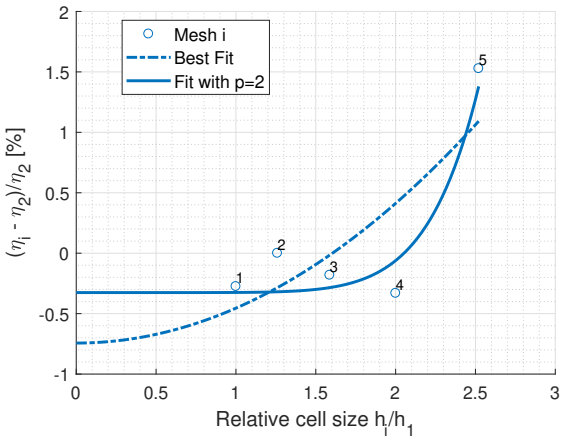

(b) GCI of the pressure recovery η with respect to the relative cell size. The relative error to the value obtained from Mesh no.2 is presented.

Figure 4.7: Grid convergence study of Configuration 2 - 55 $[mm]$. The mesh data points are illustrated with a circle icon, the dotted line represents the best fit of the observed order of convergence and the solid line corresponds to the fit with $p^* = 2$.

From the observation of Figure 4.7a, it can be seen that Meshes no.1-4 show small differences in the drag coefficient C_D. The differences of the drag coefficient C_D for those four meshes are around 0.5%, whereas the difference of the drag coefficient of Mesh no.5 with respect to Mesh no.2 is relatively large to be 3%. This is also represented by the overall uncertainty of 1.73% for the drag coefficient in Table 4.4. In Figure 4.7b, the differences of the pressure recovery η of Meshes no.1-4 of Configuration 2 are very small with differences of less than 0.5%, while Mesh no.5 shows a relative difference of 1.5% with respect to Mesh no.2. The small differences in pressure recovery of Configuration 2 led to a low overall uncertainty of 0.64%.

The grid convergence of the chordwise distribution of the pressure coefficient C_p of Configuration 2 is shown in Figures 4.8, 4.9, and 4.10. The C_p distributions are shown for locations $\phi = 0, 0.25, 0.5$ along the width of the NACA ram-air lip, as shown in Figure 4.2.

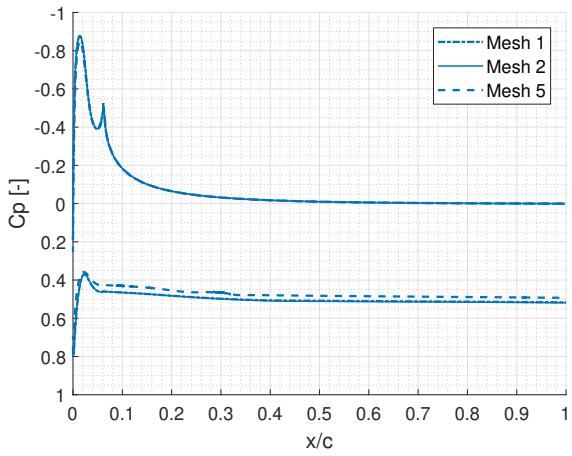

Figure 4.8: Grid convergence study of the chordwise pressure coefficient distribution of the upper-and lower surfaces at $\phi = 0$. The results of three grid sizes of Configuration 2 are illustrated.

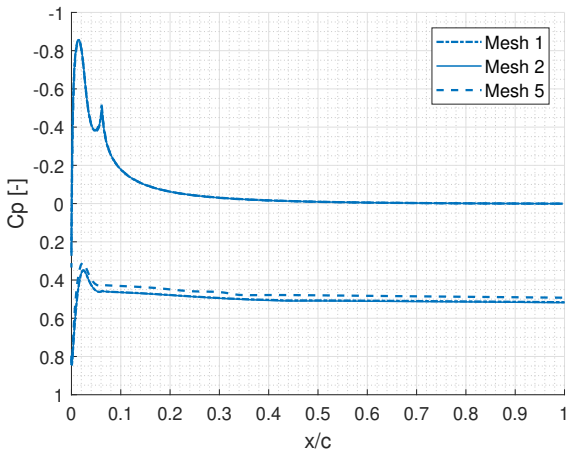

Figure 4.9: Grid convergence study of the chordwise pressure coefficient distribution of the upper-and lower surfaces at $\phi = 0.25$. The results of three grid sizes of Configuration 2 are illustrated.

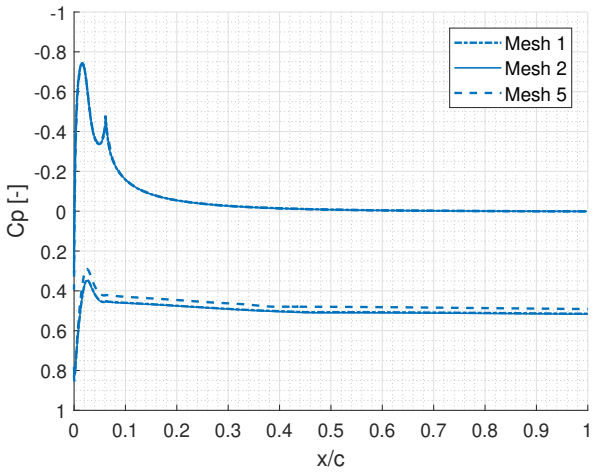

Figure 4.10: Grid convergence study of the chordwise pressure coefficient distribution of the upper-and lower surfaces at $\phi = 0.50$. The results of three grid sizes of Configuration 2 are illustrated.

It can be seen that the C_p-plots of the upper surface in Figures 4.8, 4.9, and 4.10, are very similar for Mesh no.1 and no.2. However, a small variation can be found at the suction peak. The element size at the lip can have an influence on the discretisation error, leading to local differences in the C_p distribution. The lower surface of Figures 4.8, 4.9, and 4.10 also shows great similarity for the meshes with finest grids meshes no.1 and no.2, but the lower surface of Mesh no.5 shows an offset with Meshes no.1 and 2. This can be explained by the coarser grid of Mesh no.5.

4.2.5. GCI OF CONFIGURATION 3 - 95 [mm] OPENING

Table 4.5 shows the exact values of the drag coefficient C_D and the pressure recovery η for multiple meshes of Configuration 3 where the opening in the NACA ram-air tunnel is equal to 95 [mm]. The estimated value of Mesh no.0 is calculated for both the observed order of convergence p and the constant value of $p^* = 2$.

Table 4.5: Grid Convergence Study of Configuration 3 - 95 [mm] opening - the drag coefficient and the pressure recovery of each mesh. The values of both parameters are extrapolated with the best fit and the fit where the order of convergence was set to 2.

Mesh	Refinement	Number of elements [$x10^6$]	h_i/h_1	C_D [-]	η [-]
5	very coarse	2.081	2.19	0.0028928	0.7788
4	coarse	3.364	1.86	0.0029417	0.7824
3	medium	6.311	1.51	0.0029638	0.7820
2	fine	11.682	1.23	0.0029799	0.7823
1	very fine	21.807	1.00	0.0029891	0.7826
0 (best fit)	-	infinite	0	0.0030018	0.7826
0 (fit with $p^* = 2$)	-	infinite	0	0.0030048	0.7829

Table 4.6 shows the uncertainty analysis of Configuration 3. The observed order of convergence p, the standard deviation U_s of the fit, the error relative to Mesh no.2 δ_{RE2} are presented in the top part of the table. The standard deviation U_s^* and the error relative to Mesh no.2 δ^*_{RE2} of the fit with an order of convergence of $p^* = 2$ and the overall discretisation uncertainty U^*_ϕ are presented in the bottom part of the Table.

Table 4.6: Grid Convergence Study of Configuration 3 - 95 [mm] opening - uncertainty analysis

Quantity	Drag coefficient C_D	Pressure recovery η
p	3.2881	8.9127
U_s [%]	0.1176	0.0519
δ_{RE2} [%]	-0.5800	-0.0321
p^*	2	2
U_s^* [%]	0.1370	0.0808
δ_{RE2}^* [%]	-0.8342	-0.0757
Overall uncertainty U_ϕ^* [%]	1.1072	0.1412

Figures 4.11a and 4.11b show the Grid Convergence Study of Configuration 3. The drag coefficient C_D and the pressure recovery η are assessed on its grid independence.

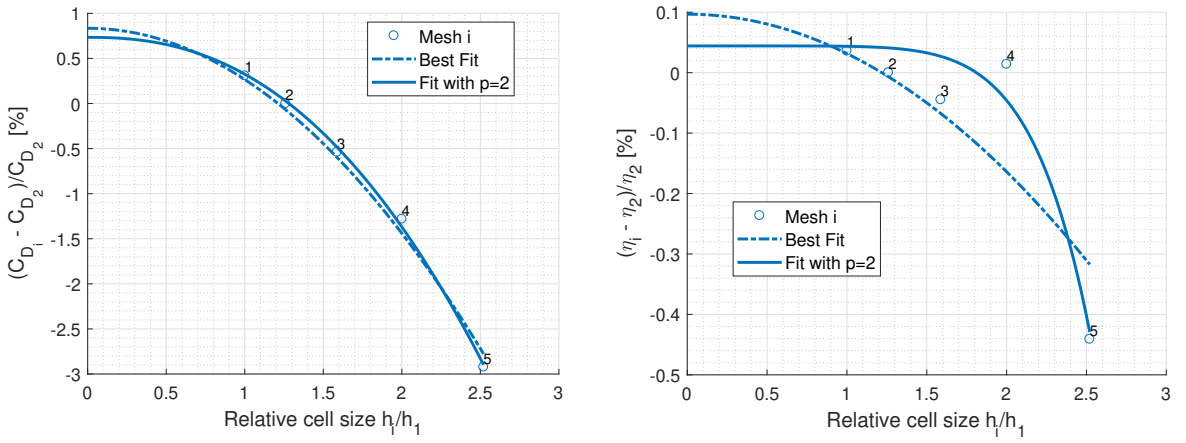

(a) GCI of the drag coefficient C_D with respect to the relative cell size. The relative error to the value obtained from Mesh no.2 is presented.

(b) GCI of the pressure recovery η with respect to the relative cell size. The relative error to the value obtained from Mesh no.2 is presented.

Figure 4.11: Grid convergence study of case 95 [mm]. The mesh data points are illustrated with a circle icon, the dotted line represents the best fit of the observed order of convergence and the solid line corresponds to the fit with $p^* = 2$.

Note that the y-axis in Figure 4.11b varies from -0.5% to 0.1%. The relative differences of the pressure recovery η with respect to Mesh no.2 are very small, especially for Meshes no.1,2, and 4. This resulted in a low overall uncertainty of the pressure recovery of the Grid Convergence Study of Configuration 3 of 0.14%, shown in Table 4.6.

The grid convergence of the chordwise distribution of the pressure coefficient C_p of Configuration 3 is shown in Figures 4.12, 4.13, and 4.14. The C_p distributions are shown for locations $\phi = 0, 0.25, 0.5$ along the width of the NACA ram-air lip, as shown in Figure 4.2.

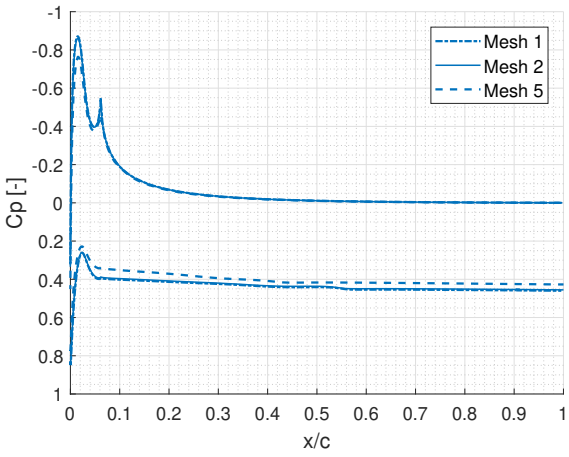

Figure 4.12: Grid convergence study of the chordwise pressure coefficient distribution of the upper-and lower surfaces at $\phi = 0$. The results of three grid sizes of Configuration 3 are illustrated.

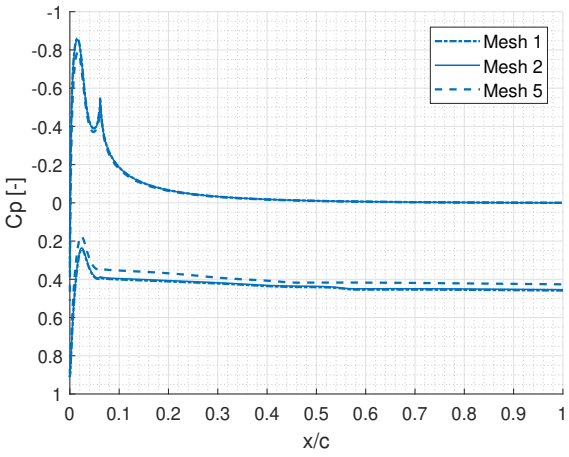

Figure 4.13: Grid convergence study of the chordwise pressure coefficient distribution of the upper-and lower surfaces at $\phi = 0.25$. The results of three grid sizes of Configuration 3 are illustrated.

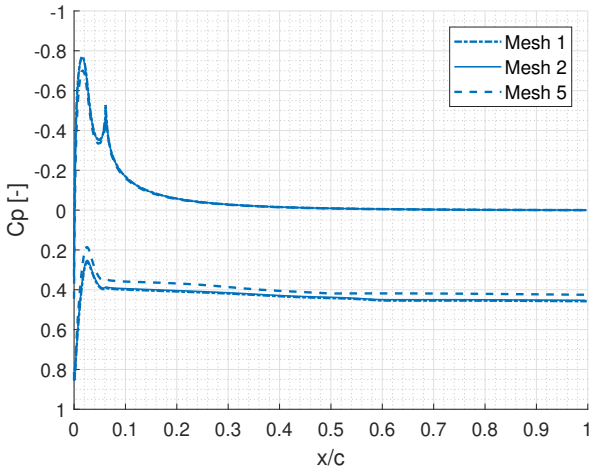

Figure 4.14: Grid convergence study of the chordwise pressure coefficient distribution of the upper-and lower surfaces at $\phi = 0.50$. The results of three grid sizes of Configuration 3 are illustrated.

These three figures show that the overall agreement between the C_p-plots of the top surface is generally good, although the suction peak at Mesh no.2 tends to be slightly overestimated. Despite Mesh no.5, the coarsest grid, the lower surface of the three meshes in Figures 4.12, 4.13, and 4.14 show good agreement. In the three figures, the C_p-plots of the lower surface of Mesh no.5 tend to shift upwards.

4.2.6. RUN TIME OF CFD SIMULATIONS

The numerical error due to the spatial discretisation depends on the level of mesh refinement. Mesh no.1 (very fine mesh) amongst the set of five meshes is expected to be the best in terms of accuracy, but the high number of the mesh elements leads to high computational cost for the CFD simulation. From the Grid Convergence Index assessment previously treated, a trade-off between the required run time and the level of accuracy was made.

Figure 4.15 shows the run time as a function of the number of grid cells. The run time of each set (of five grids) of Configurations 1, 2, and 3, are plotted.

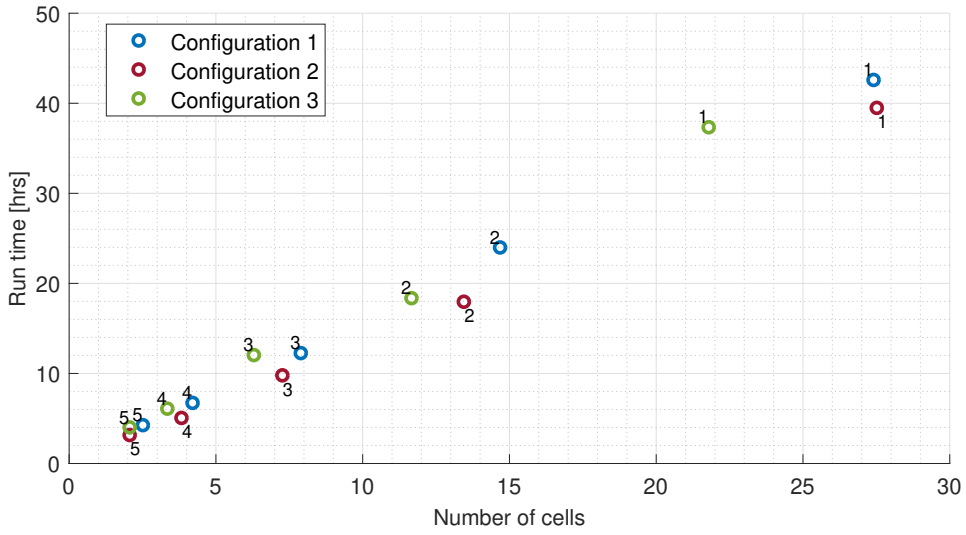

Figure 4.15: The CFD run time of Meshes no.1 to 5, for configurations 1,2, and 3, are indicated with blue, red, and green respectively.

In Figure 4.15, the number next to the data point represents the level of refinement of the grid, numbered from 1 to 5 with no.1 as the very fine grid. It can be noticed that five clusters of data points can be distinguished. Each cluster is represented by the level of refinement. On the right in Figure 4.15, it can be seen that the very fine grids Mesh no.1 of the three Configurations, which contains most cells, are located on the right. Note that the data point in green, which represents Configuration 3, contains the fewest number of cells compared to other configurations at a similar level of refinement. Configurations 1 and 2 with an opening of 15 and 55 $[mm]$, respectively, required local refinements at regions with high flow gradients due to their more narrow opening compared with Configuration 3 with an opening of 95 $[mm]$. The local refinements have led to an increase in the total amount of cells in the grid.

Mesh no.1 of all configurations has a run time of around 40 hours, which was very costly due to the limited time of the thesis project. A couple of weeks is required to successfully run for 50 cases of CFD simulations. Mesh no.2 has a run time of around 20 hours with a high level of accuracy. Based on the Grid Convergence Index and run time study, Mesh no.2 was chosen as the final grid that was used for the CFD simulations.

5

RESULTS AND DISCUSSION

The aerodynamic analysis on the NACA ram-air inlet for different configurations with hinged and morphing flaps that were conducted through CFD simulations are presented and discussed in this Chapter. The results on the pressure recovery are presented in Section 5.1. The results of individual cases, hinged and morphing flap, will be compared and discussed. Furthermore, the envelopes of the pressure recovery will be presented. Section 5.2 presents the results on the drag of the NACA ram-air inlet for different test cases. Section 5.3 presents the pressure distributions between flap designs on different configurations. The vorticity plots are shown in Section 5.4. This is followed by Section 5.5 in which the distortion inside the duct of the NACA ram-air inlet will be presented.

5.1. PRESSURE RECOVERY

CFD simulations were conducted for a range of mass flow rates and various configurations with different designs of the closure flaps. Firstly, two different closure flap designs were analysed: the hinged flap and the morphing flap. Secondly, three different configurations from which the flap opening that is regulated by the closure flap mechanism has a minimum distance of 15, 55 and 95 $[mm]$. Thirdly, the mass flow rate was varied for the CFD simulations. The CFD simulations were performed for a range of mass flow rates.

One of the important inlet parameters is the pressure recovery. This section presents the inlet performance between the NACA ram-air inlet with the hinged flap and the morphing flap. The comparison of the pressure recovery between the hinged flap and the morphing flap is discussed in Subsection 5.1.1. This is followed by Subsection 5.1.2 in which the envelopes of the pressure recovery for the hinged flap and the morphing flap are presented.

5.1.1. PRESSURE RECOVERY HINGED-MORPHING COMPARISON

In order to assess and quantify the effect of replacing the conventional hinged flap by an inherently smoother morphing flap, the hinged flap and the morphing flap of each configuration will be compared. The pressure recovery of both different flap designs on Configurations 1, 2, and 3, is plotted against the mass flow rate in Figures 5.1, 5.2, and 5.3, respectively.

The pressure recovery of both different flap designs on Configuration 1 is plotted against the mass flow rate in Figure 5.1.

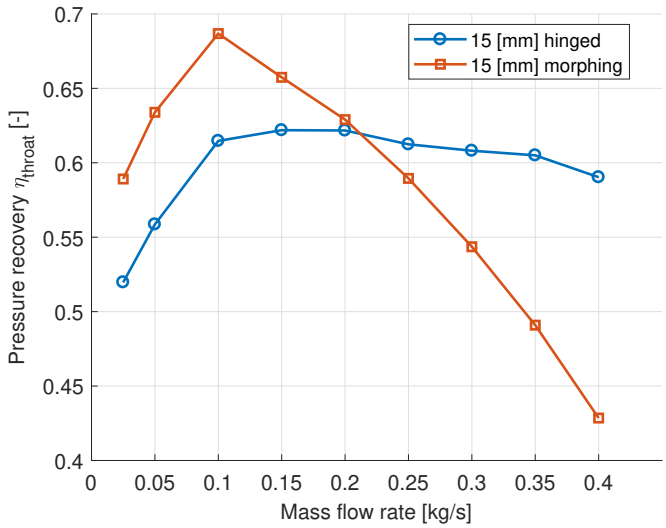

Figure 5.1: Comparison between the hinged and morphing flap of Configuration 1 with an opening of 15 $[mm]$. The pressure recovery is plotted as a function of the mass flow rate.

In Figure 5.1 it can be seen that Configuration 1 with the morphing flap shows a large variety of pressure recovery. The highest value of the pressure recovery is 0.687 and can be found at a mass flow rate of 0.100 $[kg/s]$ for the morphing flap. However, the pressure recovery declines sharply to a value of 0.429 with increasing mass flow rate. It is a different case for Configuration 1 with the conventional hinged flap. In this case, the highest pressure recovery equals 0.622 at the corresponding mass flow rate of 0.150 $[kg/s]$. However, the pressure recovery of the hinged flap has a wide plateau and fluctuates around 0.610, meaning that the pressure recovery remains relatively high and constant for a broad range of mass flow rate. The relative difference between the highest values of pressure recovery between the two flaps is slightly over 10%. For low mass flow rates, the morphing flap performs in terms of pressure recovery significantly better than the hinged flap, whereas the opposite happens at the breakpoint at a mass flow rate of 0.210 $[kg/s]$. For mass flow rates higher than 0.210 $[kg/s]$ the pressure recovery of the hinged flap gradually drops to 0.590, whereas the pressure recovery of the morphing flap drops drastically to 0.429.

The large difference in pressure recovery between the hinged flap and morphing flap at high mass flow rates can be explained as follows. The locations of the throat of the hinged flap and morphing flap of Configuration 1 are not the same. The influence of this geometrical difference is that the pressure recovery is also measured further downstream for the morphing flap. The flow travels a larger distance through the duct, which causes more pressure loss due to skin friction, reducing the measured pressure recovery.

The pressure recovery of both different flap designs on Configuration 2 is plotted against the mass flow rate in Figure 5.2.

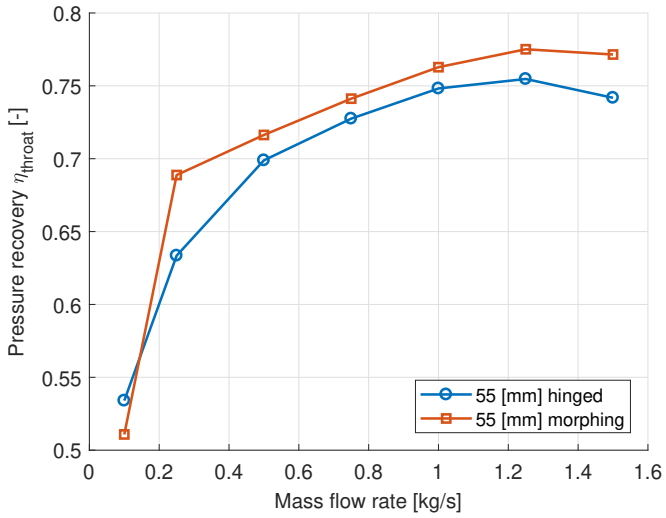

Figure 5.2: Comparison between the hinged and morphing flap of Configuration 2 with an opening of 55 $[mm]$. The pressure recovery is plotted as a function of the mass flow rate.

From the first observation of Figure 5.2, it can be observed that Configuration 2 with the morphing flap possess a higher pressure recovery than Configuration 2 with the hinged flap for most mass flow rates, apart from a mass flow rate of 0.100 $[kg/s]$. The pressure recovery of the morphing flap case shows a large jump from 0.511 to 0.689 between mass flow rates 0.100 and 0.250 $[kg/s]$. The pressure recovery of both flap designs on Configuration 2 increases with increasing mass flow rate up to maximum pressure recovery. The highest values of the pressure recovery of Configuration 2 are very similar and equal to 0.775 and 0.755 at a mass flow rate of 1.250 $[kg/s]$, for the morphing and hinged flap, respectively.

The pressure recovery of both different flap designs on Configuration 3 is plotted against the mass flow rate in Figure 5.3.

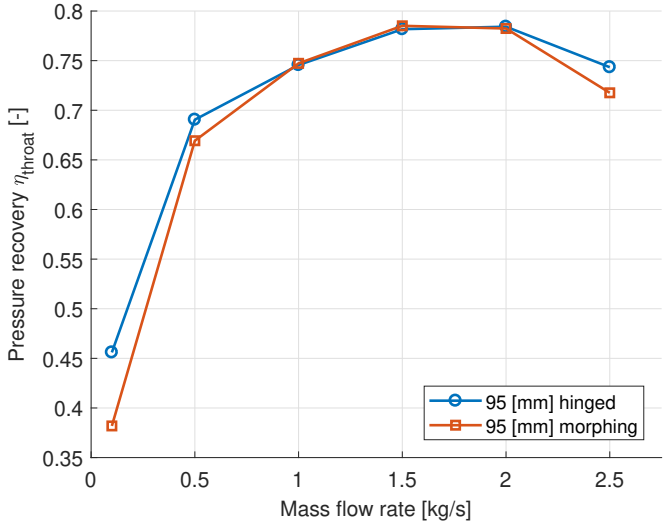

Figure 5.3: Comparison between the hinged and morphing flap of Configuration 3 with an opening of 95 $[mm]$. The pressure recovery is plotted as a function of the mass flow rate.

Figure 5.3 shows the pressure recovery of Configuration 3 of both hinged and morphing flaps as a function of the mass flow rate. The trend of the pressure recovery is very similar for both hinged and morphing flap. The maximum pressure recovery of Configuration 3 with a hinged flap equals 0.784 at a mass flow rate of 2.000 $[kg/s]$, whereas the maximum pressure recovery of Configuration 3 with a morphing flap equals 0.785 at a mass flow rate of 1.500 $[kg/s]$. Both hinged flap and morphing flap have very similar maximum pressure recovery.

At most mass flow rates, the pressure recovery of Configuration 3 with a morphing flap is lower than a hinged flap. This can be explained as follows. Figure 5.16 shows the shape of the hinged flap and the morphing flap. The morphing flap is much smoother than the hinged flap and the kinks have been eliminated in the morphing flap. Although the morphing flap is smoother, for this particular configuration, the ramp angle in the morphing flap case is much larger than the hinged flap. The hinged flap has a locally more strong ramp angle downstream of the ramp, but the effect of a large ramp angle along the entire morphing flap is more prominent. A large ramp angle provokes flow separation [5]. Second, increasing the ramp angle increases the obliquity between the freestream flow and the divergent ramp walls. This results that the flow has more difficulty to follow the shape of the divergent ramp walls, causing more high-energetic flow to spill over the NACA ram-air lip [5] [9]. These two adverse conditions, high obliquity and high spillage, cause large pressure losses. This resulted in a low pressure recovery for the morphing flap case.

5.1.2. ENVELOPE OF THE PRESSURE RECOVERY

In the previous Subsection, each Configuration has been compared with two flap designs, it can be concluded that the largest differences in pressure recovery were found for Configuration 1. Besides assessing the performance in terms of pressure recovery each configuration with two flap designs separately, it is useful to show the pressure recovery of all configurations for each flap design in a graph in order to present the overall pressure recovery profile of each flap design.

Figure 5.4a presents the results on the pressure recovery obtained from CFD simulations for the three configurations with the **hinged flap** as a function of the mass flow rate, whereas Figure 5.4b presents the results on the pressure recovery obtained from CFD simulations for the three configurations with the **morphing flap** as a function of the mass flow rate. The pressure recovery is measured at the throat area inside the NACA ram-air inlet.

The highest achievable pressure recovery per configuration is found for the morphing plate. For the configuration with a smaller opening, a larger difference in the maximum pressure recovery is found. The maximum pressure recovery that can be achieved with Configuration 1, 2, and 3 with a hinged flap are 0.622, 0.755, and 0.784, respectively. For Configurations 1,2 and 3 with morphing flap, the maximum values of the pressure recovery are 0.687, 0.775 and 0.785, respectively.

Firstly, a clear trend of the pressure recovery can be observed. The maximum achievable pressure recovery is related to the configuration. A large opening inside the NACA ram-aim inlet, which is defined by the throat area, allows a higher pressure recovery. In both Figures 5.4a and 5.4b, it can be seen that Configuration 3 with an opening of 95 $[mm]$ enables a maximum pressure recovery much higher than the maximum pressure recovery for Configuration 1 with an opening of 15 $[mm]$. This can be explained with the aspect ratio of the NACA ram-air inlet, but one must also remember that each configuration has a different throat area. The aspect ratio is defined as the ratio of the width of the NACA ram-air and the duct height inside the NACA ram-air inlet. For Configurations 1, 2, and 3, the aspect ratios are 20.3, 5.53, and 3.20, respectively. Although the throat area of each configuration is different, the streamtube that is ingested by the NACA ram-air inlet with a higher

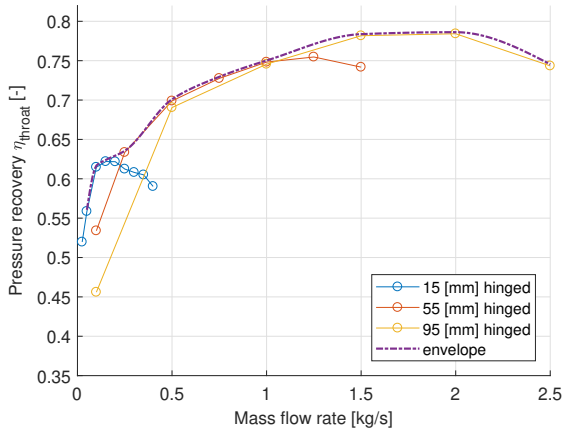

(a) The pressure recovery is shown for Configurations 1, 2 and 3 with a **hinged** flap with an opening of 15, 55 and 95 $[mm]$, respectively.

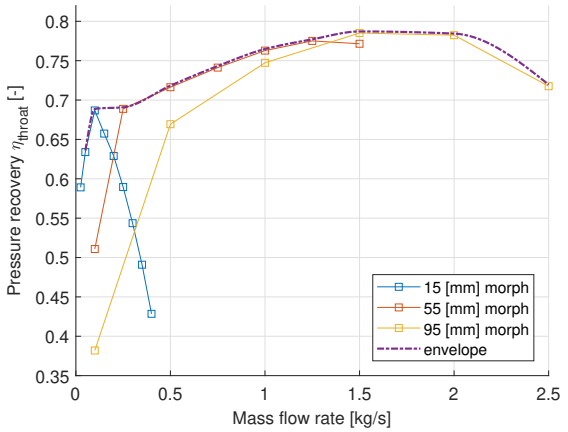

(b) The pressure recovery is shown for Configurations 1, 2 and 3 with a **morphing** flap with an opening of 15, 55 and 95 $[mm]$, respectively.

Figure 5.4: Pressure recovery at the cross-sectional area of the throat versus mass flow rate obtained from CFD simulations is plotted. The envelope of the maximum pressure recovery is plotted.

aspect ratio contains proportionally more boundary layer flow. Boundary layer flow is less energetic and slower than the freestream airflow, thereby decreasing the pressure recovery. Increasing the aspect ratio leads to an increase in the proportion of boundary layer that is ingested, which results in a reduction of the pressure recovery.

Secondly, the pressure recovery of any configuration increases with increasing mass flow rate until the maximum value of the pressure recovery has been reached. By increasing further increasing the mass flow rate, the pressure recovery drops. The increase of the pressure recovery by increasing the mass flow rate can be explained as follows. Due to the divergent shape of the NACA ram-air inlet, the airflow is forced to flow over the sharp ramp edges into the NACA ram-air inlet. This results in the generation of a vortex on each edge of the NACA ram-air inlet. The vortex curls over the edge towards the centreline of the NACA ram-air inlet and inwards to the ramp walls, thinning out the boundary layer at the centreline. For low mass flow rates, a larger portion of the airflow is not being ingested into the NACA ram-air inlet but spilt over the NACA ram-air lip. This will also be discussed in Section 5.4 on vorticity. Therefore, the effect of the vortices on the boundary layer is weaker. The boundary layer near the centreline of the NACA ram-air inlet will not be thinned out by the vortex, leading to a lower pressure recovery when the mass flow rate is lowered. When the mass flow rate is increased, the vortex strength will become stronger. The vortex curls over the edge of the NACA ram-air inlet and thins out the boundary layer. Higher energetic flow is ingested into the NACA ram-air inlet, resulting in a higher pressure recovery.

The decrease of the pressure recovery beyond its maximum value is due to the vortex that is being ingested by the inlet. Although the boundary layer around the ramp of the inlet is thinned out by the vortices, the amount of the vortex flow that is being ingested is higher at high mass flow rates. After vortices are generated, the vortex core will fade and dissipate its energy [51]. The pressure losses are caused due to the vortex cores, leading to lower pressure recovery. At the maximum pressure recovery, the loss due to boundary layer thickening and the pressure losses due to vortex ingestion are minimal.

In conclusion, increasing the mass flow rate increases the effect and the strength of the vortices that reduce the boundary layer thickness. The pressure losses due to vortices are low. Beyond the maximum pressure recovery, the effect of thinning out the boundary layer is outweighed by the detrimental effect of vortex ingestion. Vortex ingestion is high, which results in higher pressure losses due to vortex cores.

In both Figures 5.4a and 5.4b, the envelope corresponds to the maximum pressure recovery that can be achieved for a certain mass flow rate. This is particularly useful for the air-conditioning system as it can monitor and select the best configuration for maximum pressure recovery at a certain mass flow rate (without considering the corresponding drag coefficient). Looking at Figure 5.4a, when a mass flow rate of 1.500 $[kg/s]$ is required as the amount of coolant air for the heat exchanger, it is more beneficial to select Configuration 3 with a hinged flap instead of Configuration 2 with a hinged flap. The pressure recovery of Configuration 3 and 2 are 0.782 and 0.742, respectively, which is a relative improvement of 5.4%.

Figure 5.5 shows the envelopes of the pressure recovery for both configurations. The envelopes are extracted from Figures 5.4a and 5.4b.

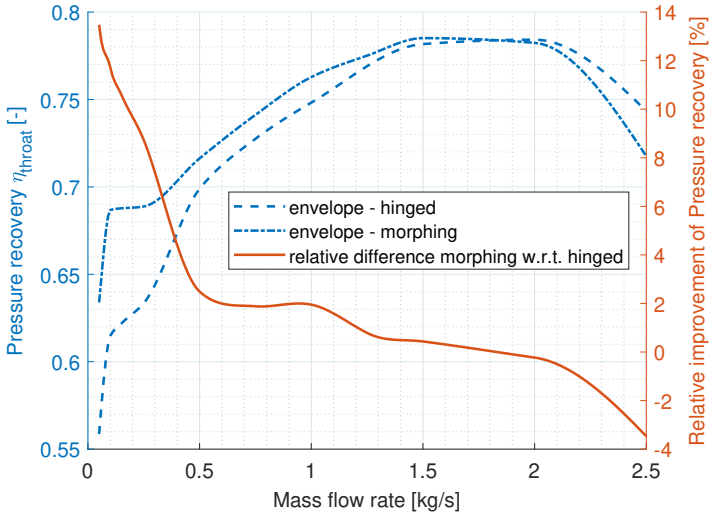

Figure 5.5: The envelopes pressure recovery of the designs with morphing and hinged flaps are shown in blue. The relative difference of pressure recovery envelopes of the morphing flap with respect to the hinged flap is shown in orange.

By analysing the blue lines in the graph which shows the envelope of the pressure recovery as a function of the mass flow rate, it can be seen that the configuration with morphing flap has a higher pressure recovery envelope than the configuration with hinged flap for a broad range of mass flow rates. The opposite holds for a mass flow rate higher than 1.870 $[kg/s]$, where the configuration with morphing flap possesses a lower value of pressure recovery than the hinged-plated configuration. Furthermore, it can be seen that the envelopes of both configurations with morphing and hinged flaps converge between mass flow rates between 1.500-2.000 $[kg/s]$. The envelope will not extend further upwards since the maximum flap opening is equal to 95 $[mm]$.

By calculating the relative difference of the pressure recovery of the configuration with morphing flap with respect to the configuration with hinged flap, the relative improvement in pressure recovery is indicated by the orange line in Figure 5.5. This can be interpreted as a measure of the improvement or deterioration of the performance of the NACA ram-air inlet by replacing the conventional closure flap mechanism, the hinged flap, by a morphing flap. The relative improvement of

the pressure recovery is the highest at low mass flow rates. The relative improvement of the pressure recovery of Configuration 1 with a morphing flap with respect to a hinged flap can go up to 13.5%. The relative improvement rapidly drops to 2.49% for a mass flow rate of 0.500 $[kg/s]$. Between a mass flow rate of 0.500-1.870 $[kg/s]$ the difference of pressure recovery between the two configurations is small.

In summary, the morphing flap provides a significant improvement in terms of pressure recovery, compared to the hinged flap. The largest improvement can be found for low mass flow rates and goes up to 13.5%. The largest relative improvement in pressure recovery was found for Configuration 1 with morphing flap compared to Configuration 1 with hinged flap. At high mass flow rates, the hinged plate performs better than the morphing flap by a narrow margin.

5.2. DRAG

Another important performance parameter is the drag. Although an improved pressure recovery is desirable, a large increase of drag is detrimental to the overall performance of the NACA ram-air inlet. Therefore, it is important to assess the drag increase/decrease by replacing the hinged flap with the morphing flap. The drag is calculated by using the operating conditions and the reference area of the Airbus A320, which equals to 122.4 $[m^2]$ [52].

The drag coefficient of both flap designs of each individual Configurations 1, 2, and 3, are plotted in Figures 5.6a, 5.6b, and 5.6c, respectively (shown on the next page). The relative difference between the drag coefficient of the morphing flap with respect to the hinged flap is also plotted.

By looking at Figures 5.6a and 5.6b, a general trend can be noticed for Configuration 1 and 2. At low mass flow rates, the configurations with the morphing flap have a lower drag coefficient. At high mass flow rates, the opposite holds. The configurations with the hinged flap have a lower coefficient. This trend is slightly different in Configuration 3. In Figure 5.6c, it can be seen that the drag coefficient of the morphing flap case is higher than the hinged flap case at low mass flow rates. Then the drag coefficient of the morphing flap is lower at moderate mass flow rates, and the drag coefficient of the morphing flap is again higher at high mass flow rates.

Figure 5.6a shows the drag coefficient as a function of mass flow rate for Configuration 1 of both hinged and morphing flaps.

From Figure 5.6a it can be seen that the drag coefficient of the morphing flap is lower than the hinged flap at a low mass flow rate, but the difference in drag coefficient seems to be small. By looking at the relative difference of the drag coefficient of the morphing flap case with respect to the hinged flap in percentage, it can be seen that the difference in drag coefficient is rather large. At low mass flow rates, the maximum drag improvement of using a morphing flap instead of a hinged flap is 33.1%. At mass flow rates of 0.150 $[kg/s]$ and higher, the performance in drag of the morphing flap is worse than the morphing flap.

Figure 5.6b shows the drag coefficient as a function of mass flow rate for Configuration 2 of both hinged and morphing flaps.

From Figure 5.6b it can be seen that the drag coefficient of the morphing flap is lower than the hinged flap at a low mass flow rate. The largest drag improvement of the morphing flap compared to the hinged flap case is 17.8%. The opposite holds when the mass flow rate is increased above 0.550 $[kg/s]$. The drag coefficient of the morphing flap case starts to increase significantly compared to the hinged flap case. The drag increase of the morphing flap compared to the hinged flap case is 30.1% at a mass flow rate of 1.000 $[kg/s]$. In Subsection 5.1.1, it was found that Configuration 2 with

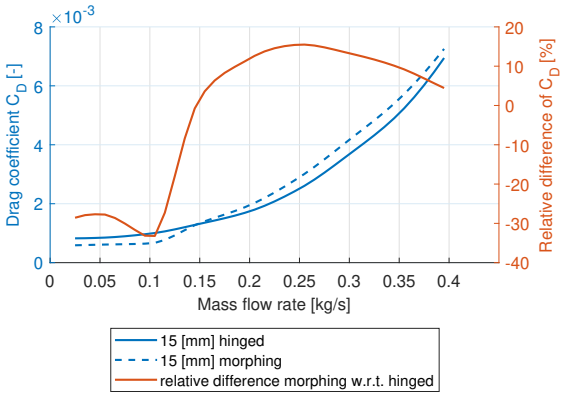

(a) Configuration 1 with an opening of 15 [mm] - the hinged flap and the morphing flap

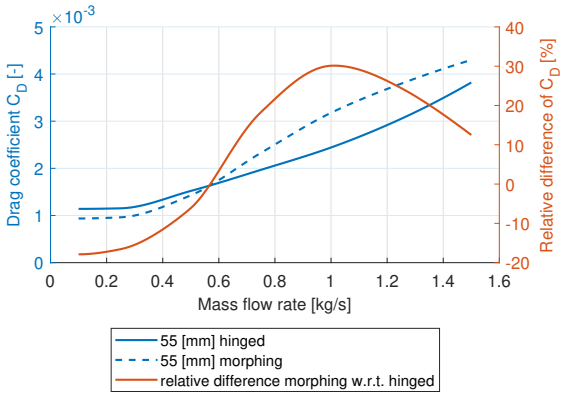

(b) Configuration 2 with an opening of 55 [mm] - the hinged flap and the morphing flap

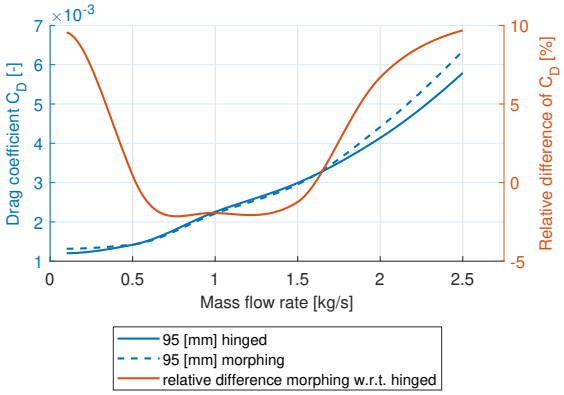

(c) Configuration 3 with an opening of 95 [mm] - the hinged flap and the morphing flap

Figure 5.6: Comparison of the drag coefficient between the hinged and morphing flap of each configuration on the left axis. The drag coefficient is plotted as a function of the mass flow rate. The relative difference of the drag coefficient between the morphing and hinged flap in percentage is plotted on the right axis.

morphing flap has a higher performance in terms of the pressure recovery for a broad range of mass flow rates. The drag penalty of using the morphing flap is large that it may offset the performance gain in the pressure recovery.

Figure 5.6c presents the drag coefficient as a function of mass flow rate for Configuration 3 of both hinged and morphing flaps.

As can be seen from Figure 5.6c, the drag coefficient of both flaps shows that the drag coefficient increases with increasing mass flow rate. Especially between mass flow rates of 0.500 and 1.500 $[kg/s]$ the drag coefficients are very similar. From a mass flow rate higher than 1.500 $[kg/s]$ the morphing flap performs worse compared to the hinged flap. The same holds for low mass flow rates between 0.100-0.500 $[kg/s]$ where the drag coefficient is also higher for the morphing plate with respect to the hinged flap. The relative difference of the morphing flap compared to the hinged flap in Configuration 3 is not as large as in Configurations 1 and 2. This can be explained by the fact that geometrical differences between Configuration 3 with the hinged flap and the morphing flap are less strong. Although Kink no.1 and Kink no.2 are present in the hinged flap of Configuration 3, the shape of the morphing flap of Configuration 3 is very similar. The geometrical shapes of the morphing flap and hinged flap in Configuration 1 and 2 are due to deflection of the actuator more different.

5.2.1. ENVELOPE OF THE DRAG

Figure 5.7a presents the results on the drag count obtained from CFD simulations for the three configurations with a **hinged flap** for different mass flow rates, whereas Figure 5.7b presents the results on the drag count obtained from CFD simulations for the three configurations with a **morphing flap** for different mass flow rates. The drag count is calculated by using the reference area of the Airbus A320, which equals to 122.4 $[m^2]$ [52].

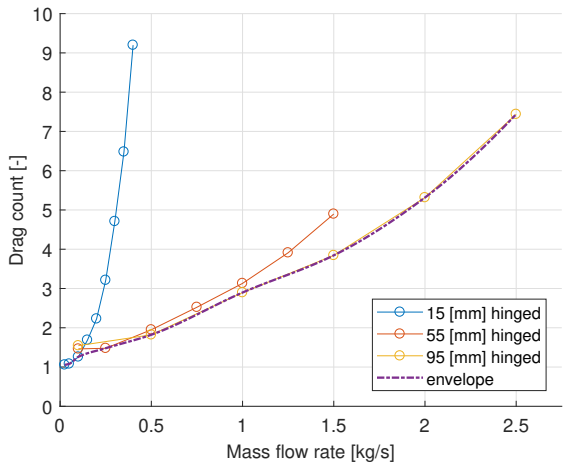

(a) The drag count is shown for Configurations 1, 2 and 3 with a **hinged** flap with an opening of 15, 55 and 95 $[mm]$, respectively.

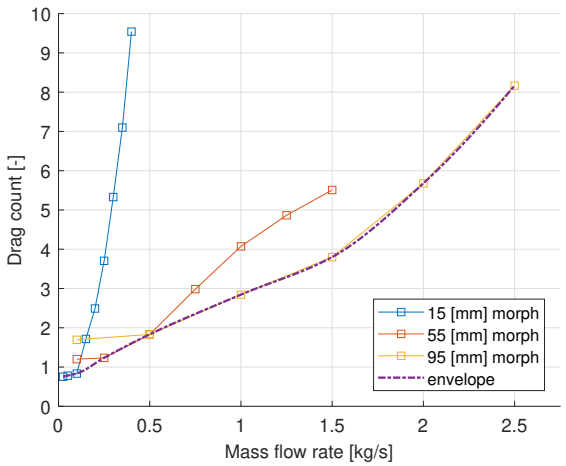

(b) The drag count is shown for Configurations 1, 2 and 3 with a **hinged** flap with an opening of 15, 55 and 95 $[mm]$, respectively.

Figure 5.7: Drag count of the NACA ram-air inlet and the fuselage skin versus mass flow rate obtained from CFD simulations is plotted. The envelope of the minimum drag count for a given mass flow rate is plotted.

The similar method from the previous section on the pressure recovery plots can be done with the drag. The envelopes of the drag counts versus the mass flow rate for the two sets of configurations with a hinged and a morphing flap have been extracted and are plotted as the blue dotted lines in Figure 5.5. The relative difference of the drag counts of the configuration with morphing flap with respect to the configuration with the hinged flap was calculated and it is plotted as the relative improvement of the drag counts in percentage indicated by the orange line in Figure 5.8.

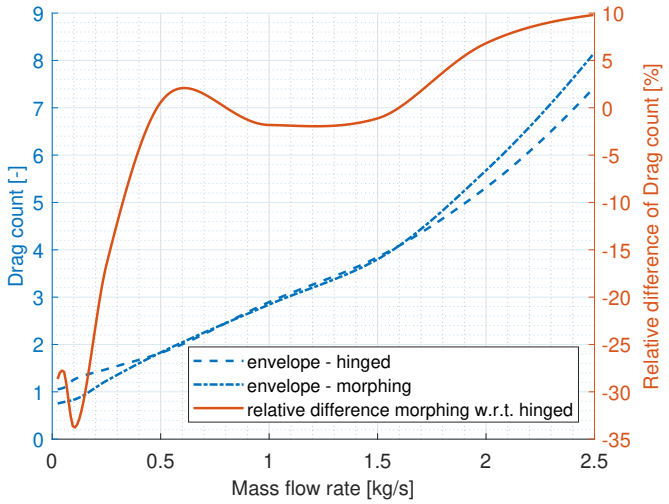

Figure 5.8: The envelopes drag counts of the designs with morphing and hinged flaps are shown in blue. The relative difference of pressure recovery envelopes of the morphing flap with respect to the hinged flap is shown in orange.

From Figure 5.8, it can be observed that the configuration with morphing has an improvement in

its drag performance for a broad range of low mass flow rates. The largest improvement in drag can be found for low mass flow rates, especially for configuration with the smallest throat area: Configuration 1 with an opening of 15 $[mm]$. By investigating the drag envelope, the maximum improvement of the drag of the morphing flap with respect to the hinged flap is 33.8%. The improvement in drag is positive between 0.025 and 0.480 $[kg/s]$. Then the drag improvement is negative and becomes positive again with a drag improvement of around 1.8% between mass flow rates 0.800 and 1.600 $[kg/s]$. The drag count improvement is negative above a mass flow rate of 1.600 $[kg/s]$ with a deterioration of 9.80% for a mass flow rate of 2.500 $[kg/s]$. The highest improvement in terms of drag counts was found in Configuration 1.

Typically, 1.2 $[kg/s]$ of air is required for the ventilation requirement inside the cabin of an Airbus A320 with 200 passengers [12]. Half of the cabin air is recirculated, which means that 0.6 $[kg/s]$ of bleed air is required [53]. According to Martinez, the amount of coolant air is two times the amount of bleed air [12]. By looking at Figure 5.8 for a mass flow rate of 0.6 $[kg/s]$ (since half of the geometry was modelled), it can be seen that the difference in drag counts between the hinged flap and the morphing flap is very small, it is equal to 2.00%. The drag count of Configuration 1 with the hinged flap and the morphing flap is 2.0360 and 1.9948, respectively. The difference between the hinged flap and the morphing flap is 0.0412 drag count. The drag improvement of using the morphing flap design is minimal in comparison to the total drag of an aircraft. Since the CFD simulations of the NACA ram-air inlets were analysed at Mach 0.20, the calculations for the fuel savings cannot be performed for the flight segment at cruise speed.

5.3. PRESSURE DISTRIBUTION OF THE CLOSURE FLAP

The main geometrical difference between the designs of the configuration with a hinged flap and the configuration with the morphing flap is originated in the closure flap. For the hinged flap, two kinks in the flap are present. It was defined that Kink no.1 is located in the middle of the first rigid plate and Kink no.2 is located between the two rigid plates. These two kinks have been eliminated in the morphing flap. It is expected that the undesirable aerodynamic effect will be reduced or even be eliminated by using a morphing flap. The pressure distribution of the lower surface of the NACA ram-air inlet, which consists of the ramp surface and the surface of the closure flap, will be discussed.

Previously, it was observed that the largest differences in drag and the largest improvement of the drag are originated from Configuration 1 with an opening of 15 $[mm]$. This is a good reason to zoom in on the geometry of the different flap designs.

Figures 5.9 and 5.10 show the side view of the NACA ram-air inlet of Configuration 1 with the hinged and the morphing flap, respectively. The location in the x-direction is indicated with the normalised distance x/c, where $x/c = 0$ is the location of the start of the NACA ram-air inlet and $x/c = 1$ is the location at the NACA ram-air lip.

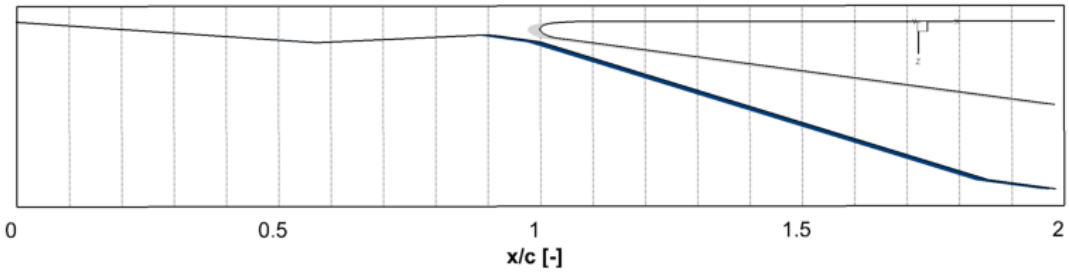

Figure 5.9: Side view of Configuration 1 - 15 [mm] opening with **hinged flap** of the lower surface of the NACA ram-air inlet and the upper and lower surface around the NACA ram-air lip: The lower surface of the NACA ram-air inlet is indicated in blue.

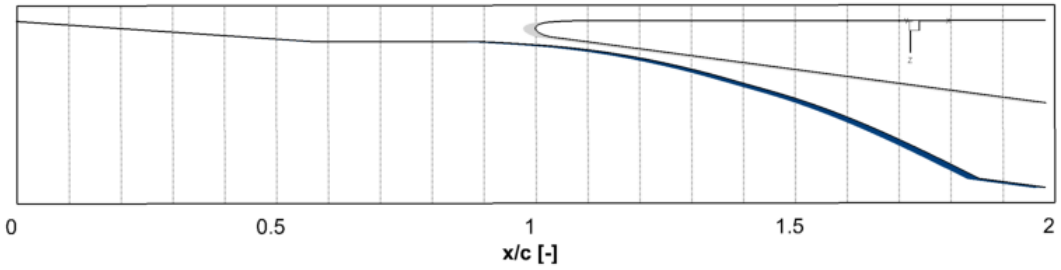

Figure 5.10: Side view of Configuration 1 - 15 [mm] opening with **morphing flap** of the lower surface of the NACA ram-air inlet and the upper and lower surface around the NACA ram-air lip: The lower surface of the NACA ram-air inlet is indicated in blue.

From Figure 5.9, it can be seen that Configuration 1 with an opening of 15 [mm] with a hinged flap has three kinks. One kink on the closure flap is located around $x/c = 0.55$ at the 'axis of rotation' at which the hinged flap is attached to. The other two kinks were introduced as Kink no.1 and Kink no.2 in Figure 3.7. Kink no.1 is located around $x/c = 0.90$ and Kink no.2 which is located downstream of the closure flap, is located around $x/c = 1.0$ in the vicinity of the NACA ram-air lip. The latter kink between two rigid plates, Kink no.2, has been presented earlier as the source of pressure losses and airframe vibration during flight. Figure 5.10 shows the side view of the NACA ram-air inlet of Configuration 1 with an opening of 15 [mm] with a morphing flap. Both Kinks no.1 and no.2, that are present in the hinged flap case, have been eliminated in the morphing flap. The closure flap is slightly curved and smooth due to the deflection of the actuator. The morphing flap is attached to the 'axis of rotation' at which a subtle kink is present.

The comparison of the C_p-plots of the ramp floor and the closure flap of the NACA ram-air inlet between the hinged flap and the morphing flap of Configuration 1 with an opening of 15 [mm] is shown in Figure 5.11.

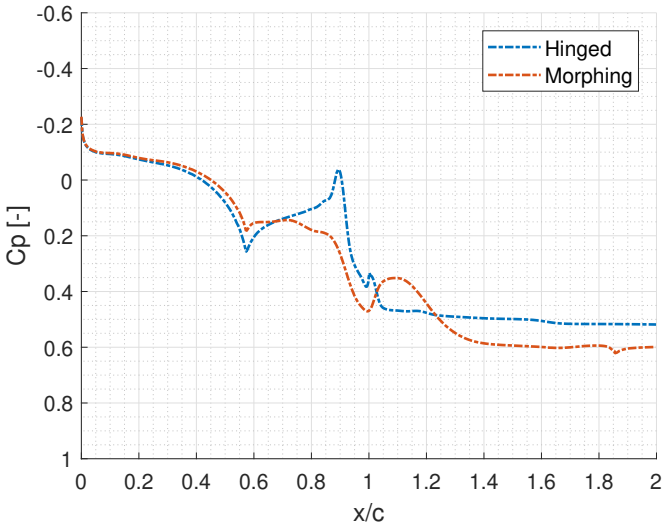

Figure 5.11: C_p-plots of Configuration 1 - 15 $[mm]$ opening with **hinged flap** and **morphing flap**. x/c is the normalised x-distance.

From the observation of Figure 5.11, a pressure peak can be found around $x/c = 0.55$, which is the location of the 'axis of rotation' for both hinged and morphing cases. This kink is more subtle in the case of a morphing flap, causing a less strong pressure peak in the C_p-plot.

It can be observed that the C_p-plot of Configuration 1 with the hinged flap shows a suction peak near $x/c = 0.90$. This is the location of Kink no.1 of Configuration 1 with an opening of 15 $[mm]$. The local convex curvature leads to higher supervelocity, thus a locally less positive or more negative pressure coefficient [54]. When this is compared with the morphing case, one can observe that the suction peak has been eliminated. The Kink no.1, which is found in the middle of the first rigid plate of the hinged flap, is smoothed out in the morphing case. The morphing flap is a smooth surface, even when the laminated plate is deflected due to the actuator. This results in a reduction of the supervelocity that would have caused in the present of the sharp kink, reducing the magnitude of the adverse pressure gradient such that flow separation is postponed.

Furthermore, there is a small suction peak around $x/c = 1.0$. This is the location of Kink no.2 in the case of a hinged flap. A peak around $x/c = 1.1$ can be found for the morphing case. This can be explained by recalling Figure 5.10, which shows the side view of the morphing flap in the vicinity of the NACA ram-air inlet. The throat is now located more downstream from the NACA ram-air lip. Since the throat is located downstream in the duct, the velocity increases due to the convergent shape of the duct.

Figures 5.12 and 5.13 show the side view of the NACA ram-air inlet of Configuration 2 with the hinged and the morphing flap, respectively.

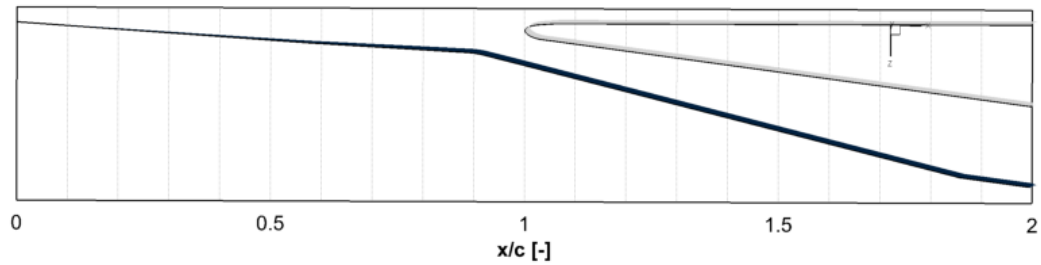

Figure 5.12: Side view of Configuration 2 - 55 [mm] opening with **hinged flap** of the lower surface of the NACA ram-air inlet and the upper and lower surface around the NACA ram-air lip: The lower surface of the NACA ram-air inlet is indicated in blue.

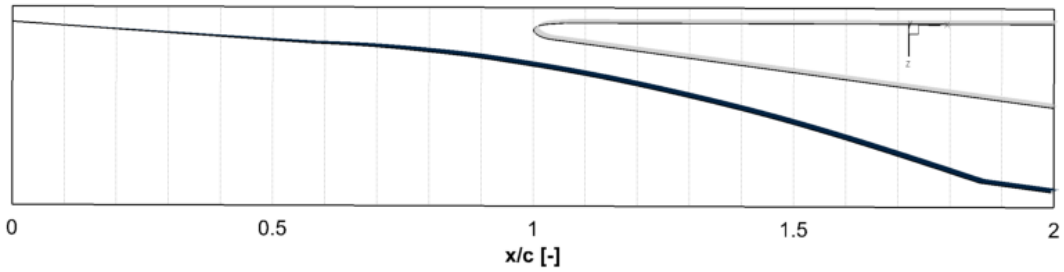

Figure 5.13: Side view of Configuration 2 - 55 [mm] opening with **morphing flap** of the lower surface of the NACA ram-air inlet and the upper and lower surface around the NACA ram-air lip: The lower surface of the NACA ram-air inlet is indicated in blue.

From Figure 5.12, it can be seen that Configuration 2 with an opening of 55 [mm] with a hinged flap two kinks. One kink on the closure flap is located around $x/c = 0.55$ at the 'axis of rotation' at which the hinged flap is attached to. The other kink is the Kink no.1 located around $x/c = 0.90$ on the first rigid plate of the hinged flap. As explained earlier, Kink no.2 is a pronounced kink at the hinge for certain deflections. For Configuration 2 with an opening of 55 [mm], there is a smoother transition between the two rigid plates such that Kink no.2 has a relatively favourable geometry. In a general case, Kink no.2 shall be located around $x/c = 1.0$ beneath the NACA ram-air lip. In Figure 5.12, Kink no.2 is hardly visible. Figure 5.13, it can be seen that the morphing flap is very smooth. One thing to mention is the 'axis of rotation' around $x/c = 0.55$, which is slightly less smooth in the morphing flap case compared to the hinged flap case.

Figure 5.14 shows the C_p-plots of the ramp floor and the closure flap of the NACA ram-air inlet between the hinged flap and the morphing flap of Configuration 2 with an opening of 55 [mm].

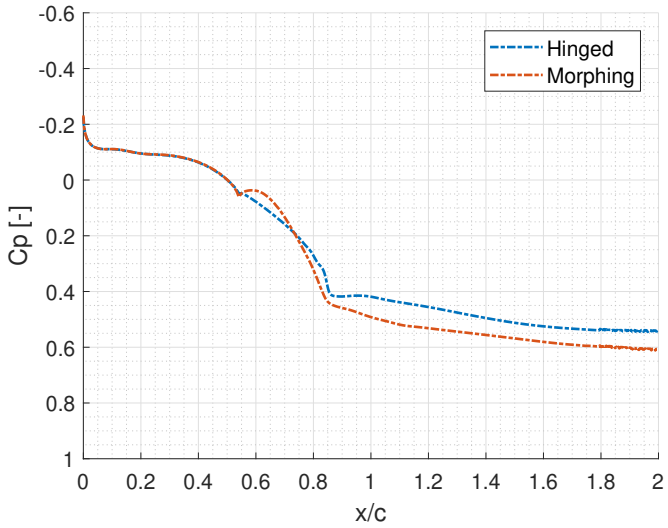

Figure 5.14: C_p-plots of Configuration 2 - 55 $[mm]$ opening with **hinged flap** and **morphing flap**. x/c is the normalised x-distance.

In Figure 5.14, it can be seen that there is a suction peak around $x/c = 0.55$ for the morphing flap case. As explained earlier, this location of the 'axis of rotation' of the flap is slightly less smooth in the morphing flap case compared to the hinged flap case, therefore causing a suction peak. Since the geometry of the morphing flap at this particular point is still smooth, the suction peak is not very strong. There is no suction peak present in the hinged flap case because the transition at the 'axis of rotation' of the flap is very smooth. The pressure peak is followed by an adverse pressure gradient up to $x/c = 0.90$ the location of Kink no.2 in the hinged flap. The pressure increases gradually beyond the NACA ram-air lip into the duct.

Figures 5.15 and 5.16 show the side view of the NACA ram-air inlet of Configuration 3 with the hinged and the morphing flap, respectively.

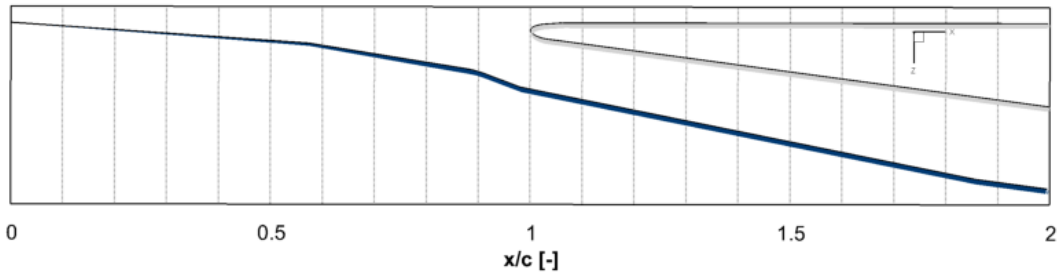

Figure 5.15: Side view of Configuration 3 - 95 $[mm]$ opening with **hinged flap** of the lower surface of the NACA ram-air inlet and the upper and lower surface around the NACA ram-air lip: The lower surface of the NACA ram-air inlet is indicated in blue.

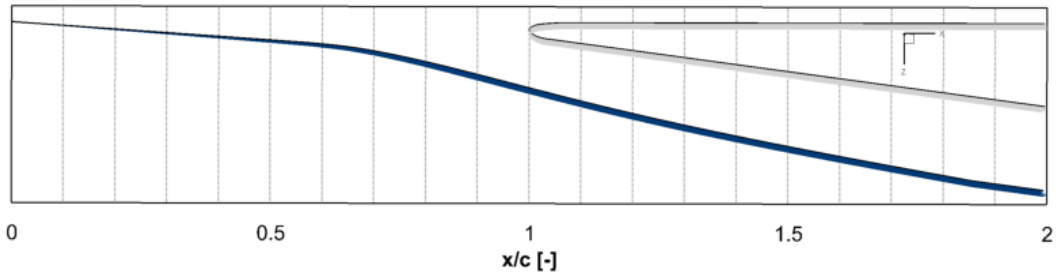

Figure 5.16: Side view of Configuration 3 - 95 [mm] opening with **morphing flap** of the lower surface of the NACA ram-air inlet and the upper and lower surface around the NACA ram-air lip: The lower surface of the NACA ram-air inlet is indicated in blue.

From Figure 5.15, it can be seen that Configuration 3 with an opening of 95 [mm] with a hinged flap has three kinks, similar to Configuration 1 with an opening of 15 [mm] with a hinged flap. One kink is present around $x/c = 0.55$ at the 'axis of rotation' of the hinged flap. Kink no.1 is located around $x/c = 0.90$ and Kink no.2, which is located downstream of the closure flap, is located slightly forward of $x/c = 1.0$. Kink no.2 in Configuration 3 is different from Kink no.2 in Configuration 1; the local curvature in Configuration is concave, whereas the local curvature in Configuration 1 is convex. It is expected that a local concave curvature results in lower supervelocity, thus a locally more positive or less negative pressure coefficient [54].

The comparison of the C_p-plots of the ramp floor and the closure flap of the NACA ram-air inlet between the hinged flap and the morphing flap of Configuration 3 with an opening of 95 [mm] is shown in Figure 5.17.

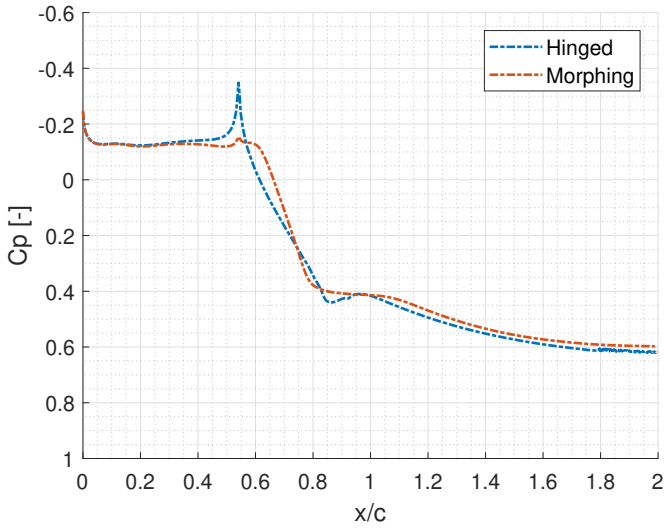

Figure 5.17: C_p-plots of Configuration 3 - 95 [mm] opening with **hinged flap** and **morphing flap**. x/c is the normalised x-distance.

In Figure 5.17, it can be seen that the case with hinged flap produces a very strong suction peak at $x/c = 0.55$. This is caused by the local convex curvature in the geometry. At the same location in the case with morphing flap, it can be seen that the suction peak is not present, and the pressure increases gradually. The location $x/c = 0.90$ at which Kink no.1 is located in the hinged flap case shows an increase of supervelocity due to the local convex curvature. Since the geometry is directly followed by a local concave curvature, it has prevented a strong suction peak between $x/c = 0.90$ and $x/c = 1.0$.

5.4. VORTICITY

Since the NACA ram-air inlet has the characteristics that a pair of vortices is generated at the sharp ramp edges, it is relevant to investigate the effect of vorticity on the inlet performance [16]. The vorticity plots will be presented in this section.

For the investigation of the vorticity, two locations around the NACA ram-air inlet on the fuselage were investigated. The midplane and the duct entrance plane are illustrated in Figure 5.18.

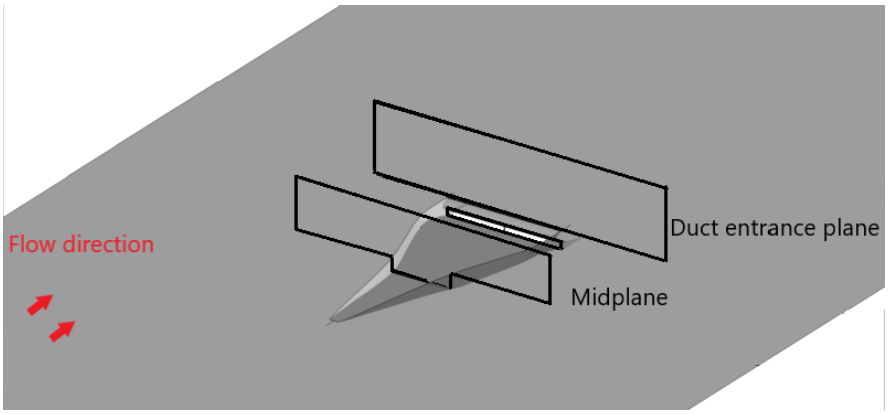

Figure 5.18: The location of the midplane and the duct entrance plane

Figures 5.19a and 5.19b show the vorticity plot at the midplane of Configuration 1 at a mass flow rate 0.100 $[kg/s]$ between the hinged flap and morphing flap design.

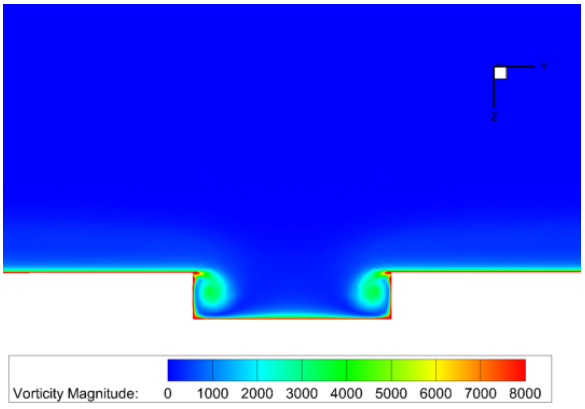

(a) Configuration 1 with a hinged flap - mass flow rate of 0.100 $[kg/s]$

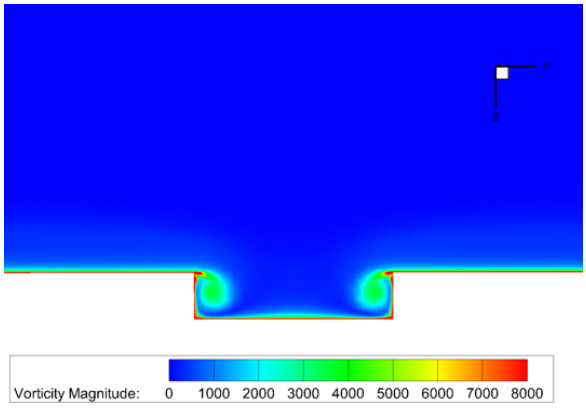

(b) Configuration 1 with a morphing flap - mass flow rate of 0.100 $[kg/s]$

Figure 5.19: Vorticity-plots at the midplane for Configuration 1 with a hinged flap and a morphing flap at a mass flow rate 0.100 $[kg/s]$

In these figures, it can be seen that there are two regions with high vorticity flow around the edges of the NACA ram-air with hinged flap and the morphing flap. These are originated from the pair of vortices that is generated around the edges of the ramp for a NACA ram-air inlet. The pair of vortices swirls around the edge towards the ramp floor of the NACA ram-air inlet, thinning out the boundary layer. Then, since the vortices rotate towards the ramp walls (vertical sides), this results in a thicker boundary layer.

The vorticity plots at the midplane showed that vortices were formed at the edges of the NACA ram-air inlet. The investigation on the vorticity continues with the vorticity plots at the duct entrance plane, which is located further downstream along the fuselage. Figures 5.20a and 5.20b show the vorticity strength at the duct entrance plane of Configuration 1 with a hinged flap and a morphing flap at a mass flow rate 0.100 $[kg/s]$, respectively.

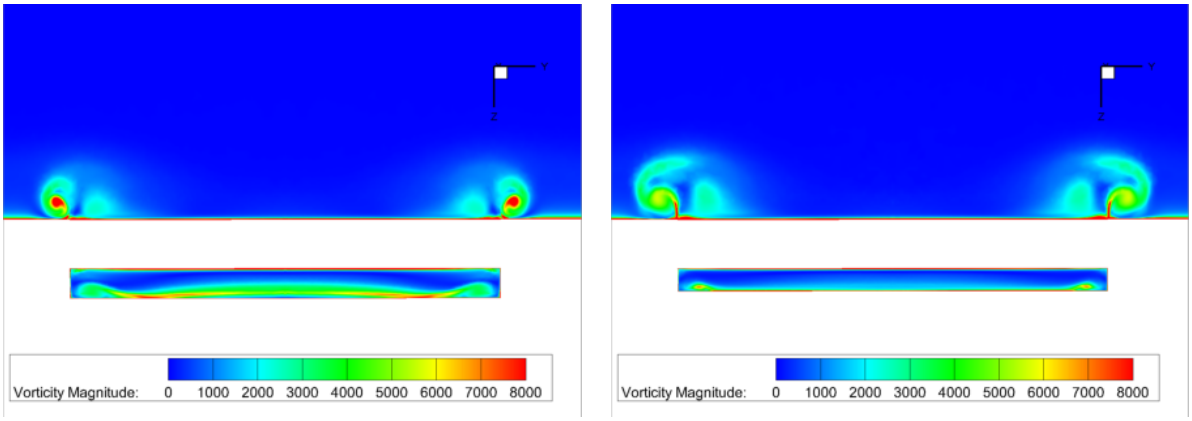

(a) Configuration 1 with a hinged flap - mass flow rate of 0.100 $[kg/s]$

(b) Configuration 1 with a morphing flap - mass flow rate of 0.100 $[kg/s]$

Figure 5.20: Vorticity-plots at the duct entrance plane for Configuration 1 with a hinged flap and a morphing flap at a mass flow rate 0.100 $[kg/s]$

One must notice that there are two regions are visible in both Figures 5.20a and 5.20b. The NACA ram-air lip divides the duct and the fuselage. A portion of the flow has entered the duct, while the other portion flows over the fuselage. From Figures 5.20a and 5.20b, it can be seen that vortex structures are present on the fuselage skin, outside of the duct of the NACA ram-air inlet. The vortex flow is originated from the vortices that were generated by the edges of the NACA ram-air inlet, previously explained in Figures 5.19a and 5.19b. There is a difference in the vortices between the two cases. The vortex core that flows over the fuselage is stronger for the case with the hinged flap than the case with the morphing flap. Another detail that can be spotted, the amount of vortex flow that is ingested into the duct of the NACA ram-air inlet is higher for the hinged flap case, indicated by the high vorticity region in green in Figure 5.20a. The ingestion of vortex flow by the NACA ram-air inlet decreases the inlet performance.

Previously, Configurations 1 with a hinged flap and morphing flap at a mass flow rate of 0.100 $[kg/s]$ were compared. In order to gain more understanding about the behaviour of the vortex flow around the NACA ram-air inlet, the vorticity plots of the same Configuration 1 at a higher mass flow rate of 0.300 $[kg/s]$ will be presented.

Figures 5.21a and 5.21b show the vorticity strength at the plane of the duct entrance of Configuration 1 with a hinged flap and a morphing at a mass flow rate 0.300 $[kg/s]$, respectively.

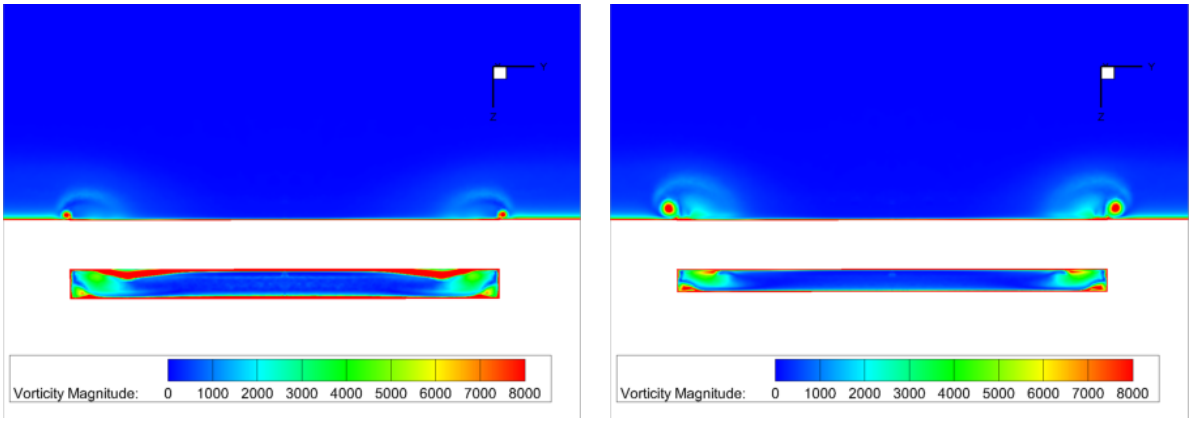

(a) Configuration 1 with a hinged flap - mass flow rate of 0.300 $[kg/s]$

(b) Configuration 1 with a morphing flap - mass flow rate of 0.300 $[kg/s]$

Figure 5.21: Vorticity-plots at the duct entrance plane for Configuration 1 with a hinged flap and a morphing flap at a mass flow rate 0.300 $[kg/s]$

From Figures 5.21a and 5.21b, it can be seen that there are vortex structures present inside the duct and outside near the fuselage. For Figure 5.21a, Configuration 1 with a hinged flap shows that a large amount of vortex flow is ingested into the duct. The high turbulent flow is located near the sides and the top surface of the duct. This is different in the other case, Configuration 1 with a morphing flap, as less vortex flow is ingested by the duct and more vortex flow is spilt over the lip to the fuselage. The two vortex structures near the fuselage can be seen in the morphing flap case, shown in Figure 5.21b. These structures have higher core strength and are larger in size in the morphing flap case. Increasing the mass flow rate causes the vortex strength to be stronger, but also a larger portion of the vortex flow is ingested into the duct.

The vorticity plots were analysed at the midplane and duct entrance plane, which are perpendicular with the flow direction. The side view of the vorticity plots of Configuration 1 with mass flow rates of 0.100 and 0.300 $[kg/s]$ are shown in Figures 5.22 and 5.23, respectively. In each figure, both hinged and morphing cases are illustrated.

From Figures 5.22 and 5.23 (shown on the next page), it can be observed that the strong vortices are generated around the ramp edges of the NACA ram-air ramp walls. The vortex flow is located mainly around the edge in the upstream part of the NACA ram-air inlets. Furthermore, the strong vortex flow is mainly found on the ramp of the NACA ram-air inlet (vorticity region in red). The high vorticity flow removes the low-energetic part of the boundary layer, such that a larger proportion of high energetic air is ingested by the inlet.

By further investigation, the vortex flow is split into two portions by the NACA-ram inlet lip, which was also concluded from the vorticity plots at the midplane and duct entrance plane. In Figure 5.22, only a small amount of the flow is ingested by the duct internally, while a large portion of the flow is spilt over the lip and passed over the fuselage externally which is shown by the wide vortex tube.

The vorticity plots of the side view of the NACA ram-air inlet shows the development of the vortices inside the duct of the NACA ram-air inlet. Another difference between the hinged flap and morphing flap case can be pointed out. From Figure 5.23, it can be seen that vortices are ingested into the duct of the NACA ram-air inlet. In the morphing case, the stronger vortices over a larger distance in the duct cause high pressure losses, resulting in a decrease of the inlet performance.

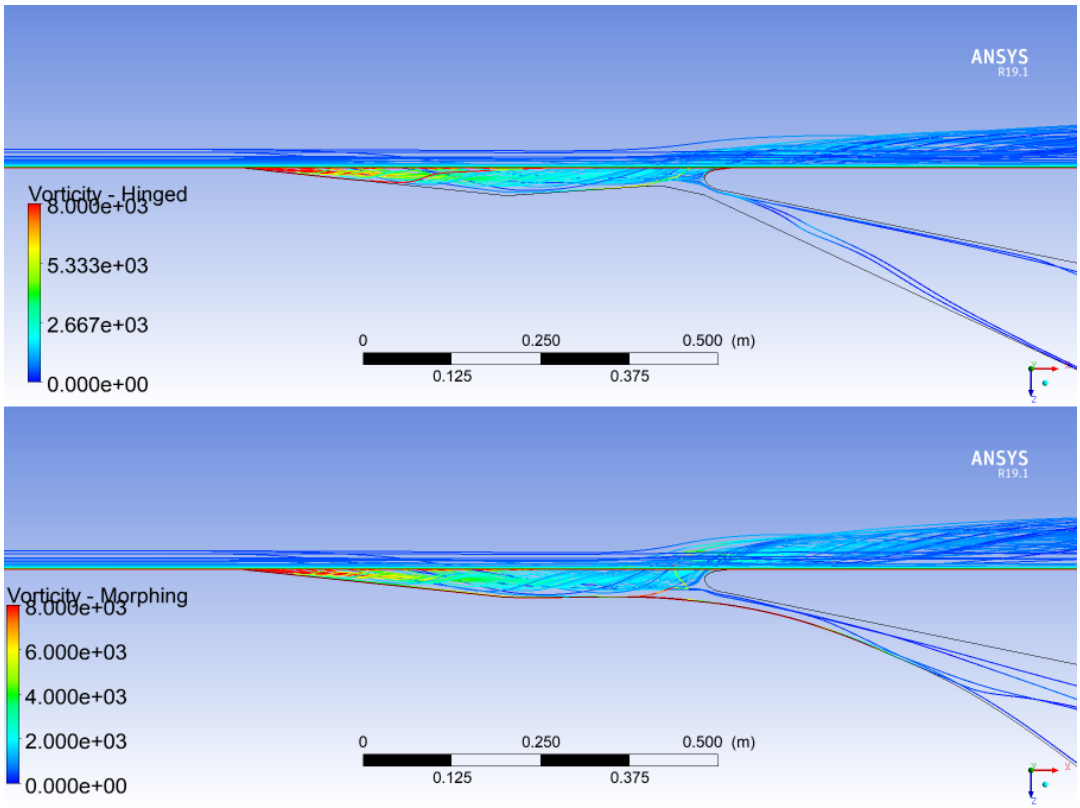

Figure 5.22: Side view of the NACA ram-air inlet. Configuration 1 with a mass flow rate of 0.100 $[kg/s]$. The vorticity strength $[1/s]$ is plotted with the streamlines of the airflow. Top shows the hinged case, bottom shows the morphing case.

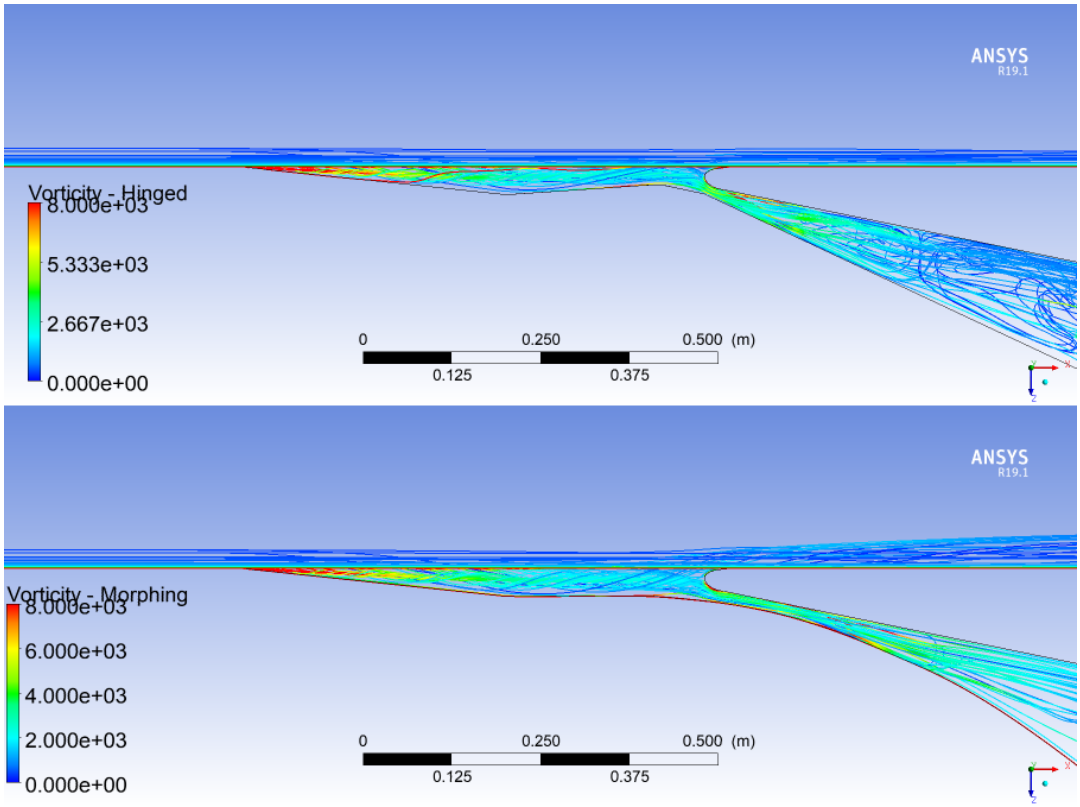

Figure 5.23: Side view of the NACA ram-air inlet. Configuration 1 with a mass flow rate of 0.300 $[kg/s]$. The vorticity strength $[1/s]$ is plotted with the streamlines of the airflow. Top shows the hinged case, bottom shows the morphing case.

5.5. DISTORTION

While the pressure recovery and drag are the most important indications of the performance of the NACA ram-air inlet, the distortion of the flow is an important parameter for the performance of the heat exchanger. The NACA ram-air inlet ingests ambient air that is used by the air-to-air heat exchangers as the coolant [12]. For optimal operation, a uniform flow field is desired at the face of the heat exchangers [55]. A non-uniform flow field can cause a large level of distortion to the flow which decreases the efficiency of the heat exchanger [56]. In this section, the effect on the magnitude and the distribution of the incoming flow at the face of the heat exchangers will be discussed. The distortion was analysed at the entrance face of the heat exchangers.

It was assumed that the heat exchangers are located downstream at the end of the closure flap mechanism. The location, at which the distortion is analysed, is shown in Figure 5.24.

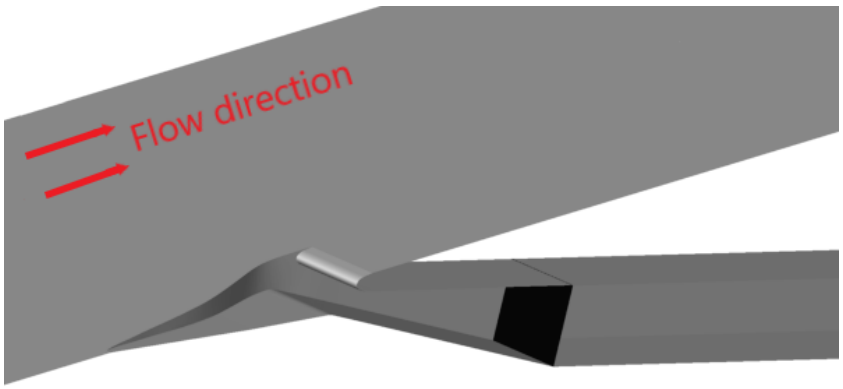

Figure 5.24: Half of the geometry of the NACA ram-air inlet is illustrated. The distortion plane is indicated in black.

Forced convection occurs in the heat exchanger since ambient air is sucked into the NACA ram-air inlet. The formula for the rate of heat transfer $\dot{Q}$ $[W]$ is shown in Equation 5.1 [57].

$$\dot{Q} = hA\Delta T \tag{5.1}$$

Where h is the heat transfer coefficient $[W/(m^2 \cdot K]$, A is the area of the heat transfer $[m^2]$ and ΔT is the temperature difference between the surface of the heat exchanger and the coolant $[K]$.

The heat transfer coefficient for forced convection is a function of the Nusselt number, shown in Equation 5.2 [58].

$$Nu = \frac{hL}{k} \tag{5.2}$$

Where h is the heat transfer coefficient $[W/(m^2 \cdot K)]$, k is the thermal conductivity of the fluid $[W/(m \cdot K)]$, and L is the characteristic length $[m]$. The Nusselt number is related to the heat transfer rate in a boundary layer. It was expected that the Nusselt number is a function of the Reynolds number and the Prandtl number, which is the relative thickness of the momentum diffusivity and the heat diffusivity [58]. The general relation of Nusselt number is given by Equation 5.3 [58].

$$Nu \propto Re^a \, Pr^b \tag{5.3}$$

Where Re is the Reynolds number, Pr is the Prandtl number, a and b are constants.

The Prandtl number of air is constant up to a temperature of 1000 $[K]$ [28]. This means that the amount of heat transfer in a heat exchanger of the aircraft is proportional to the velocity. Since the heat exchangers are located downstream of the distortion plane, it is assumed that the x-component of the velocity is the most prominent component of the velocity. The velocity-plots of Configurations 1,2, and 3 were analysed. Not all test cases showed large differences in the velocity plots. For this reason, a selection of the test cases with large differences in velocity-plots of each configuration was made.

Figures 5.25a and 5.25b show the velocity-plots of Configuration 1 at a mass flow rate of 0.100 $[kg/s]$ between the hinged and morphing flap.

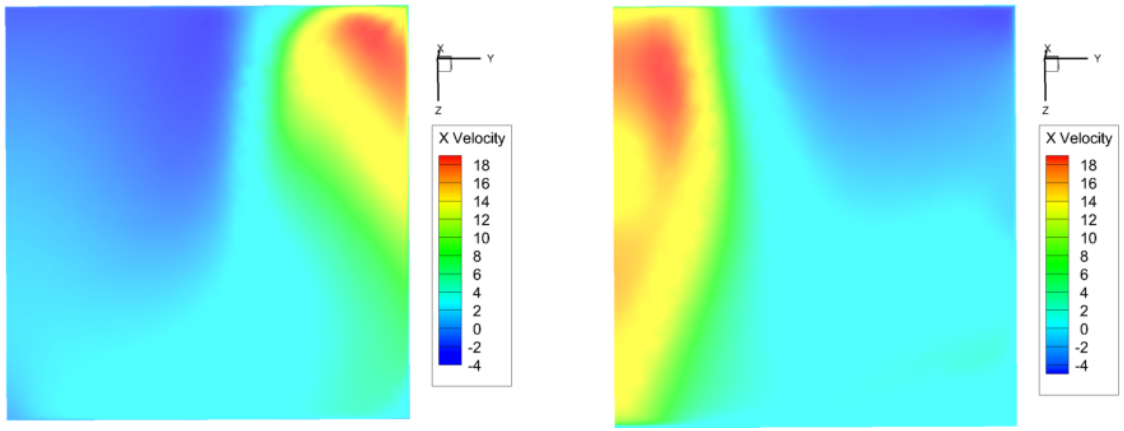

(a) Configuration 1 with a hinged flap - mass flow rate of 0.100 $[kg/s]$

(b) Configuration 1 with a morphing flap - mass flow rate of 0.100 $[kg/s]$

Figure 5.25: The velocity-plots at the distortion plane for Configuration 1 with a hinged flap and a morphing flap at a mass flow rate of 0.100 $[kg/s]$

From Figures 5.25a and 5.25b, it can be seen the velocity-plots of the hinged flap and the morphing flap cases of Configuration 1 are very different. The locations of the regions of high- and low-velocity occurs are mirrored along the z-axis. The region with the high velocity-component occurs in the top right corner in the case of a hinged flap, whereas the region of the high velocity-component is located in the top left corner in the case of a morphing flap. This region of high velocity in Figure 5.25b covers the entire left side of the duct. By replacing the conventional hinged flap with a new morphing flap will influence the distortion experienced at the distortion plane.

Figures 5.26a and 5.26b (shown on the next page) show the velocity-plots of Configuration 2 at a mass flow rate of 1.500 $[kg/s]$ between the hinged flap and morphing flap.

For Configuration 2 at a mass flow rate of 1.500 $[kg/s]$, large differences were found between the hinged flap and the morphing flap. It can be seen that the velocity-plots at the distortion plane have different patterns. Figure 5.26b, shows a large region of high velocity at the bottom and the right side. A small region of low velocity is present at the bottom of the velocity plot. In Figure 5.26b, there is a larger region of low velocity at the right bottom corner. The flow is separated at the wall. With a conservative approach, it is assumed that the magnitude of the x-component of the velocity is related to the efficiency of the heat transfer. The large differences in the velocity plots between the hinged flap in Figure 5.26b and morphing flap case in 5.26b will influence the heat transfer efficiency of the heat exchanger of the ECS, but this is beyond the scope of this thesis.

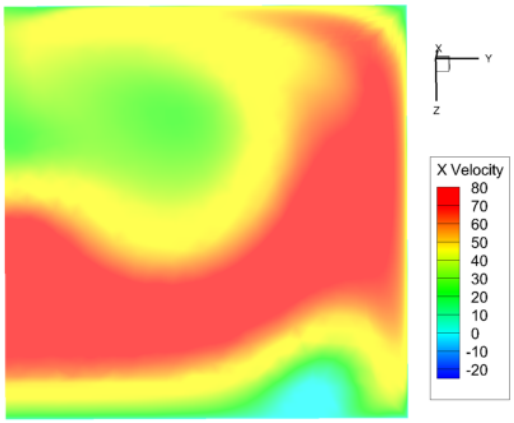

(a) Configuration 2 with a hinged flap - mass flow rate of 1.500 $[kg/s]$

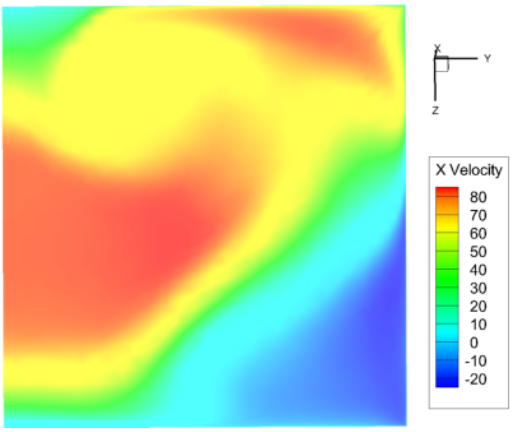

(b) Configuration 2 with a morphing flap - mass flow rate of 1.500 $[kg/s]$

Figure 5.26: The velocity-plots at the distortion plane for Configuration 2 with a hinged flap and a morphing flap at a mass flow rate of 1.500 $[kg/s]$

Figures 5.27a and 5.27b show the velocity-plots of Configuration 3 at a mass flow rate of 2.500 $[kg/s]$ between the hinged and morphing flap.

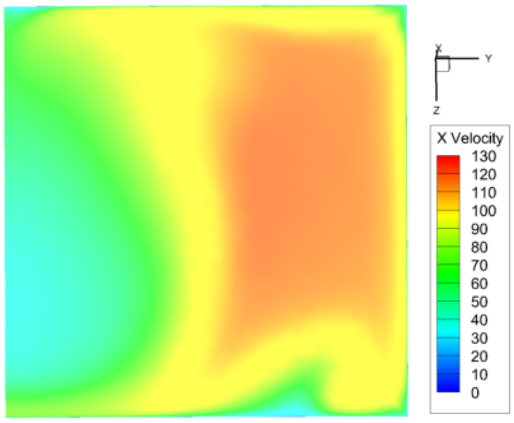

(a) Configuration 3 with a hinged flap - mass flow rate of 2.500 $[kg/s]$

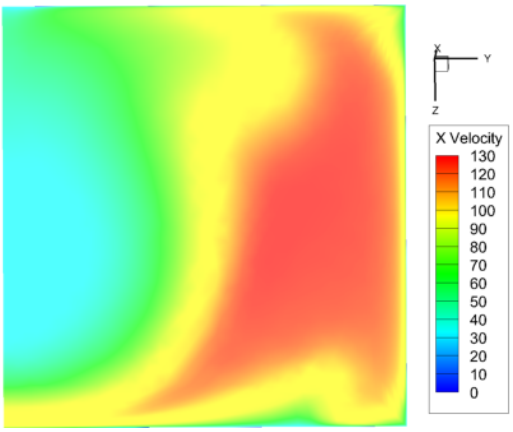

(b) Configuration 3 with a morphing flap - mass flow rate of 2.500 $[kg/s]$

Figure 5.27: The velocity-plots at the distortion plane for Configuration 3 with a hinged flap and a morphing flap at a mass flow rate of 2.500 $[kg/s]$

Figures 5.27a and 5.27b show large similarities. It can be seen that there is a region of high velocity on the right side of the distortion plane for both cases. The magnitude of the x-component is higher in the morphing case. Furthermore, a region of low velocity around 30-40 [m/s] can be seen in both hinged flap and morphing flap cases. Although this region of low velocity is larger in the case of the morphing flap. A low velocity decreases the heat transfer efficiency of the heat exchanger. There are differences in the velocity distribution in the distortion plane, which will affect the efficiency of the heat exchanger.

6

CONCLUSIONS AND RECOMMENDATIONS

The chapter consists of the conclusions of this thesis on the aerodynamic analysis on the performance of the NACA ram-air inlet by using CFD simulations. The conclusions of this study will be presented in Section 6.1. Based on the findings of this thesis, recommendations for future research on NACA ram-air inlets are discussed in Section 6.2.

6.1. CONCLUSIONS

The research objective of this thesis is to analyse the aerodynamic effects of the closure flap mechanism inside the NACA ram-air inlet. It was known that the presence of a pronounced kink between the conventional hinged flap caused undesirable aerodynamic effects, such as pressure losses and vibrations. The novel morphing flap as the new closure flap design was expected to improve the inlet performance of the NACA ram-air inlet. A CFD study on the NACA ram-air inlet was carried out to analyse the aerodynamic performance on the NACA ram-air inlet by using two different closure flap designs. Each flap design was analysed for three different configurations in which the throat area is varied. The mass flow rate was varied in the CFD simulations.

The analysis has demonstrated that the configuration with the smallest throat, Configuration 1 with an opening of 15 $[mm]$ inside the NACA ram-air inlet showed a significant improvement in pressure recovery. The largest improvement in terms of pressure recovery was found for Configuration 1, which was found to be 13.5% at a low mass flow rate of 0.100 $[kg/s]$. The relative difference between the maximum pressure recovery between the morphing flap and the hinged flap for Configuration 1 was found to be slightly more than 10%. After the maximum pressure recovery for Configuration 1 with the morphing flap has been reached, the pressure recovery decreases significantly with increasing mass flow rates.

The deterioration of the performance of the morphing flap was explained as follows. The throat of Configuration 1 with morphing flap lies more downstream than in Configuration 1 with hinged flap. Due to the difference in geometry, the pressure recovery was also measured further downstream for the morphing flap. This causes more pressure loss due to skin friction, reducing the measured pressure recovery.

By assessing the Cp-plots of the ramp and the closure flap between Configuration 1 with a hinged flap and a morphing flap, it was shown that a strong suction peak was present at the location of the sharp kink, Kink no.1 in the hinged flap. This kink has been eliminated by the smooth characteristics of the morphing flap, minimising the local supervelocity. This means that the strong

adverse gradient is reduced, such that the onset of flow separation is delayed, minimising pressure losses. For Configuration 1, the maximum drag improvement by replacing the hinged flap with the morphing flap was 33.1%.

The pressure recovery of Configuration 2 with a morphing flap, compared to Configuration 2 with a hinged flap, is higher for most mass flow rates. Although the Cp-plot between Configuration 2 with a hinged flap and a morphing flap showed that there was a suction peak located at the 'axis of the rotation of the flap', this suction peak was not strong due to the smooth geometry of the hinged flap.

The pressure recovery of Configuration 3 with a morphing flap was lower for most mass flow rates compared the Configuration 3 with a hinged flap. This was caused by the larger ramp angle in the morphing flap that causes high obliquity and high spillage of the flow, resulting in large pressure losses.

The maximum pressure recovery is the point at which the pressure losses due to vortex cores and boundary layer are minimal. For low mass flow rates, a larger portion of the airflow is not being ingested into the NACA ram-air inlet but spilt over the NACA ram-air lip. The effect of the vortices on the thinning out the boundary layer is weaker. Beyond the maximum pressure recovery, the effect of thinning out the boundary layer is outweighed by the detrimental effect of vortex ingestion. This was shown in the vorticity plots. Vortex ingestion is high, which results in higher pressure losses due to vortex cores.

By calculating the relative difference of the pressure recovery of the configuration with the morphing flap with respect to the configuration with the hinged flap, it can be found that the largest improvement was found at low mass flow rates. The largest improvement in pressure recovery was found on Configuration 1 with an opening of 15 $[mm]$ to be 13.5% at a low mass flow rate of 0.100 $[kg/s]$. The relative difference of the drag counts of the configuration with morphing flap with respect to the configuration with the hinged flap was calculated. It was observed that the configuration with morphing has an improvement in its drag performance for a broad range of low mass flow rates. The largest improvement in drag can be found for low mass flow rates, especially for configuration with the smallest throat: Configuration 1 with an opening of 15 $[mm]$. From the drag envelope, it was found that the maximum drag improvement of the morphing flap with respect to the hinged flap is 33.8% at a mass flow rate of 0.100 $[kg/s]$.

6.2. RECOMMENDATIONS FOR FUTURE WORK

This section presents the recommendations for future research on NACA ram-air inlets with the closure flap design.

In this thesis, the main goal was to compare the differences in the inlet performance by replacing the conventional hinged flap design with a morphing plate. The results were obtained by using CFD simulations. Since no comparable research on NACA ram-air inlets with closure flap deflections has been conducted yet, the results of the CFD simulations have not been validated. It is recommended to validate the accuracy of the CFD results with data obtained from wind tunnel experiments or test flights.

In this thesis project, the aerodynamic analysis on the performance of the NACA ram-air inlet for two different closure flap designs was conducted at a low-speed Mach of 0.2 at sea-level conditions. It is expected that the kinks in the hinged flap cause stronger undesirable effects at high-speed. Fur-

thermore, since low-speed CFD analyses were done in this thesis the drag reduction of the NACA ram-air inlet is not a good representation for an Airbus A320 in cruise flight. By conducting a high-speed analysis with the corresponding cruise conditions on the similar NACA ram-air inlet with hinged flap and morphing flap, a good calculation on the fuel savings in cruise can be made.

The NACA ram-air inlet was modelled on a flat plate, which is different from the real ram-air inlet component on an aircraft. It is recommended to model a full aircraft in order to gain more insights about the influence of the boundary layer of the fuselage on the inlet performance.

The curves of the morphing flap were obtained from experimental bending tests. The morphing flap was installed on a full-scale test demonstrator based on the dimensions of the real NACA ram-air inlet. Due to the geometrical differences between the design of the hinged and morphing flap, the location of the throat area was varied for different flap deflection. Especially, the throat area of the closed Configuration 1 with the morphing flap was located more downstream in the duct, while the same Configuration 1 with the hinged flap had the throat area located in the vicinity of the NACA ram-air lip. It is expected that the location has influenced the calculation of the pressure recovery at the throat. It is recommended to investigate the pressure recovery for Configuration 1 with the morphing flap at the same location of the throat area in Configuration 1 with the hinged flap.

The vortices that are created by the NACA ram-air inlet thins out the boundary layer. Since the CFD simulations were conducted in RANS, the turbulence scale structures in the flow may not be fully captured. The complex interaction of the boundary layer and the vortices that are generated around the edges of the NACA ram-air inlet may not be fully understood using RANS. Unsteady-RANS (URANS), LES or DNS simulations can be conducted to gain more insights in the boundary layer and vortex interaction in the NACA ram-air inlet [59].

A combination of structured and unstructured meshes, a hybrid mesh, was used for the CFD simulations. The generation of a structured mesh around the intersection of the NACA ram-air lip and the edges is very difficult due to the complexity of the NACA ram-air inlet. Since the NACA ram-air inlet is a complex geometry, a well-defined structured mesh can be a very challenging and time-consuming task. The structured mesh has advantages too. The connectivity of a structured mesh is more efficient than an unstructured mesh. This leads to lower memory requirement. A structured mesh allows the user to have more control over the refinement of the mesh. This can lead to a lower cell count, which reduces the run time of the CFD simulations. The cells of the structured grids are also better aligned with the flow, leading to better convergence.

Essentially, the performance of the NACA ram-air inlet for different sets of flap designs and configurations was studied. The NACA ram-air inlets are not the only type of submerged inlets used on aircraft, parallel-walled inlets are also used (on the Airbus A380). A similar study can be done on the effect by replacing the conventional closure flap on the parallel-walled inlet with a morphing flap.

BIBLIOGRAPHY

[1] European Commission, *Flightpath 2050: Europe's vision for aviation,* (2011).

[2] *Horizon 2020,* https://ec.europa.eu/programmes/horizon2020/en, accessed: 21-03-2018.

[3] T. Hartuç, *MANTA - Synthesis on Feasibility and Impact of Adaptable Air Inlet Concepts*, Tech. Rep. (Clean Sky II Airframe ITD Consortium, 2019).

[4] L. Eça and M. Hoekstra, *Discretization uncertainty estimation based on a least squares version of the grid convergence index,* 2nd Workshop on CFD Uncertainty Analysis (2006).

[5] E. A. Mossman and L. M. Randall, *An experimental investigation of the design variables for NACA submerged duct entrances*, Tech. Rep. No. A7I30 (NACA, 1948).

[6] *Manta and novair: two successful clean sky 2 proposals,* https://www.tudelft.nl/en/2016/lr/manta-and-novair-two-successful-clean-sky-2-proposals, accessed: 22-03-2018.

[7] B. Silveira, P. R. Souza, and O. Almeida, *Numerical investigation of a naca air intake for a canard type aircraft,* International Journal of Advanced Engineering Research and Science **4**, 32 (2017).

[8] E. Taskinoglu and D. Knight, *Numerical analysis of submerged inlets,* in *20th AIAA Applied Aerodynamics Conference* (2002) p. 3147.

[9] F. M. Rogallo, *Internal-flow systems for aircraft*, Tech. Rep. No. 713 (NACA, 1941).

[10] C. W. Frick, W. F. Davis, L. M. Randall, and E. A. Mossman, *An experimental investigation of NACA submerged-duct entrances*, Tech. Rep. No, 85g23 (NACA, 1945).

[11] P. Garrison, *The scoop on the naca scoop,* https://www.flyingmag.com/scoop-naca-scoop (2004), accessed: 13-08-2018.

[12] I. Martinez, *Aircraft environmental control,* Academic Website Universidad Politécnica de Madrid (2014).

[13] Airbus, *Airbus A320 Airplane Flight Manual - Master Configuration Deviation List*, Airbus (2011).

[14] Liebherr-Aerospace Lindenberg, *A319/A320/A321 Environmental Control System* (2004).

[15] L. Hime, C. C. Pérez, L. F. F. da Silva, S. B. Ferreira, A. B. de Jesus, V. L. Takase, and H. T. M. Vinagre, *A Review of the Characteristics of Submerged Air Intakes,* 18th International Congress of Mechanical Engineering, COBEM2005-1016, Ouro Preto-MG-Brazil (2005).

[16] A. H. Sacks and J. R. Spreiter, *Theoretical investigation of submerged inlets at low speeds*, Tech. Rep. NACA-TN-2323 (NACA, 1951).

[17] N. K. Delany, *An Investigation of Submerged Air Inlets on a 1/4-Scale Model of a Typical Fighter-Type Airplane*, Tech. Rep. (NACA, 1948).

[18] D. E. Gault, *An Experimental Investigation of NACA Submerged Air Inlets on a 1/5-Scale Model of a Fighter Airplane*, Tech. Rep. (NACA, 1947).

[19] J. L. Frank and R. A. Taylor, *Comparison of Drag, Pressure Recovery, and Surface Pressure of a Scoop-type Inlet and an NACA Submerged Inlet at Transonic Speeds*, Tech. Rep. (NACA, 1951).

[20] E. A. Mossman, *A comparison of two submerged inlets at subsonic and transonic speeds*, Tech. Rep. (NACA, 1949).

[21] N. J. Martin and A. H. Curt, *An experimental investigation at large scale of several configurations of a naca submerged air intake*, Tech. Rep. (NACA, 1948).

[22] J. S. Dennard, *The Total-Pressure Recovery and Drag Characteristics of Several Auxiliary Inlets at Transonic Speeds*, Tech. Rep. (NASA, 1959).

[23] R. Devine, J. Watterson, and R. Cooper, *Performance improvement of flush, parallel walled auxiliary intakes by means of vortex generators,* in *Proceedings of the 24th International Congress for Aeronautical Sciences* (2004).

[24] C. C. Pérez, L. F. da Silva, A. B. Jesus, S. B. Ferreira, and G. L. Oliveira, *Effective Use of Vortex Generators to Improve the Performance of Submerged Air Inlets for Aircrafts,* 11th Brazilian Congress of Thermal Engineering and Sciences (2006).

[25] N. J. Pignier, C. J. O. Reilly, S. Boij, and J. A. Dahan, *Aeroacoustic analysis of a naca duct,* Euronoise (1997).

[26] ESDU, *Pressure recovery of axisymmetric intakes at subsonic speeds,* Engineering Sciences Data Unit (1980).

[27] C. a. Batt, *Subsonic drag and pressure recovery of rectangular planform flush auxiliary inlets with ducts at angles up to 90 degrees*, Tech. Rep. August (ESDU 03006, 2003).

[28] J. Anderson, *Fundamentals of Aerodynamics*, McGraw-Hill series in aeronautical and aerospace engineering (McGraw-Hill Education, 2011).

[29] W. Sutherland, *Lii. the viscosity of gases and molecular force,* The London, Edinburgh, and Dublin Philosophical Magazine and Journal of Science **36**, 507 (1893).

[30] *Ansys fluids computational fluid dynamics,* https://www.ansys.com/products/fluids (2019), accessed: 14-03-2018.

[31] *ANSYS Fluent Users Guide*, ANSYS Inc. (2013).

[32] J. Tu, G. H. Yeoh, and C. Liu, *Computational fluid dynamics: a practical approach* (Butterworth-Heinemann, 2008).

[33] *Cfd online,* http://www.cfd-online.com, accessed: 14-03-2018.

[34] H. Versteeg and W. Malalasekera, *An Introduction to Computational Fluid Dynamics* (New York, 1995).

[35] J. Ferziger and M. Peric, *Computational Methods for Fluid Dynamics* (Springer Berlin Heidelberg, 2002).

[36] J. D. Anderson and J. Wendt, *Computational fluid dynamics*, Vol. 206 (Springer, 1995).

[37] D. Wilcox, *Turbulence Modelling CFD* (DCW Industries. Inc., 1993).

[38] S. Hickel, *CFD for Aerospace Engineers Lecture Notes* (Delft University of Technology, 2017).

[39] W. Jones and B. E. Launder, *The prediction of laminarization with a two-equation model of turbulence,* International journal of heat and mass transfer **15**, 301 (1972).

[40] F. R. Menter, *Two-equation eddy-viscosity turbulence models for engineering applications,* AIAA journal **32**, 1598 (1994).

[41] A. Menon, *NACA Ducts in vehicle thermal simulations*, Master's thesis, Chalmers University of Technology (2017).

[42] P. D. Bates, S. N. Lane, and R. I. Ferguson, *Computational fluid dynamics: applications in environmental hydraulics* (John Wiley & Sons, 2005).

[43] *Users manual tecplot 360 ex 2019 release 1,* http://download.tecplot.com/360/current/360_users_manual.pdf (2020), accessed: 14-03-2020.

[44] J. Cremers, H. Derlien, K.-D. Kricke, and K. Wilke, *Air conditioning system for aircraft cabins,* (2010), uS Patent App. 12/667,737.

[45] *Simscale cae forum,* https://www.simscale.com/forum/t/what-is-y-yplus/82394, accessed: 22-03-2019.

[46] S. M. Salim and S. Cheah, *Wall y strategy for dealing with wall-bounded turbulent flows,* in *Proceedings of the international multiconference of engineers and computer scientists*, Vol. 2 (2009) pp. 2165–2170.

[47] F. White and I. Corfield, *The stability of laminar flows,* Viscous fluid flow **2** (2006).

[48] M. Ruetten and H. Wendland, *Performance Enhancement of Auxiliary Air Intakes Using Vortex Generators,* 50th AIAA Aerospace Sciences Meeting including the New Horizons Forum and Aerospace Exposition (2012).

[49] L. Eça and M. Hoekstra, *On the influence of the iterative error in the numerical uncertainty of ship viscous flow calculations,* 26th ONR Symposium on Naval Hydrodynamics (2006).

[50] *MATLAB version 9.3.0.713579 (R2017b)*, The Mathworks, Inc., Natick, Massachusetts (2017).

[51] A. M. Jawarneh, P. Sakaris, and G. H. Vatistas, *Experimental and analytical study of the pressure drop across a double-outlet vortex chamber,* (2007).

[52] L. R. Jenkinson, P. Simpkin, D. Rhodes, L. R. Jenkison, and R. Royce, *Civil jet aircraft design*, Vol. 338 (Arnold London, 1999).

[53] J. Van Wensveen, F. Peter, T. Rau, and M. Hornung, *Assessment of a fuel cell powered full electric subsystem architecture for the avacon research baseline aircraft,* in *Proceedings of the German Aerospace Congress* (2019).

[54] E. Obert, *Aerodynamic design of transport aircraft* (IOS press, 2009).

[55] J. Kurzke and I. Halliwell, *Inlet flow distortion,* in *Propulsion and Power* (Springer, 2018) pp. 249–267.

[56] A. Zinkevich, V. Sharifullin, and A. Sharifullin, *Analyzing the effect on heat transfer due to nonuniform distribution of liquid flow among the tubes of a shell-and-tube heat exchanger,* Thermal engineering **57**, 807 (2010).

[57] P. Böckh and T. Wetzel, *Heat transfer: basics and practice* (Springer Science & Business Media, 2011).

[58] J. Monteith and M. Unsworth, *Principles of environmental physics: plants, animals, and the atmosphere* (Academic Press, 2013).

[59] N. J. Pignier, C. J. OReilly, and S. Boij, *Aerodynamic and aeroacoustic analyses of a submerged air inlet in a low-mach-number flow,* Computers & Fluids **133**, 15 (2016).

A

APPENDIX A: GEOMETRICAL SHAPE DATA OF THE NACA RAM-AIR INLET

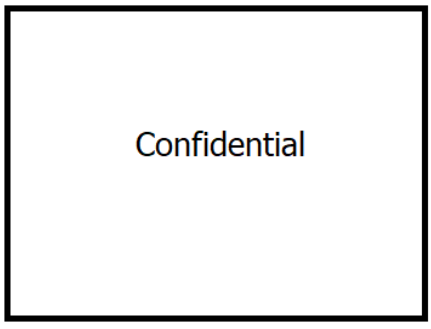

Figure A.1: Data points of the NACA ram-air inlet shown in CATIA

Table A.1: Coordinates of the NACA ram-air inlet

x in [mm]	y in [mm]	z in [mm]
confidential		

x in mm	x in mm	x in mm
confidential		